ornl

ORNL/TM-13735

OAK RIDGE NATIONAL LABORATORY

LOCKHEED MARTIN

Heavy Vehicle Propulsion System Materials Program Semiannual Progress Report for April 1998 Through September 1998

Prepared for
U.S. Department of Energy
Assistant Secretary for
Energy Efficiency and Renewable Energy
Office of Transportation Technologies

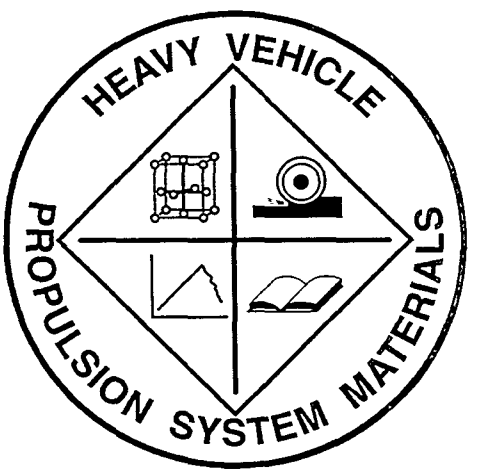

MANAGED AND OPERATED BY
LOCKHEED MARTIN ENERGY RESEARCH CORPORATION
FOR THE UNITED STATES
DEPARTMENT OF ENERGY

ORNL-27 (3-96)

ORNL/TM-13735

Metals and Ceramics Division

HEAVY VEHICLE PROPULSION SYSTEM MATERIALS PROGRAM SEMIANNUAL PROGRESS REPORT FOR APRIL 1998 THROUGH SEPTEMBER 1998

D. R. Johnson
Program Manager

Date Published: January 1999

Prepared for
U.S. Department of Energy
Assistant Secretary for Energy Efficiency and Renewable Energy
Office of Transportation Technologies
EE 04 02 000

Prepared by the
OAK RIDGE NATIONAL LABORATORY
Oak Ridge, Tennessee 37831-6285
managed by
LOCKHEED MARTIN ENERGY RESEARCH CORP.
for the
U.S. DEPARTMENT OF ENERGY
under Contract DE-AC05-96OR22464

REPORTS PREVIOUSLY ISSUED

ORNL/TM-9325	Period March 1983-September 1983
ORNL/TM-9466	Period October 1983-March 1984
ORNL/TM-9497	Period April 1984-September 1984
ORNL/TM-9673	Period October 1984-March 1985
ORNL/IM-9947	Period April 1985-September 1985
ORNL/TM-10079	Period October 1985-March 1986
ORNL/TM-10308	Period April 1986-September 1986
ORNL/TM-10469	Period October 1986-March 1987
ORNL/TM-10705	Period April 1987-September 1987
ORNL/TM-10838	Period October 1987-March 1988
ORNL/TM-11116	Period April 1988-September 1988
ORNL/TM-11239	Period October 1988-March 1989
ORNL/TM-11489	Period April 1989-September 1989
ORNL/TM-11586	Period October 1989-March 1990
ORNL/TM-11719	Period April 1990-September 1990
ORNL/TM-11859	Period October 1990-March 1991
ORNL/TM-11984	Period April 1991-September 1991
ORNL/TM-12133	Period October 1991-March 1992
ORNL/TM-12363	Period April 1992-September 1992
ORNL/TM-12428	Period October 1992-March 1993
ORNL/TM-12674	Period April 1993-September 1993
ORNL/TM-12778	Period October 1993-March 1994
ORNL/TM-12924	Period April 1994-September 1994
ORNL/TM-13046	Period October 1994-March 1995
ORNL/TM-13219	Period April 1995-September 1995
ORNL/TM-13262	Period October 1995-March 1996
ORNL/TM-13395	Period April 1996-September 1996
ORNL/TM-13467	Period October 1996-March 1997
ORNL/TM-13562	Period April 1997-September 1997
ORNL/TM-13648	Period October 1997-March 1998

Research sponsored by the U.S. Department of Energy, Assistant Secretary for Energy Efficiency and Renewable Energy, Office of Transportation Technologies, as part of the Heavy Vehicle Propulsion System Materials Program, under contract DE-AC05-96OR22464 with Lockheed Martin Energy Research Corporation.

CONTENTS

HEAVY VEHICLE PROPULSION SYSTEM MATERIALS PROGRAM
SEMIANNUAL PROGRESS REPORT
FOR APRIL 1998 THROUGH SEPTEMBER 1998

SUMMARY AND INTRODUCTION

The purpose of the Heavy Vehicle Propulsion System Materials Program is the development of materials: ceramics, intermetallics, metal alloys, and metal and ceramic coatings, to support the dieselization of class 1-3 trucks to realize a 35% fuel-economy improvement over current gasoline-fueled trucks and to support commercialization of fuel-flexible LE-55 low-emissions, high-efficiency diesel engines for class 7-8 trucks.

The Office of Transportation Technologies, Office of Heavy Vehicle Technologies (OTT OHVT) has an active program to develop the technology for advanced LE-55 diesel engines with 55% efficiency and low emissions levels of 2.0 g/bhp-h NOx and 0.05 g/bhp-h particulates. The goal is also for the LE-55 engine to run on natural gas with efficiency approaching that of diesel fuel. The LE-55 program is being completed in FY 1997 and, after approximately 10 years of effort, has largely met the program goals of 55% efficiency and low emissions. However, the commercialization of the LE-55 technology requires more durable materials than those that have been used to demonstrate the goals. Heavy Vehicle Propulsion System Materials will, in concert with the heavy duty diesel engine companies, develop the durable materials required to commercialize the LE-55 technologies.

OTT OHVT also recognizes a significant opportunity for reduction in petroleum consumption by dieselization of pickup trucks, vans, and sport utility vehicles. Application of the diesel engine to class 1, 2, and 3 trucks is expected to yield a 35% increase in fuel economy per vehicle. The foremost barrier to diesel use in this market is emission control. Once an engine is made certifiable, subsequent challenges will be in cost; noise, vibration, and harshness (NVH); and performance.

The design of advanced components for high-efficiency diesel engines has, in some cases, pushed the performance envelope for materials of construction past the point of reliable operation. Higher mechanical and tribological stresses and higher temperatures of advanced designs limit the engine designer; advanced materials allow the design of components that may operate reliably at higher stresses and temperatures, thus enabling more efficient engine designs. Advanced materials also offer the opportunity to improve the emissions, NVH, and performance of diesel engines for pickup trucks, vans, and sport utility vehicles.

The principal areas of research are:

Cost Effective High Performance Materials and Processing
Advanced Manufacturing Technology
Testing and Characterization
Materials and Testing Standards

COST EFFECTIVE HIGH PERFORMANCE MATERIALS AND PROCESSING

Cost-Effective Smart Materials for Diesel Engine Applications

J. O. Kiggans, Jr., T. N. Tiegs,
F. C. Montgomery, and L. C. Maxey
Oak Ridge National Laboratory
Oak Ridge, TN 37831

Objective / Scope

There are two objectives for this project. The first is to evaluate the cost-effectiveness and maturity of various "Smart Materials Technologies," which are under consideration for diesel engine applications, such as fuel injection systems. The second is to work on materials development in "Smart Materials" systems, to enable these materials to be incorporated into working actuators and sensors.

Materials Task Introduction - Reliability Issue

The present work involves the fabrication of sintered piezoelectric lead zirconate titanate (PZT) materials. These materials have been shown to have a very fast response to an electrical stimulation, can be made in compact shapes, and have a low power consumption. While PZT materials have many useful characteristics, they also exhibit problems such as ageing, sensitivity to temperature variations, and low strength. An important issue with PZT materials, especially for the automotive industry, is "reliability." A number of research groups in the U. S. and Japan have begun to study this issue.[1,2,3,4,5,6] One basic finding of these investigations is that the reliability of the PZT materials is strongly affected by the quality of the green PZT preforms. These green preforms are often made by die press forming and more often by tape casting. Die pressing is a simple process, but it is not as amenable to large scale production, as is tape casting. Also, die pressing involves the use of dried powders that can easily agglomerate, which results in inferior green preforms. Tape casting has been employed for many years as the primary mode for forming capacitor and PZT materials.[6,7,8] This method involves the use of liquid slurries for increased uniformity of ceramic components, and if performed carefully, can result in flexible tapes that can be electroded and laminated into multilayer structures. However, tape casting requires excessive additions of binders and lubricants, which can result in low density green tapes with resulting defects in the sintered parts.[7]

One approach for producing high reliability PZT materials is to develop improved forming methods. In recent years, a new process has been developed at Oak Ridge National Laboratory (ORNL) for forming high strength, high uniformity, ceramic preforms.[8] This method has been employed with many ceramic materials including alumina, silicon, silicon nitride, silicon carbide, boron carbide, just to name a few. Gelcasting may pose advantages for forming of PZT materials. It is the intent of the first phase of this project to do a comparative study of PZT materials made using die press, tape cast, and gelcast methods. Both quantitative and qualitative comparisons will be used to judge the performance of the products. Gelcast forming will employ water as the solvent. If water can be used in the fabrication process, this will reduce the hazardous nature and overall costs of the both forming processes. Even if the water-based gelcast process does not prove to be viable, due to water induced chemical changes in the powders, the gelcast process is also amenable to an organic solvent system.

Part I. PZT Sample Preparation

Two PZT powders have been selected for consideration as candidate materials for actuator applications, APC 840 and APC 850 powders (APC Ceramics Inc.) also designated by generic industrial designations as PZT-4 and PZT-5A, respectively. In a previous reports, studies were performed to determine the proper dispersants for these powders in water-based slurries. These studies identified Darvan 821A as an effective dispersant for both powders.

APC Ceramics routinely makes green PZT discs using die press techniques. This was the first method used to make PZT green preforms. The as-received, APC 840 powders, were loaded into a 1.27 cm diameter die and pressed at 2.5, 5, 10, and 15 ksi. Some of the die pressed samples were then isopressed to 30 or 50 ksi pressures.

A number of monomer systems have been developed over the last five years for gelcast forming of green ceramic preforms. For this study a premix water-based solution containing 24 wt.% solution consisting of 3 parts methacrylamide (MAM) and 1 part polyethylene glycol dimethyacrylate (PEGDMA) and 0.8 parts glycerol was used to suspend the PZT materials. 9.4 ml of the premix solution, 2.9 ml water, and 0.156 ml of Darvan 821A were mixed, followed by step by step additions of 97.5 g of APC 840 powder, with vortexing. The slurry was mixed on a oblique blender overnight. 80 g of the slurry was then transferred to a fresh centrifuge tube and degassed in a bell jar with vibration. 8 µl of tetramethylammonium hydroxide (TEMED) catalyst and 80 µl 10 wt % ammonium persulfate initiator solution (APS) were added to the slurry with mixing. The slurry was poured into the open end of a 7.6 X 7.6 X 0.16 cm glass mold, which was covered with parafilm, and incubated at 45 °C for 1 h. The mold was then cooled, disassembled, and the PZT part transferred to a metal tray. The PZT part was covered with polyethylene glycol 400 for 1 h to remove the water from the gel. The gel was briefly rinsed in distilled water and then dried in room air. After 24 h, the part was dried at 40 °C for 4 h to remove the remaining water. Several 1.27 cm diameter discs were cut from the rectangular gelcast PZT part. Some discs were then isopressed to 30 or 50 ksi to increase the green densities.

A Duromax binder system (recommended by Rohm and Haas) was employed as the base binder system for the APC 840 PZT tapes. 3.2 ml of deionized water ,75 µl of Darvan 821A, and 200 µl of Surfanol A surfactant were added to a 50 cc centrifuge tube. 45 g of APC 840 PZT powder was dispersed in the solution using a vortex mixer. 6.4 cc of a 1 to 1 mix of Duromax 1070 and 1080 binders were then added to the slurry. The binder content of the tape cast samples was 5.9 wt % based on total weight of the binders and the ceramics. The slurry was mixed on a oblique blender overnight. 40 g of the slurry was then transferred to a fresh centrifuge tube and degassed in a bell jar with vibration. A small amount of the slurry was poured into a 2.5 X 5 by 0.16 open plastic mold, which was coated with WD40 release agent. This procedure was not a purely conventional tape cast method, since the slurry was not spread with a doctor blade, but instead poured and to the height of the mold sides. The tape solution was dried in the mold for 30 m at 37 °C, dried overnight at room temperature, and then dried at 40 °C for 4 h to remove the final remaining water. Discs that were 1.27 cm diameter were cut from the gelcast PZT part using a hole punch. Some parts were then isopressed to 30 or 50 ksi to further increase the densities of the discs. Larger tapes, which required significantly higher binder additions to prevent cracking of the tapes, were also made, but not used for the present tests.

Data

The green densities of the die press, gelcast, and tape cast discs, and those discs which were isopressed at 30 and 50 ksi, were determined from weight and volume calculations after a binder burnout step to 600 °C. Figure 1 shows the green densities of APC 840, PZT materials made using the different forming techniques. The data show that the green density of the material die pressed to 2.5 ksi was 52.5 %, and the green densities increased for die presses at the 5, 10, and 15 ksi, with values of 56.9, 61.3, and 63.6 %, respectively. As expected, the 30 and 50 ksi isopress treatment (after the die press) increased the green densities of all pressed samples. The green density of the sample produced using the gelcast process was 57.6 % of theoretical density. This is very high and is equivalent to material die pressed at 5 ksi. The 30 and 50 ksi isopress step of the gelcast parts produced high densities of 67.3 and 69.3, respectively. The green density of the tape cast PZT was 51.2, with increases to 57.4 and 59.1 for the 30 and 50 ksi isopress treatments. Clearly, the tape cast process was inferior to both die press and gelcast forming, when judged by comparisons of the green densities.

DTA- TGA analyses were performed on as received APC 840 powders (same as die pressed samples), gelcast preforms, and tape cast samples. Figures 2 and 3 are DTA and TGA graphs of the data for the as-received powder, a gelcast sample, and a tape cast sample. The data for the "as received powders" show that there were multiple peaks in the DTA trace, with most of the binder removed by 400 °C. The TGA curve for this material showed a gradual weight loss to 200 °C followed by a more rapid weight loss to 400 °C. The DTA data for the gelcast materials also had multiple peaks. The gelcast material also showed a gradual weight loss to 200 °C followed by a very gradual weight loss to the 400 °C completion. The DTA trace for the tape cast material was very different, with two sharp peaks, and the TGA trace indicates that most of the tape cast binder volatilized over a more narrow range of 300 °C to 400 °C. Overall, the data indicated that the burn out, volatilization of the as-received powders and gelcast materials was much more gradual and than the tape cast materials. The release of binders in the tape cast materials over narrow temperature range could lead to porosity problems in sintered samples.

Part II. Sintering of Lead Zirconate - Lead Titanate (PZT) Ceramics

In previous reports, results were presented concerning initial work in forming green preforms from commercial PZT-4 (APC 840) powders using die press, tape cast, and gelcast forming methods. The following work presents the results on initial sintering studies for the PZT-4 gelcast preforms. The goal is to find a simple, cost-effective, robust sintering method for these and other PZT materials.

It is well known that one of the major problems in the reproducible production of high quality PZT ceramics is controlling the volatility of the PbO component of PZT materials during the sintering process. A loss or gain of PbO during sintering will affect both the densification and the dielectric properties of the sintered materials. Some investigators have concluded that a 1 to 2 mole deficiency of PbO in sintered parts is a desired result.[9] Since PbO can be volatilized and lost from green parts during sintering, it is a common practice to use packing powders which will establish a PbO equilibrium with the samples, and prevent severe PbO deficiencies. Researchers have used a variety of combinations of gaseous PbO generators, such as PbO powder combined with $PbZrO_3$ or ZrO_2 . These powder mixtures have been packed in numerous ways relative to the PZT samples as illustrated in Figure 4.[9,10,11,12,13,14,15] The most questionable arrangement in this group is packing the samples directly in the packing powder (Fig. 4 b), since investigators have shown that direct contact between samples and packing powder lacking titanium ions (Ti) can lead to solid state

diffusion of Ti ions from the samples[9]. In all sintering arrangements one must also assure that sufficient O_2 is present during sintering to assure good densification.[14]

Experimental Results

The methods for preparation of the 10 X 10 X 0.2 cm PZT gelcast stock sheets were discussed on previous reports. Test parts, 1.25 X 1.25 X 0.2 cm, were cut from the larger stock sheets for the sintering trials. Figure 4a is a schematic of the crucible set-up used for sintering trials, which is the sintering configuration utilized by some investigators at Penn. State University.[15] Figure 5 is a schematic of the furnace used for the study. The nominal sample temperature was measured using a Type "S" thermocouple placed beneath the sample crucible. The alumina furnace tube was purged with flowing air throughout sintering runs. In most cases, binder burnout was performed prior to the sintering run, and but in one case, the binder burnout step was incorporated into the sintering run. The binder burnout step consisted of heating samples at 1°C / min to 300°C with a 1 h dwell in air, and then heating at the same rate to 500°C with an additional 1 h dwell. Samples were then heated at 10°C / min to temperature for the sintering runs. Samples were weighed before and after binder burnout and sintering runs to measure weight losses during binder burnout, and changes in weight during sintering. Densities of sintered samples were determined by alcohol immersion using the Archimedes method.

Table 1 is a summary of all of the sintering runs completed at this time. In experiment 1, PZT-4 samples were sintered at nominally 1100°C for 2 h in proximity to either a PbO/ $PbZrO_3$ (4:1) powder mixture or a (2:1) mixture. Similar results were observed for both samples adjacent or "near" to the two different powders. These samples had 3 % weight gains and 93 % theoretical densities (T.D.). The "far" samples both had a 1 % weight gains and 88-89 % densities. These results indicated that the 1100°C temperature was too low for complete sintering, and that there appeared to be a localized, uneven PbO atmosphere in the crucible, adjacent to the powder bed, which caused higher weight gains and higher densities for the "near" samples. Sintering run 2 was to 1200°C for 2 h with no powder in the sintering crucible. Both samples in this experiment had weigh losses of between 2.7 and 4.1 % and both reached approximately 98 % T.D. Thus 1200°C increased the sintered densities, but the higher weight losses indicated the need for better atmosphere control. Sintering run 3 had two sets of crucibles with the same PbO / $PbZrO_3$ (4:1) powder mixture. Very good sintered densities, 99.8 - 100 %, were obtained for all samples in this run, with the samples nearest the powder bed having the highest densities. Once again, those samples near the powder bed also showed the highest weight gains. Since some samples had over 3 % weight gains, it was decided to use run a fourth experiment at 1200°C with a powder bed of PbO/ $PbZrO_3$ (2:1). In run 4, the "near" samples once again had very high weight gains, along with slightly higher densities. The next experiment was performed at 1200°C with PbO/ $PbZrO_3$ (1:2) and PbO/ $PbZrO_3$ (1:4) powders. Very similar results were obtained for this experiment, indicating that, although good densification occurred, this packaging arrangement also had very localized PbO atmospheres, leading to uneven weight gains by samples at different positions within the sintering crucible. This series of five experiments indicate the difficulty with controlling the PbO atmosphere by adjusting powder beds by altering PbO and $PbZrO_3$ powder mixtures, although experiment 2, in which the PZT 840 powder was used as the atmosphere powder, showed some promise with only 1% weight losses for both samples and densities at 98 % T.D.

A second set of sintering experiments were then conducted using the inverted cover crucible configurations shown in Figure 6. Other investigators have successfully used this arrangement along with a PbO generating powder mixture consisting of 10 wt % ZrO_2 - 90

wt % $PbZrO_3$.[8,16] Three types of green PZT-4 preforms were tested in this sintering arrangement: glecast, die pressed, and tape cast parts. The procedures for gelcasting PZT-4 were described in previous reports. Die press operations were performed with a 1.13 in. diameter die and a Carver press. Samples were pressed to ~5000 psi using Mold Wiz AZN spray release (AXEL Plastics Research Laboratories). Tape cast materials were made using a Mistler TTC-1000 machine according to methods provided by R. E. Mistler, personal communications and referenced to published descriptions.[17] Tape cast and die pressed samples were isopressed to increase the green densities, but equity in green densities was not achieved for all samples. Following forming steps, all samples were processed to remove the binder. This consisted of a heating samples in air at 1°C/min to 300°C with a 1 h hold, followed by a second ramp at 1°C/min to 500°C with a 1 h hold, followed by a static furnace cool. Green densities were calculated from the sample volume and weight measurements after binder burnout. Samples were kept in a desiccator until the sintering step. Sintering was performed in one of two similar crucibles in the previously described tube furnace. The sample configuration is shown in Figure 6. Samples were then heated in flowing air at 10°C/min to 1200°C+/-10°C with a 2 h dwell, followed by cooling to room temperature at 10°C/min. Densities of sintered samples were measured by the Archimedes immersion method in absolute ethanol.

Table 2 lists the results for the sintering runs comparing the PZT materials formed by the three forming methods. Densities of the three sets of samples varied from 97.0 to 99.3 % T.D. The two die press/isopress samples, which had the highest green densities, 69.6 and 69.8 g/cm^3, reached the highest sintered densities, both 99.3 % T.D. The gelcast parts had slightly better densities that the tape cast parts. The weight losses of the three groups of samples varied from 0.1 to 0.28 %. Slight weight losses, such as were observed here, are desirable to obtain good piezoelectric properties in these materials. The high densities and the small weight losses of all three sample types indicates that the sintering arrangement is robust and reproducible for materials formed by various methods.

In addition to the 1200°C sintering experiments, two groups of gelcast samples were sintered at 1140°C+/-10°C in flowing air or oxygen. This lower temperature was chosen, since reported literature has indicated that this is the maximum temperature that can be used for sintering multilayered PZT structures containing internal electrodes consisting of the commonly used silver palladium mixtures. Above 1140°C the electrode material will react with PZT materials, and diminish the electrical conductivity of the electrode interlayer.[13,18,19] Figure 2 shows the sintered density of the gelcast PZT-4 parts held for various times at temperature in each atmosphere. The data show that an approximately 24 h dwell time at 1140°C is required to reach near full densities, with the sample in air reaching 98.9 % T.D. and the sample heated in O_2 to 99.8 % T.D. Figure 7 also shows sample weight losses at the various sintering intervals. The weight losses reached a near steady state at about 12 h for samples sintered in both atmospheres. The final weight losses were 0.68 % for the sample processed in air and 0.61 % for the sample processed in O_2. The differences for densification and weight losses for materials processed in air and O_2 were expected and have been observed by other investigators.[14,19,20] The explanation for the density difference is that when sintering in air, nitrogen gas bubbles can get trapped as closed pores, which prevent total densification. With oxygen, the O_2 gas in the closed pores can diffuse into the oxygen-containing PZT materials, allowing complete densification.

Measurement Equipment and Reliability Test Center

Several pieces of diagnostic equipment are being purchased for the characterization of the dielectric and piezoelectric properties of the PZT materials being fabricated for this project. In addition, a custom poling device has been built for poling the sintered PZT materials.

Work also continues in the set-up of electrical drive devices and diagnostic equipment for future reliability tests on PZT actuator materials or assemblies.

Travel

Travel to the American Ceramic Society Annual Meeting, May 3-6, 1998 in Cincinnati, Ohio to present a talk, "Gelcasting Systems for Forming Reactive Silicon Compositions," by J. O. Kiggans, Jr., T. N. Tiegs, J. L. Schroeder, and F. C. Montgomery.

Visitors

None

Publications

None.

Problems Encountered

None

References

1. K. Uchino, Piezoelectric Actuators and Ultrasonci Motors, Kluwer Academic Publishers, London, 1997.
2. T. Sakai, M. Ishikiriyama, Y. Terai, and R. Shimazaki, "Durability of Piezoelectric Ceramic for an Actuator," Jpn. J. Appl. Phys. Vol. 31, Pt. 1, No. 9b, pp. 3051 - 3054, 1992.
3. T. Sakai, M. Ishikiriyama, Y. Terai, and R. Shimazaki, "Improvement in the Durability of PZT Ceramics for Actuator, Toyota Technical Review, 42 (2), 56-62, 1993.
4. C. T. Sun and J. Z. Jiang, "Fatigue Behavior of Piezoelectric Ceramics," Proc. of Int. Soc. Opt. Eng. (SPIE), 3040, 129-159, 1997.
5. T. Tanimoto and K. Okazaki, "Fatigue, Degradation, and Reliability of Piezoelectric Ceramics," Jpn. J. Appl. Phys. Vol. 30, No. 9B, pp. 2410-2412, 1991.
6. S. Winzer, N. Shankar, and A. Ritter, "Designing Cofired Multilayered Electrostrictive Actuators for Reliability," J. Am. Ceram. Soc., 72, (12) pp. 2246 - 2257, 1989.
7. O. O. Omatete, M. A. Janney, and R. A. Strehlow, " Gelcasting - A New Ceramic Forming Process," Am Ceram. Soc. Bull., Vol., 70, No. 10, pp. 1641-1649, 1991
8. R. E. Mistler, "Tape Casting," Engineered Materials Handbook, Vol. 4: Ceramics and Glasses, ASM International, pp. 161-165, 1991.
9. A. Kingon and J. Clark, Sintering of PZT Ceramics: I Atmosphere Control, J. Am. Cer. Soc., Vol. 66, N0 4, pp. 253-256, 1982.
10. G. Snow, "Fabrication of Transparent Electrooptic PLZT Ceramics by Atmosphere Sintering," J. Am. Cer. Soc., Vol. 56, No. 2, pp. 91-95, 1973.
11. A. Kingon, J. Terblanche, and J. Clark, "The Control of Composition, Microstructure, and Properties of $Pb(Zr,Ti)O_3$ Ceramics," Mat. Sci. and Eng., Vol. 71, pp. 391-397, 1985.
12. S. Takahashi, S. Miyao, S. Yoneda, and M. Kuwabara, " Preparation of Dense and pure Perovskite Ceramics in $Pb(Ni_1y_3Nb_{2/3})O_3$-$PbTiO_3$ Systems, Jpn. J. Appl. Phys., Vol. 32, pp. 4245-4248, 1993.
13. D. Hind and P. Knott, "Aqueous and Sol-Gel Synthesis of Submicron PZT Materials and the Development of Tape Casting Systems for Multilayer Actuator Fabrication," in Electroceramics - Production, Properties, and Microstructures, W. Lee and A. Bell, eds.; University Press, Cambridge, UK, pp. 107-119, 1994.

14. T. Murray and R. Dungan, "Oxygen Firing can Replace Hot Pressing for PZT," Cer. Ind., Vol. 82 No. 6, pp. 74-77, 1964.
15. Personal communication, Dr. J. P. Maria, Penn. State University
16. A. Kingon, J. Terblanche, and J. Clark, "The Control of Composition, Microstructure, and Properties of $Pb(Zr,Ti)O_3$ Ceramics," Mat. Sci. and Eng., Vol. 71, pp. 391-397, 1985.
17. E. M. Anderson, R. A. Marra, and R. E. Mistler, " Tape Casting of Reactive Aluminas," Amer. Soc. Bull., Vol. 76 (7), pp. 45-50, 1997.
18. S. F. Wang, J. P. Daughtery, W. Huebner, and J. G. Pepin, "Silver-Palladium Thick-Film Conductors," J. Am. Ceram. Soc., Vol. 77 (12), pp. 3051-3072, 1994.
19. W. Wersing, H. Wahl, and M. Schnoller, " PZT-Based Multilayer Piezoelectric Ceramics with AgPd-Internal Electrodes," in Ferroelectrics, Vol. 87, pp. 271-294, 1988.
20. Moon, J. H. and Jang, H. M., "Effects of Sintering Atmosphere on Densification Behavior and Piezoelectric Properties of $Pb(Ni_{1/3}Nb_{2/3})O_3$-$PbTiO_3$-$PbZrO_3$ Ceramics, J. Ceram. Soc., Vol. 76 (2), pp. 549-552, 1993.

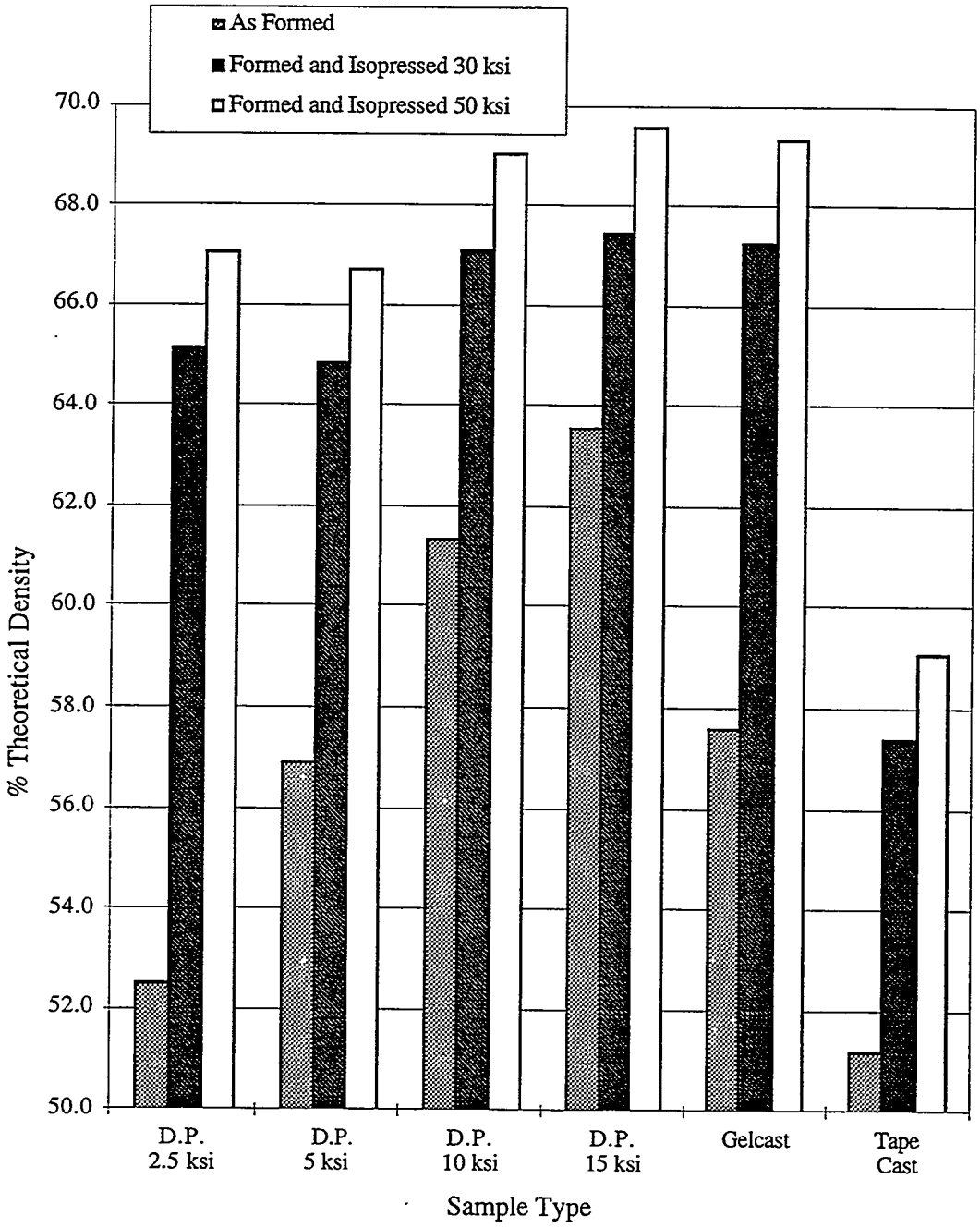

Figure 1. Green densities of APC 840 materials formed by die press (D. P.), tape cast, and gelcast methods, followed by an isostatic press treatment at 30 or 50 ksi.

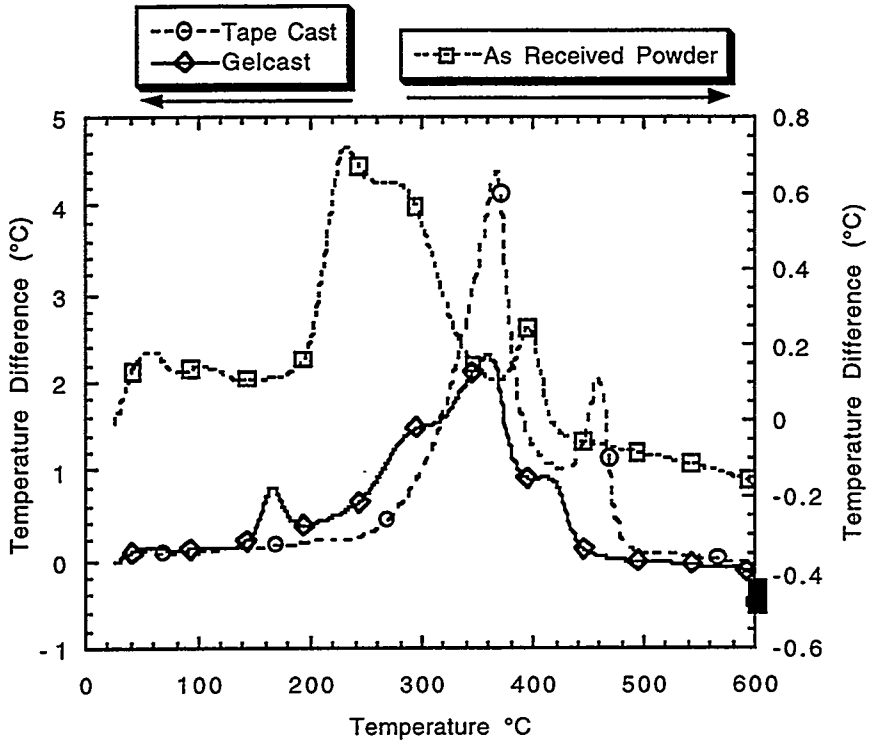

Figure 2. DTA of APC 840 materials as received, tape cast, and gelcast methods.

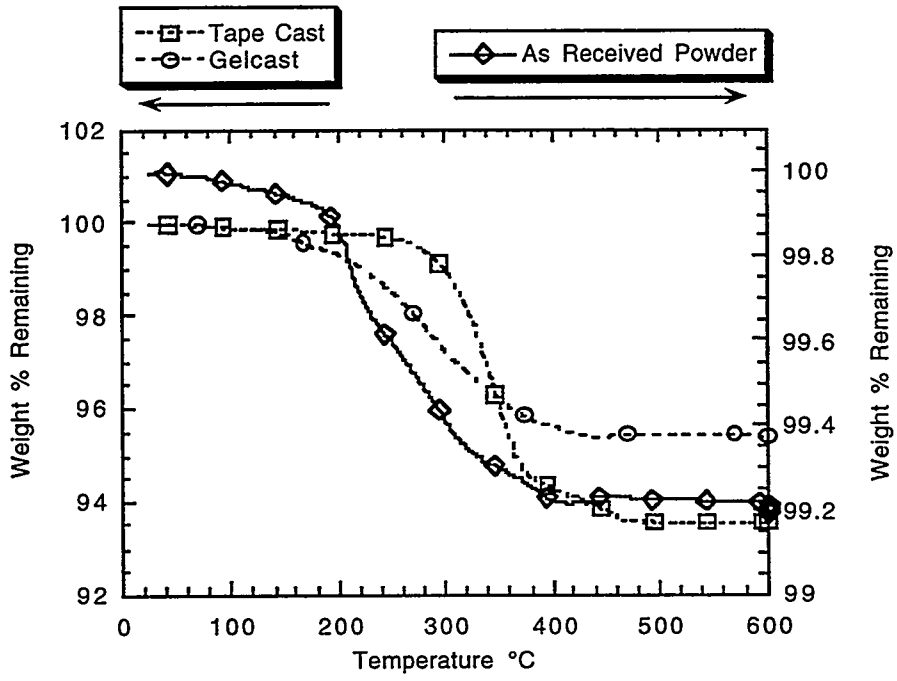

Figure 3. TGA of APC 840 materials as received, tape cast, and gelcast methods.

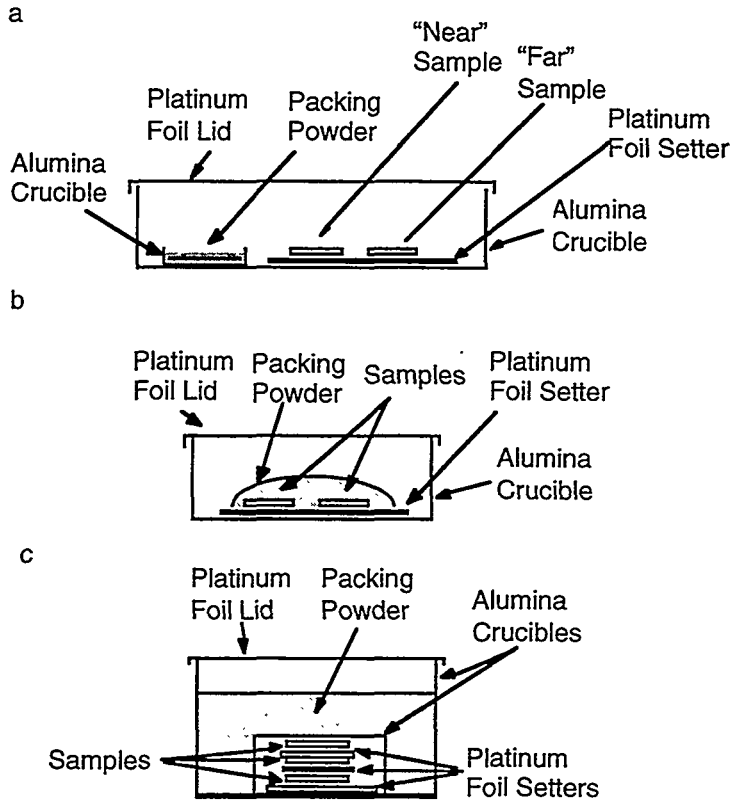

Figure 4. Three PZT configurations for sintering PZT materials with samples: a) placed adjacent to protective powders, b) buried in protective powders, or c) sealed under a protective crucible beneath protective powders.

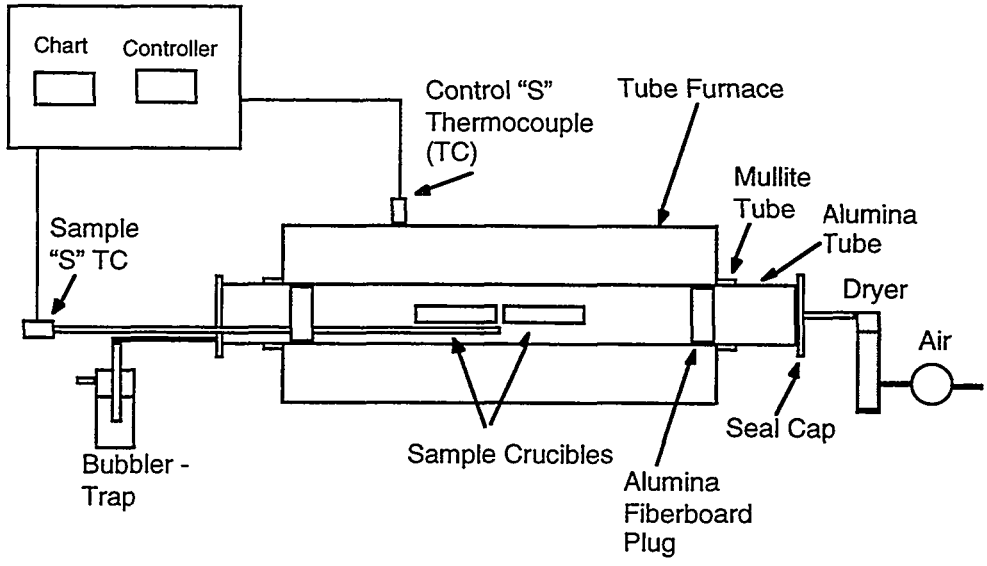

Figure 5. CM tube furnace with double tube arrangement for lead containment.

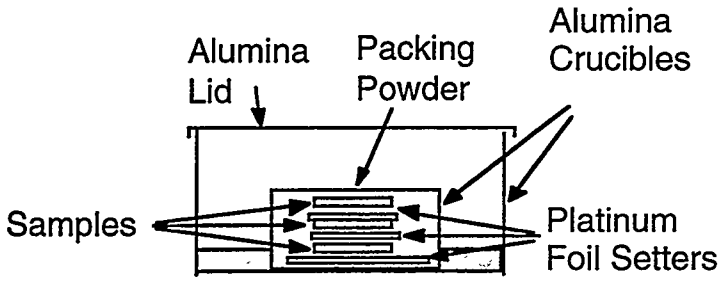

Figure 6. Crucible arrangement for PZT-4 sintering using inverted alumina cover and powder seal.

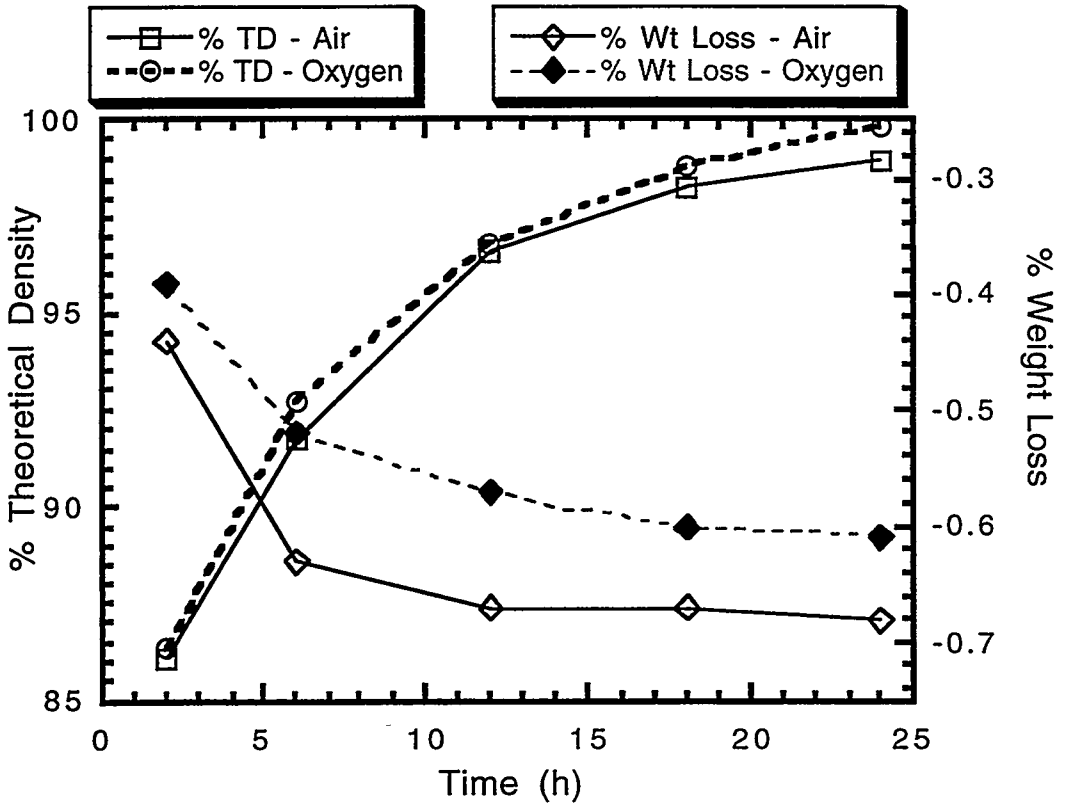

Figure 7. Sintered densities, expressed as % T.D., and weight losses for gelcast PZT-4 samples sintered
in air or oxygen.

Table 1. Data from PZT Sintering Trials

Run #	Sample #	Control Temp (°C)	Powder	Sample Position	(%) Wt Loss/Gain Sintering	Density (g/cm^3)	TD (%)
1	GC 2-92-3	1100	$PbO/PbZrO_3$ 4:1 ratio	near*	3.2	7.25	93.63
1	GC 1-92-6	1100	$PbO/PbZrO_3$ 4:1 ratio	far**	1.0	6.92	89.34
1	GC 1-92-3	1100	$PbO/PbZrO_3$ 2:1 ratio	near	2.8	7.26	93.84
1	GC 2-92-4	1100	$PbO/PbZrO_3$ 2:1 ratio	far	1.1	6.82	88.09
2	GC 1-1b	1200	none	near	-4.1	7.59	98.02
2	GC 2-3	1200	none	far	-2.7	7.64	98.70
2	GC 1-2	1200	PZT 840	near	-0.9	7.64	98.74
2	GC 2-4	1200	PZT 840	far	-1.0	7.66	98.97
3	GC 1-2a	1200	$PbO/PbZrO_3$ 4:1 ratio	near	NA***	7.76	100.19
3	GC 1-1a	1200	$PbO/PbZrO_3$ 4:1 ratio	far	2.8	7.73	99.88
3	GC 2-5	1200	$PbO/PbZrO_3$ 4:1 ratio	near	3.3	7.73	99.88
3	GC 1-2b	1200	$PbO/PbZrO_3$ 4:1 ratio	far	1.6	7.73	99.85
4	GC 2-6	1200	$PbO/PbZrO_3$ 2:1 ratio	near	4.4	7.75	100.07
4	GC 1-4	1200	$PbO/PbZrO_3$ 2:1 ratio	far	1.6	7.74	99.96
5	GC 2-92-6	1200	$PbO/PbZrO_3$ 1:2 ratio	near	5.7	7.72	99.78
5	GC 1-92-7	1200	$PbO/PbZrO_3$ 1:2 ratio	far	2.3	7.72	99.74
5	GC 1-92-5	1200	$PbO/PbZrO_3$ 1:4 ratio	near	3.5	7.70	99.52
5	GC 2-92-7	1200	$PbO/PbZrO_3$ 1:4 ratio	far	1.7	7.72	99.77

* In Figure 4a, the sample closest to powder , if used.
** In Figure 4a, the sample in furthermost position relative to powder.
*** Measurement not made

Table 2. Data for PZT-4 materials formed by gelcast, tape cast, and die press methods followed by isopress pressing, binder burnout, and sintering at 1200°C in air.

Sample #	Forming Method	% T.D. of Green Parts	Sintered Density (g/cm^3)	T.D. (%)	Weight Loss (%)
GC-#3-141-CA	Gelcast	57.0	7.64	98.5	-0.28
GC-#3-141-CB	Gelcast	56.6	7.66	98.9	-0.10
Mistler#2-231-F	Tape Cast/Isopress	56.3	7.52	97.0	-0.20
Mistler#2-231-F	Tape Cast/Isopress	57.8	7.56	97.5	-0.20
DP-231-D	Die Press/Isopress	69.6	7.69	99.3	-0.25
DP-231-B	Die Press/Isopress	69.8	7.69	99.3	-0.22

W.B.S. ELEMENT 1.2.3.1
LOW COST-HIGH TOUGHNESS CERAMICS

T. N. Tiegs, F. C. Montgomery, M. R. Snyder, D. L. Barker, J. L. Schroeder, and D. W. Coffey
Oak Ridge National Laboratory
Oak Ridge, TN 37831

Objective/Scope

Significant improvement in the reliability of structural ceramics for advanced diesel engine applications could be attained if the critical fracture toughness (K_{Ic}) were increased without strength degradation. Early results from ORNL research showed that significant increases in fracture toughness could be achieved by manipulating the microstructure to promote toughening mechanisms such as crack bridging. Excellent properties were obtained in this manner for the alumina and mullite matrix systems reinforced with SiC whiskers. In silicon nitride, mechanical property improvements were achieved by promoting acicular or elongated grain growth and these provided significant toughening on the same order as the whisker reinforced materials. Currently, the project is initiating studies on toughening of ceramics by two methods: microstructure development in oxide-based ceramics, and incorporation of ductile intermetallic phases.

Technical Highlights

In-Situ Toughening of Oxide-Based Ceramics by Microstructure Development

Microstructure manipulation has been used to increase the fracture toughness of ceramics for many years. Mainly, this has been done in the silicon nitride-based systems where growth of acicular grains has been encouraged. Recently, oxide-based ceramics have been studied to achieve the same type of results observed with silicon nitride. Initially, Al_2O_3 was investigated, however, mullite has also been examined.[1,2] Thus, because of the large potential, a study was initiated to develop in-situ toughened oxide-based ceramics.

To begin, mullite will be examined as the matrix because of its low thermal conductivity and expansion characteristics. Seeding of mullite has been shown to produce microstructures with anisotropic grain growth similar to that observed with in-situ reinforced silicon nitride.[1,2] However, to date, the experiments have been exploratory in nature and no mechanical properties have been reported for these materials. Consequently, samples are being prepared to produce mullite with the desired microstructures for mechanical property testing to determine their suitability for diesel engine applications.

Previously, it was reported that mullite seeds were being produced to be added back to pure matrix raw materials as shown in Table 1.

Sintering results on seeded mullite-based compositions are summarized in Fig. 1. As indicated, the addition of SrO inhibited the densification of the gel-derived mullite. On the other hand, Y_2O_3 additions improved densification, especially at the lower temperatures of ~1450°C. A commercial mullite powder was also tested for comparison purposes which did not attain high densities until temperatures of 1700°C were reached.

Fracture surfaces of the SrO-doped mullites are shown if Figs. 2 and 3. The fracture surfaces show transgranular fracture occurs indicating strong bonding between the intergranular phase and the matrix. For high toughness materials, debonding along the matrix-intergranular phase interface is necessary. Anisotropic grain growth to form

platelets was observed predominantly in the pore areas. At the present time, it is uncertain if the growth behavior to form anisotropic grains requires gas-phase transport or if the grains can be developed in the bulk during liquid phase sintering. Metallographic specimens are being prepared to determine this.

Examination of the fracture surfaces of the mullite materials with Y_2O_3 additions revealed similar behavior to the SrO-containing samples (Figs. 4 and 5). Transgranular fracture accompanied by preferential anisotropic grain growth in the pore regions was observed.

Polished and etched specimens of Fe-doped mullite revealed the anisotropic nature of the grains (Figs. 6 and 7). However, crack growth from a Vickers indentation showed that the crack propagation was transgranular for the most part. Consequently, measured fracture toughness values were low, $\leq$ 3 MPa$\sqrt{m}$. Further work will investigate alternate grain boundary phases to promote debonding between the anisotropic grains and the intergranular phases.

Along with the investigation of the mullite system, an exploratory study of the effect of dopants on the anisotropic grain growth of alumina was initiated. In contrast to mullite, alumina is readily available in high quality powders that sinter well. Consequently, the dopants were added to a commercial powder and a sintering study performed. The initial results on the densification are shown in Figs. 8 and 9 for a variety of dopants. The dopant additions were made at 0.5 mole % with and without an additional 5 mole % SiO_2 addition. The SiO_2 was added to determine the effects of a liquid phase on the densification behavior and microstructure development.

The microstructures have been characterized for evidence of anisotropic grain growth. Of the 44 samples examined to date, anisotropic grain growth has been observed for the following dopants: $\geq$ 5% Na_2O; 5% Na_2O-5% SiO_2; 4.5% Na_2O-0.5% Na_2AlF_6; and 5% La_2O_3. The microstructures for various compositions are shown in Figs. 10 through 14.

Aluminide-Bonded Ceramics

Previous studies have shown that the properties of the aluminide-bonded ceramics (ABC) are attractive for diesel engine applications and consequently, development of these materials was started. Issues to be studied include the fabrication of parts using cost-effective processing, effect of alloying elements on the properties and fabrication of near-net-shape parts for testing. Initially, a study was done to examine the sintering behavior of the aluminide-bonded ceramics at high binder contents. Most of the previous work on ABC's was done at binder contents of 10-30 vol. %. However, higher binder contents on the order of 30-50 vol. % are necessary for these composites to match the thermal expansion of steel.

Samples were prepared by two different methods: (1) sintering with pre-alloyed gas-atomized Ni_3Al or FeAl powders, and (2) reaction sintering with fine elemental powders to form Ni_3Al in-situ. The experimental plan is shown in Table 2.

The results of the densification study are shown in Fig. 15. As indicated, high densities were obtained for most compositions at temperatures of $\geq$1450°C. As expected, lower densities were observed with the 30% content of the Ni_3Al liquid phase in comparison to the higher volume contents. In addition, the densification of the FeAl-based materials was lower than that achieved by the Ni_3Al. This is in contrast to earlier work which indicated just the opposite effect. Besides the densification behavior, the samples are being characterized for strength, fracture toughness, and thermal expansion.

The microstructure of the TiC-30 vol. % Ni_3Al fabricated by sintering with prealloyed Ni_3Al (DC-10) is shown in Fig. 16. The large pore is a remnant of the initial Ni_3Al powders used in the fabrication. Evidently, during the initial stage of alloy melting, the liquid is wicked into the surrounding TiC powders by capillary action. Because of the large size of the pore it is difficult to eliminate during sintering. At the higher volume contents of Ni_3Al, the occurrence of these pores was less. In any case, their appearance would probably would be eliminated by using a sinter-HIP cycle, such as those used for WC-Co hardmetals.

The microstructure of a TiC-40 vol. % Ni_3Al sample fabricated by sintering with prealloyed Ni_3Al (DC-11) is shown in Fig. 17. The TiC particles exhibit a 'core-and-rim' morphology caused by reaction of the liquid Ni_3Al with the TiC. X-ray diffraction identified as a titanium nickel carbide. Such 'core-and-rim' structures have observed previously in TiC-Ni cermets.

Previous work showed that the alloying additives affect the sintering behavior and properties of the aluminide bonded ceramics. Consequently, a series of samples are presently being fabricated to determine the effect of alloying additives on the sintering behavior and properties of the aluminide-bonded TiC. The experimental plan is given in Table 3.

As shown in Figs. 18 and 19, no significant change in the densification behavior was seen with the additions of Fe or Ti. Alloying additions of Mo, Co or Si may have had a beneficial effect on densification especially at the lower sintering temperature used in the study (1400°C). In contrast, the additions of Cr or Zr inhibited densification as shown in Fig. 20. The effects of different alloying additive contents are shown in Figs. 21 and 22 for Fe and Cr, respectively.

Status of Milestones

On schedule.

Communications/Visits/Travel

Travel by T. N. Tiegs to attend the American Ceramic Society Annual Meeting in Cincinnati, OH, May 3-6.

Travel by T. N. Tiegs to present a paper entitled, "Effect of Alloying Additives on Properties of Ni_3Al-Bonded Hardmetals," at the International Conference on Powder Metallurgy in Las Vegas, NV, May 31-June 7.

Problems Encountered

None.

Publications

T. N. Tiegs, P. A. Menchhofer, C. B. Thomas and P. K. Liaw, "Effect of Alloying Additives on Fabrication and Properties of Ni_3Al AND FeAl-Bonded Hardmetals," to be published in Proceedings of International Conference on Powder Metallurgy and Particulate Materials (1998).

References

1. S.-H. Hong, W. Cermignani and G. L. Messing, "Anisotropic Grain Growth in Seeded and B_2O_3-Doped Diphasic Mullite Gels," J. Europ. Ceram. Soc., 16, 133-141 (1996).

2. T. J. Mroz and J. W. Laughner, "Microstructures of Mullite Sintered From Seeded Sol-Gels," J. Am. Ceram. Soc., 72[3]508-509(1989).

Table 1. Summary of mullite seed compositions for anisotropic grain growth experiments.

Specimen No.	Dopant[a]	Dopant Level	Alumina Source	Silica Source
ITM-1	None	--	Versal 850	Ludox HS-40
ITM-2	None	--	Versal 850	Ludox AS-40
ITM-Cr-1	Cr	21.5	Versal 850	Ludox HS-40
ITM-Cr-2	Cr	0.7	Versal 850	Ludox HS-40
ITM-Cr-3	Cr	0.7	Versal 850	Ludox AS-40
ITM-Cr-4	Cr	7.2	Versal 850	Ludox AS-40
ITM-Fe-1	Fe	7.2	Versal 850	Ludox AS-40
ITM-Fe-2	Fe	0.7	Versal 850	Ludox AS-40
ITM-Sr-1	Sr	7.2	Versal 850	Ludox AS-40
ITM-Sr-2	Sr	5.2	Versal 850	Ludox AS-40
ITM-Y-1	Y	7.2	Versal 850	Ludox AS-40
ITM-Y-2	Y	5.8	Versal 850	Ludox AS-40

[a] Added as either chrome acetate, iron nitrate, strontium carbonate or yttrium nitrate.

Table 2. Samples of aluminide-bonded TiC ceramics fabricated by different processing methods to determine the sintering behavior and properties.

Specimen No.	Binder Type	Binder Content (vol. %)	Fabrication Method[a]
DC-10	Ni_3Al (IC-50)	30	S/PA
DC-11	Ni_3Al (IC-50)	40	S/PA
DC-12	Ni_3Al (IC-50)	50	S/PA
DC-13	Ni_3Al	30	RS/E
DC-14	Ni_3Al	40	RS/E
DC-15	Ni_3Al	50	RS/E
DC-19	Fe-40Al	30	S/PA
DC-20	Fe-40Al	30	RS/E

[a] S/PA - Sintering with pre-alloyed powders; RS/E - Reaction sintering with elemental powders.

Table 3. Samples of aluminide-bonded TiC ceramics fabricated to determine the effect of alloying additives on the sintering behavior and properties of the aluminide-bonded TiC. All samples fabricated with 30 vol. % of the Ni_3Al binder phase by reaction sintering of elemental powders.

Specimen No.	Binder Composition	Substitution Site of Alloying Element
DC-22	$Ni_{2.85}Fe_{0.15}Al_{1.00}$	Both Ni and Al
DC-23	$Ni_{2.85}Fe_{0.20}Al_{0.95}$	Both Ni and Al
DC-24	$Ni_{2.40}Fe_{0.80}Al_{0.80}$	Both Ni and Al
DC-25	$Ni_{1.50}Fe_{2.00}Al_{0.50}$	Both Ni and Al
DC-26	$Ni_{2.85}Cr_{0.20}Al_{0.95}$	Both Ni and Al
DC-27	$Ni_{2.40}Cr_{0.80}Al_{0.80}$	Both Ni and Al
DC-28	$Ni_{2.40}Si_{0.80}Al_{0.80}$	Al Sites
DC-29	$Ni_{2.40}Ti_{0.80}Al_{0.80}$	Al Sites
DC-30	$Ni_{2.40}Mo_{0.80}Al_{0.80}$	Al Sites
DC-31	$Ni_{2.40}W_{0.80}Al_{0.80}$	Al Sites
DC-32	$Ni_{2.40}Co_{0.80}Al_{0.80}$	Ni Sites
DC-33	$Ni_{2.40}Zr_{0.80}Al_{0.80}$	Al Sites

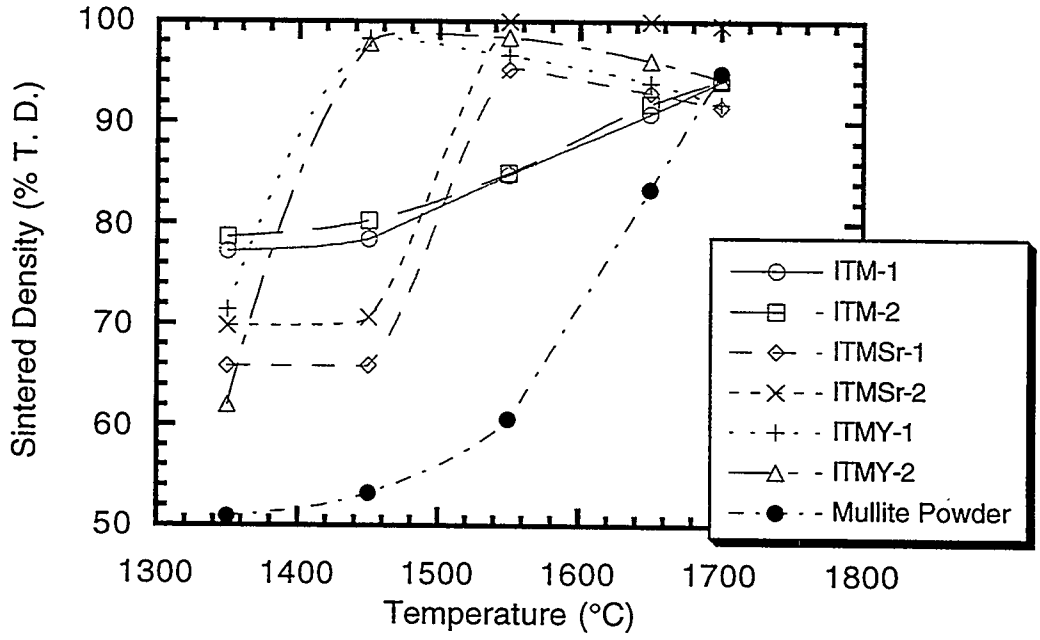

Fig. 1. Summary of densification results on the seeded mullite compositions.

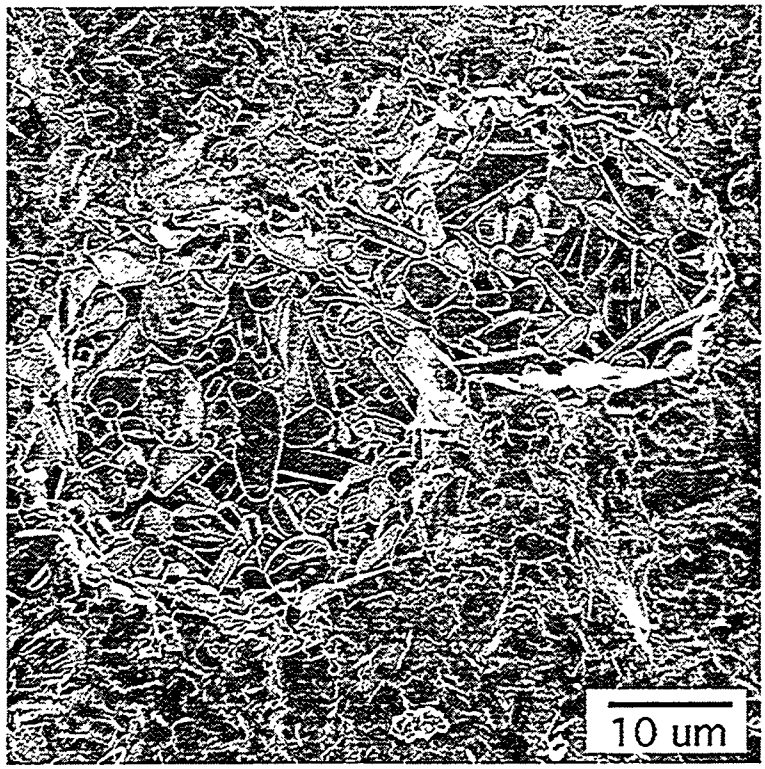

Fig. 2. Fracture surface of ITM-Sr-1 sintered at 1600°C for 15 h.

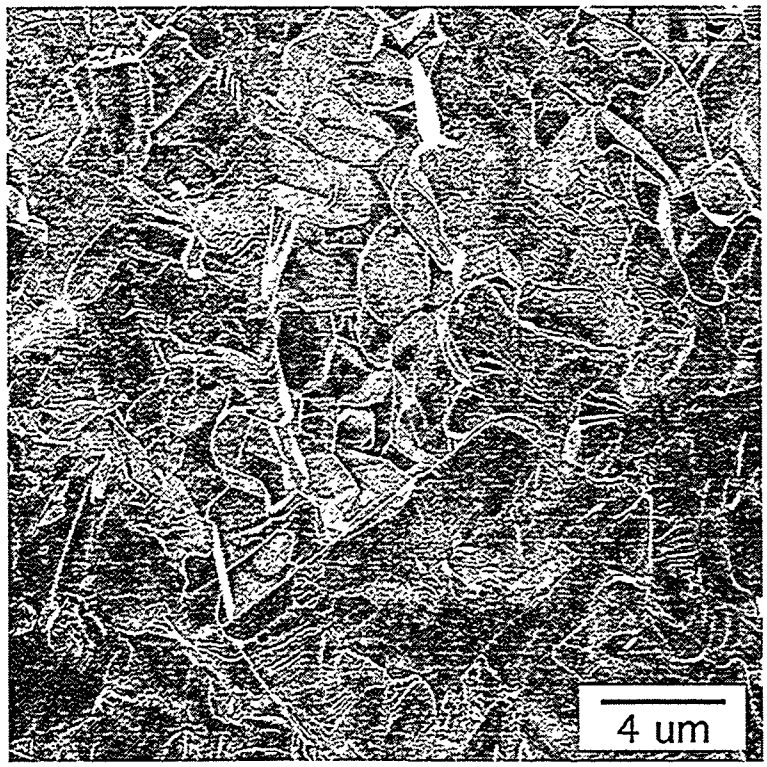

Fig. 3. Fracture surface of ITM-Sr-2 sintered at 1600°C for 15 h.

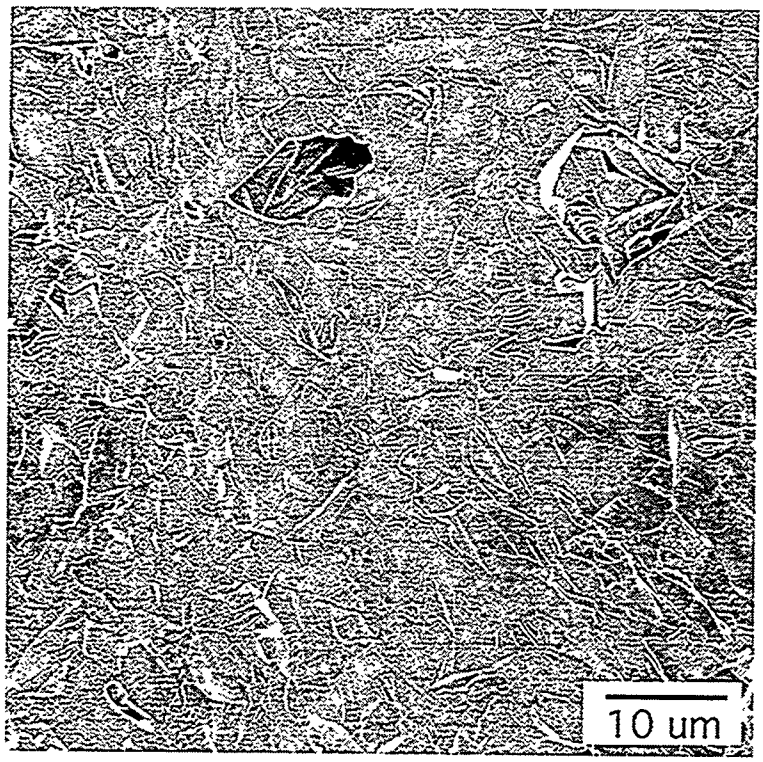

Fig. 4. Fracture surface of ITM-Y-1 sintered at 1600°C for 15 h.

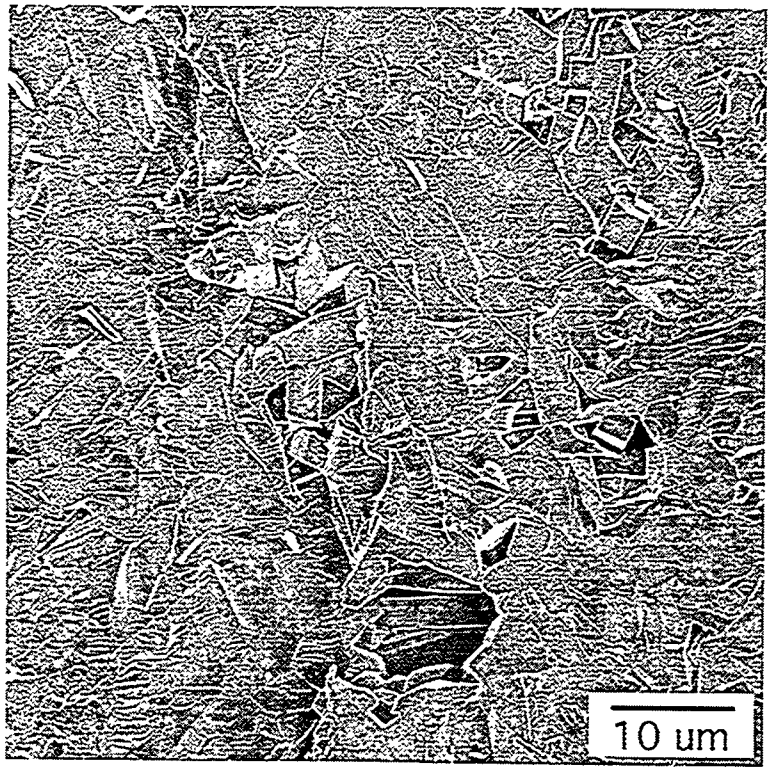

Fig. 5. Fracture surface of ITM-Sr-1 sintered at 1600°C for 15 h.

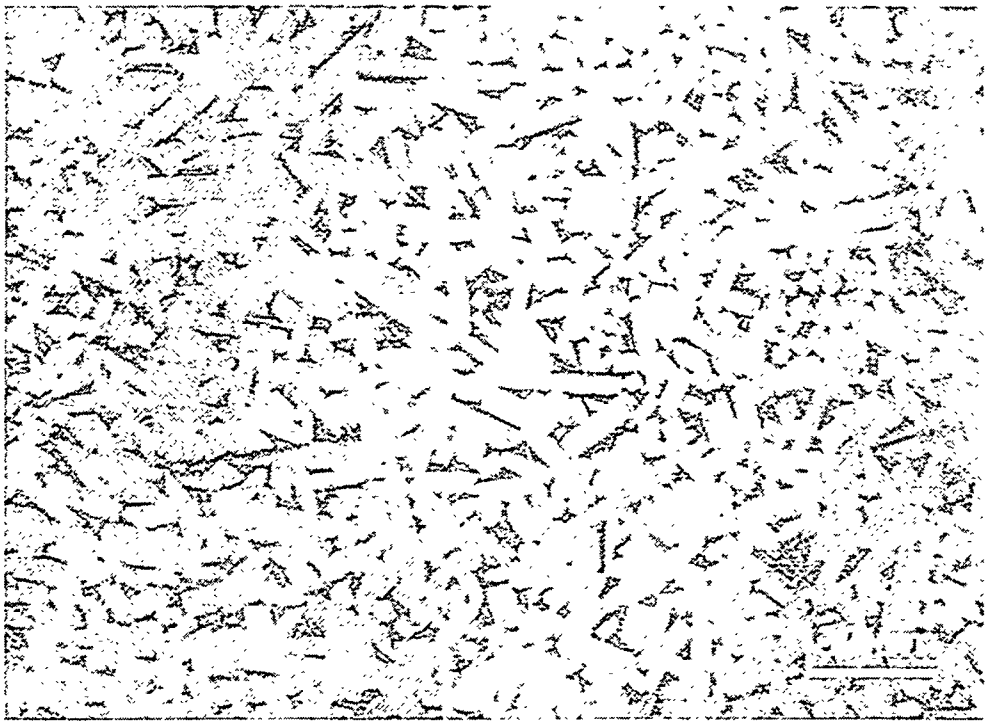

Fig. 6. Polished and etched Fe-doped mullite composition exhibiting anisotropic grain growth.

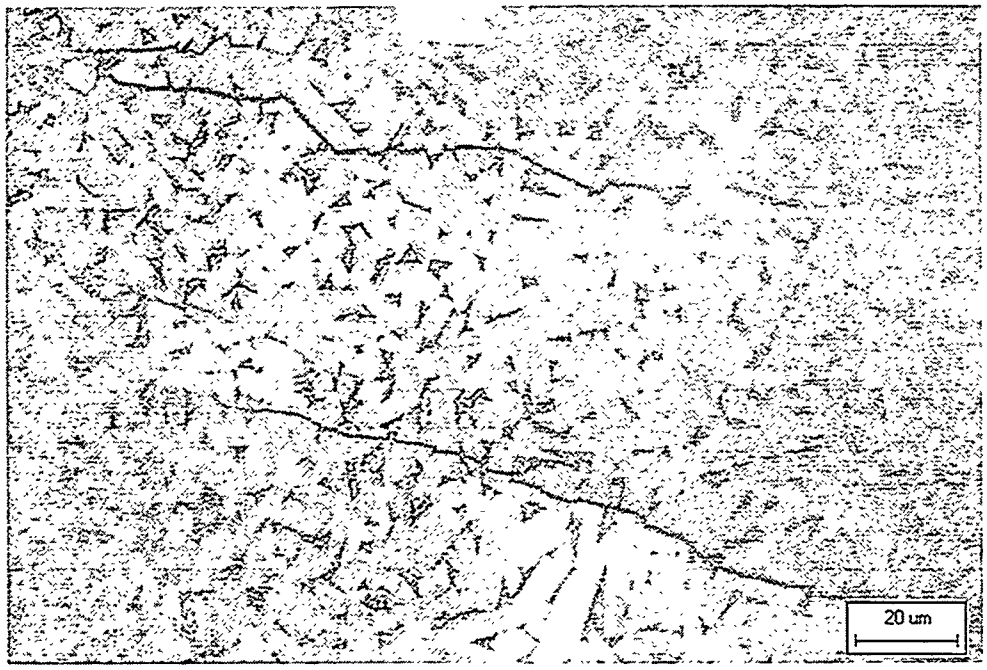

Fig. 7. Crack growth in a Fe-doped mullite composition showing mostly transgranular crack propagation.

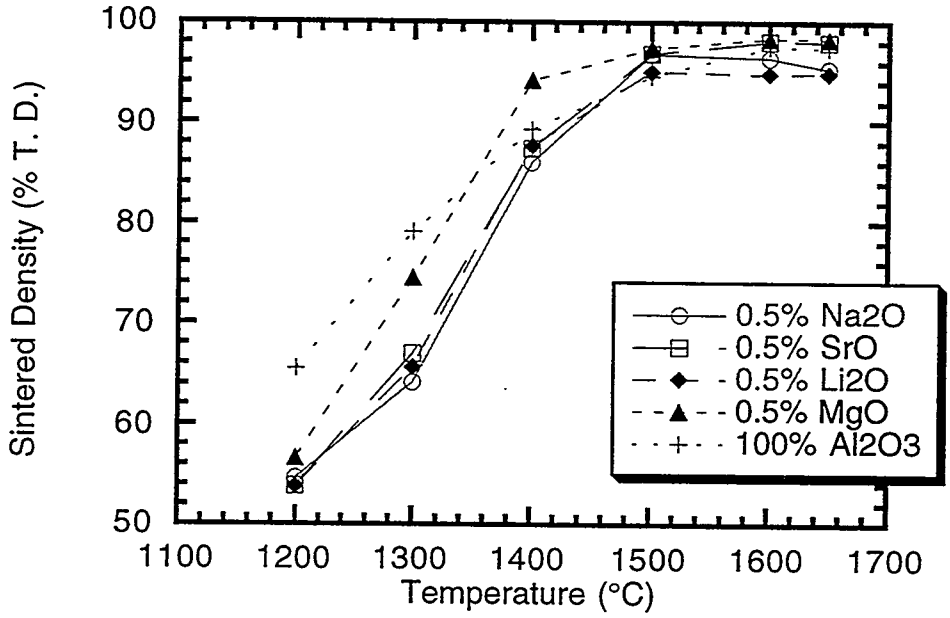

Fig. 8. Summary of densification results on the doped alumina compositions.

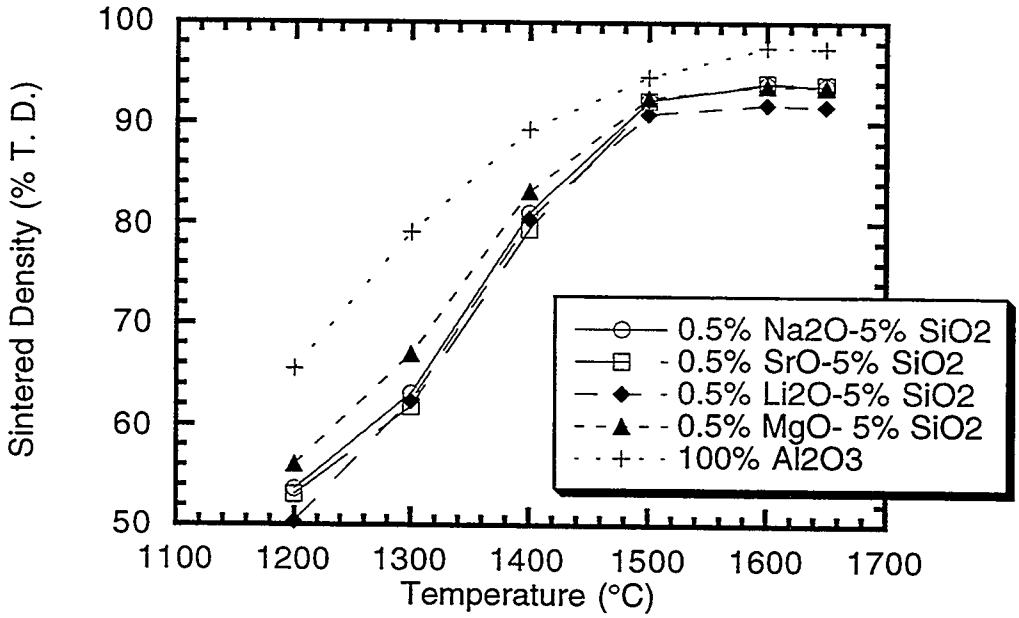

Fig. 9. Summary of densification results on the doped alumina compositions.

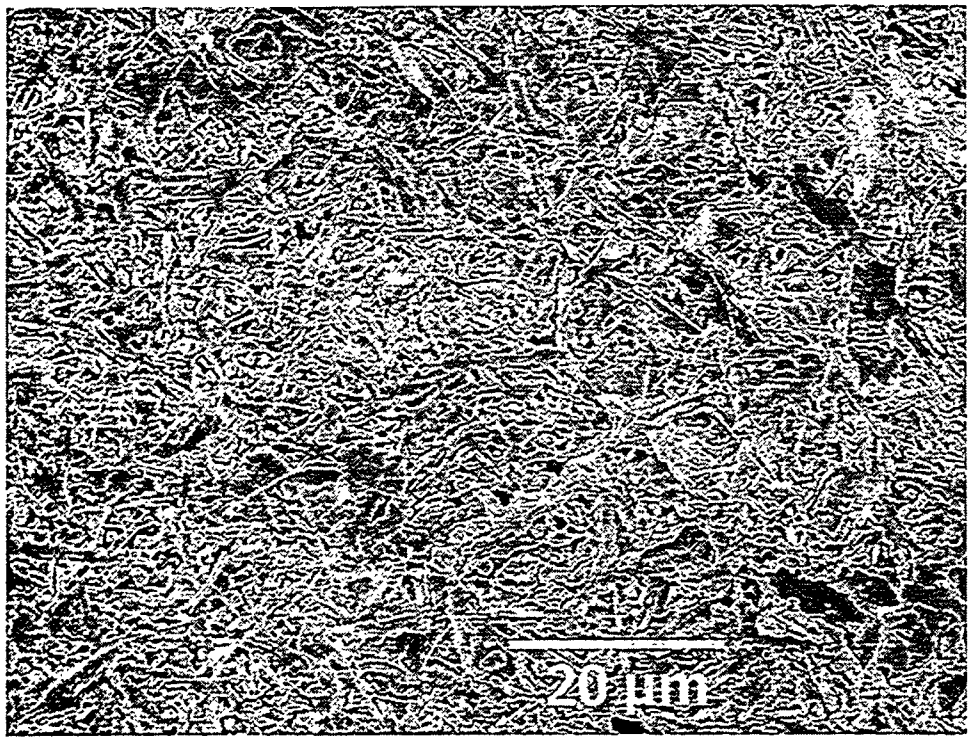

Fig. 10. Alumina-10% Na_2O composition exhibiting anisotropic grain growth.

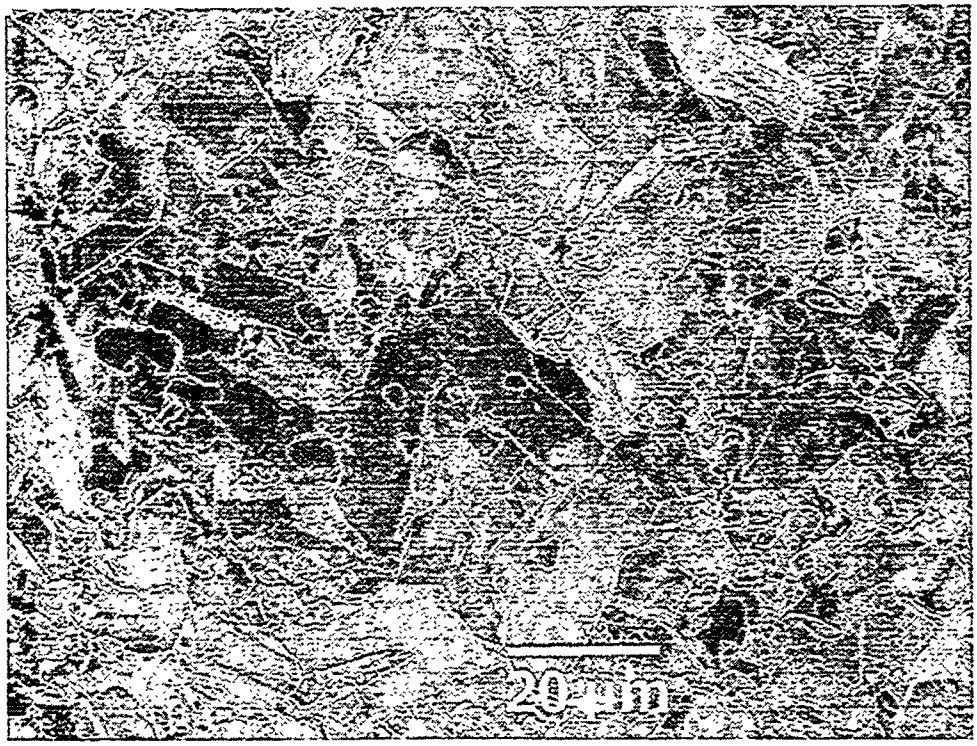

Fig. 11. Alumina-5% Na_2O-5% SiO_2 composition exhibiting anisotropic grain growth.

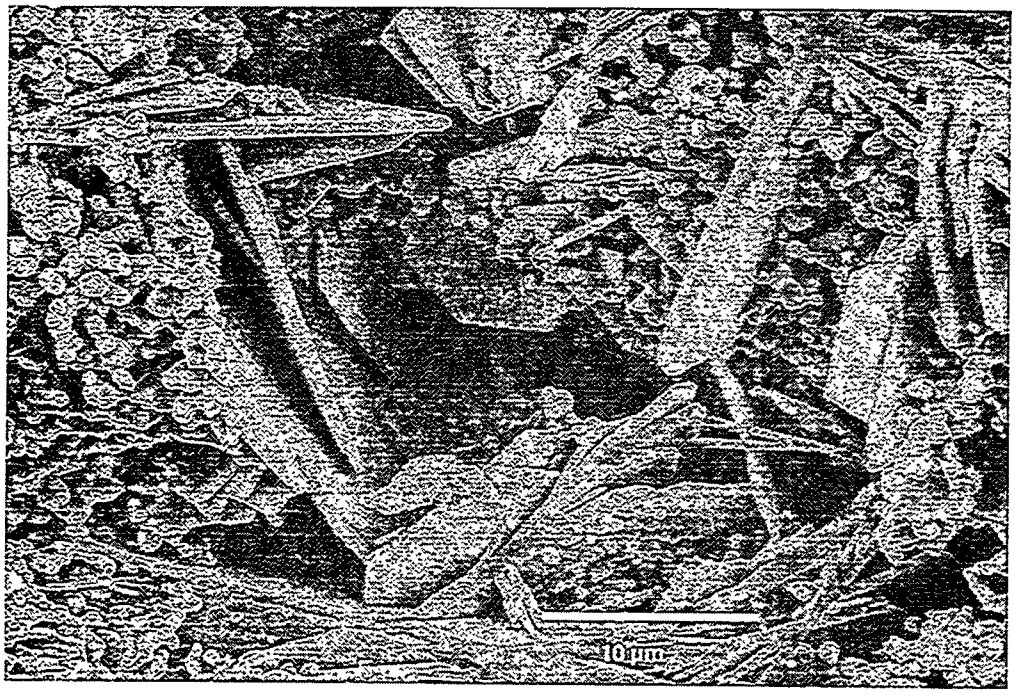

Fig. 12. Alumina-4.5% Na_2O-0.5 Na_2AlF_6 composition exhibiting anisotropic grain growth.

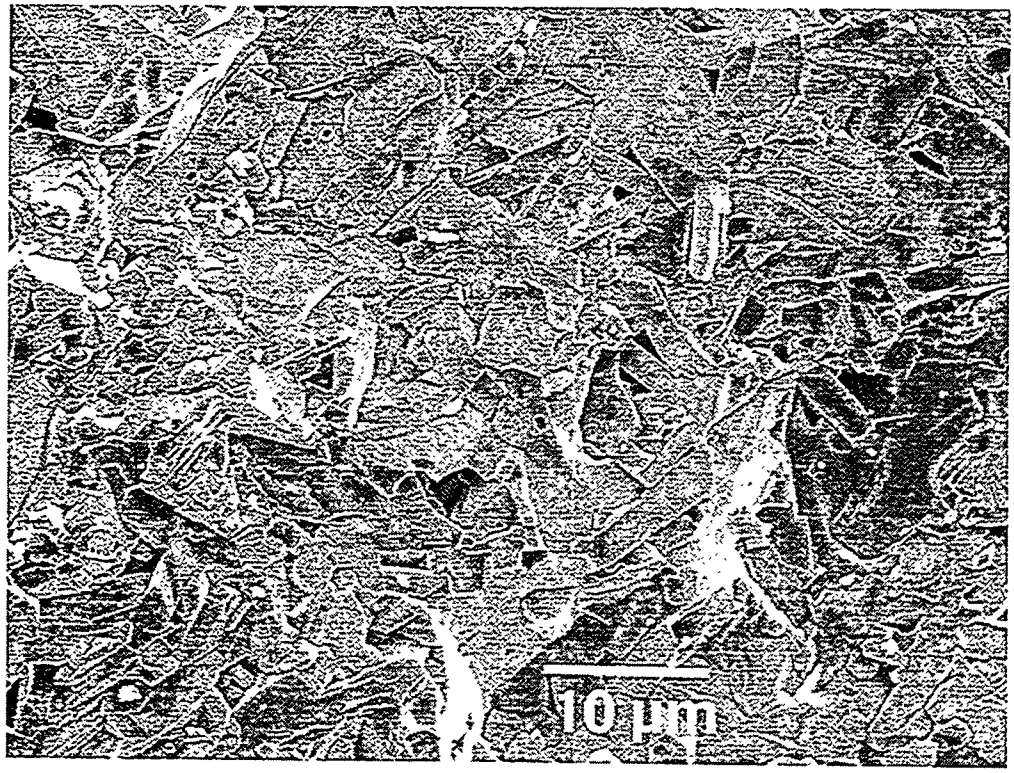

Fig. 13. Alumina-5% La_2O_3 composition exhibiting anisotropic grain growth.

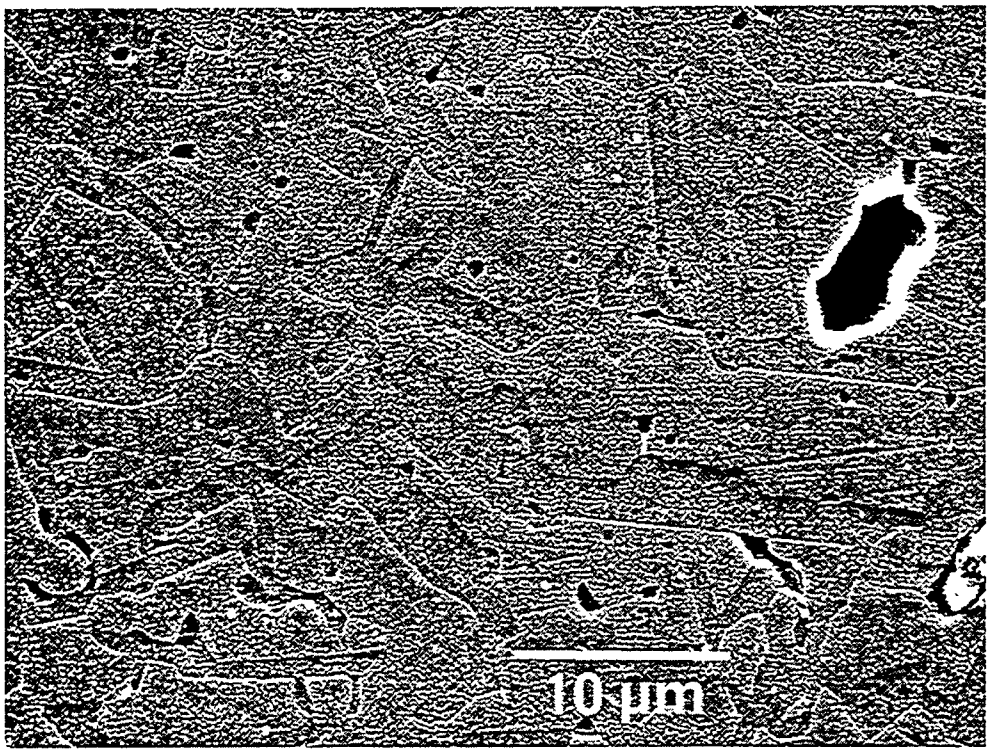

Fig. 14. Polished and etched alumina-5% Na_2O composition exhibiting anisotropic grain growth.

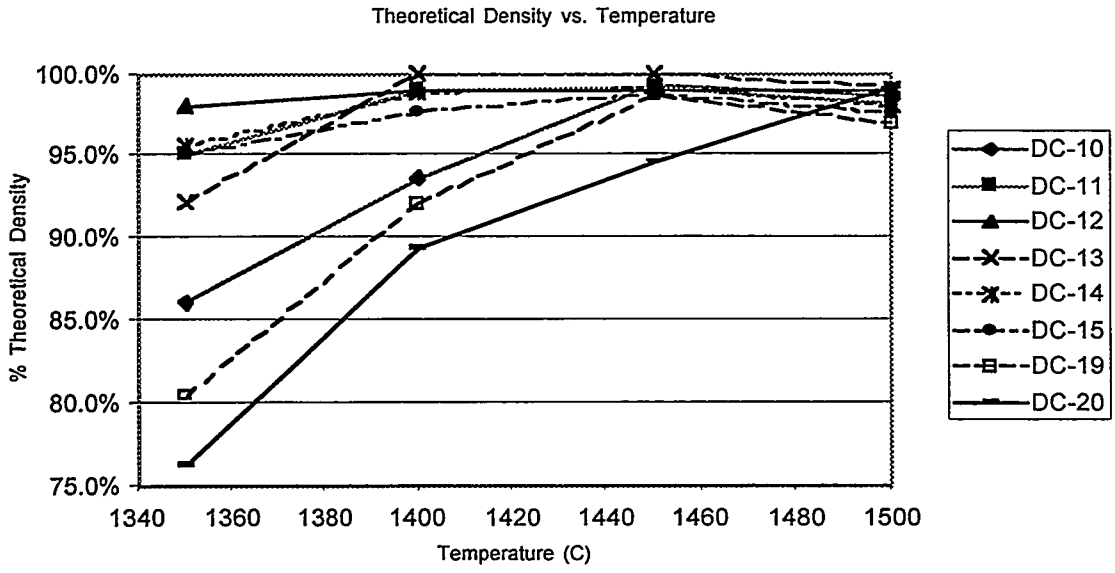

Fig. 15. Summary of densification behavior of Ni_3Al-bonded TiC composites.

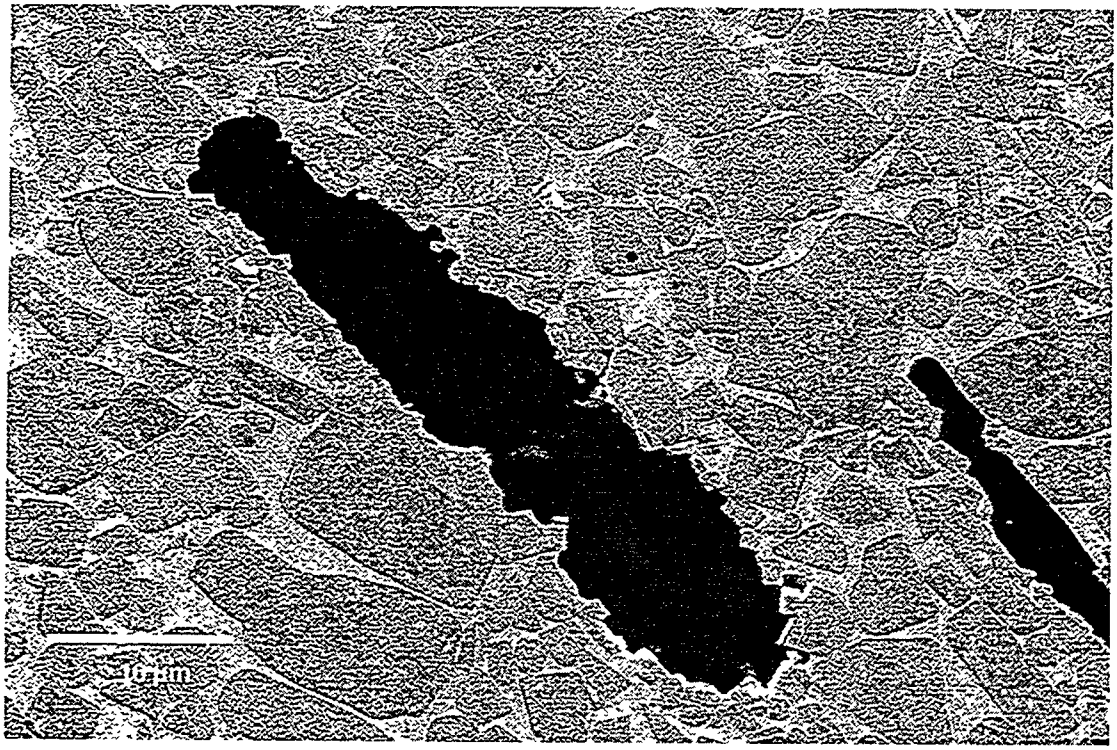

Fig. 16. Microstructure of TiC-30 vol. % Ni_3Al fabricated by sintering with prealloyed Ni_3Al. Large pore was remnant from large prealloyed Ni_3Al powders.

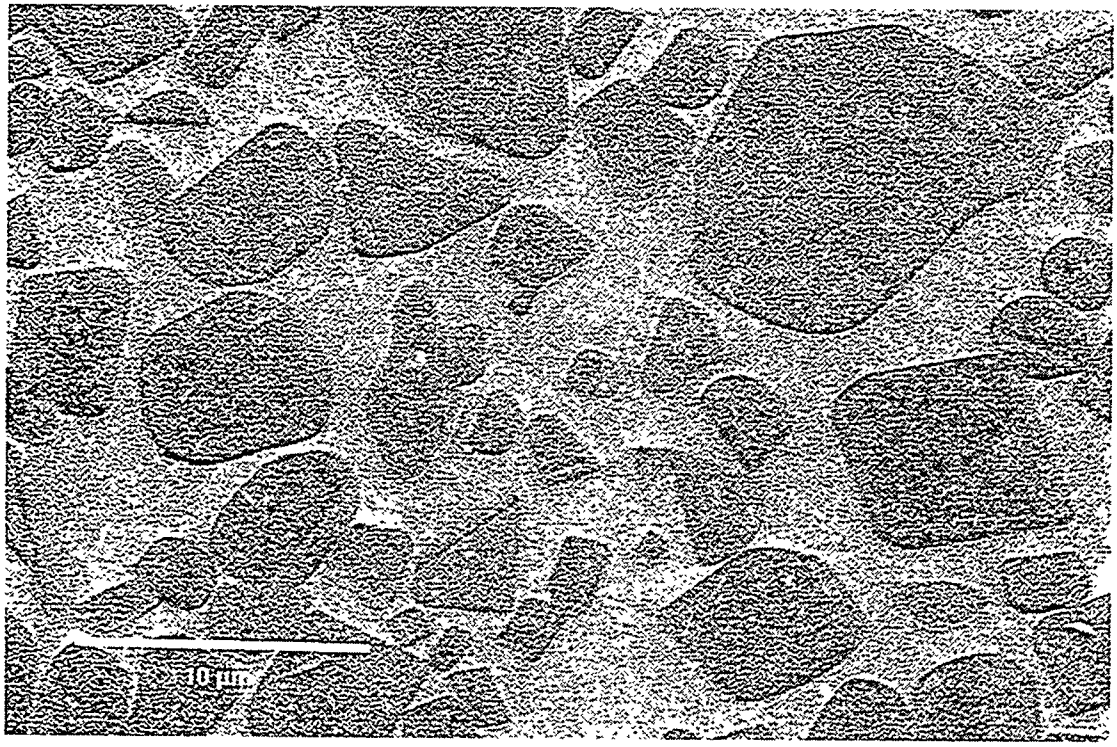

Fig. 17. Microstructure of TiC-40 vol. % Ni_3Al fabricated by sintering with prealloyed Ni_3Al. TiC particles exhibit a 'core-and-rim' morphology caused by reaction of the liquid Ni_3Al with the TiC.

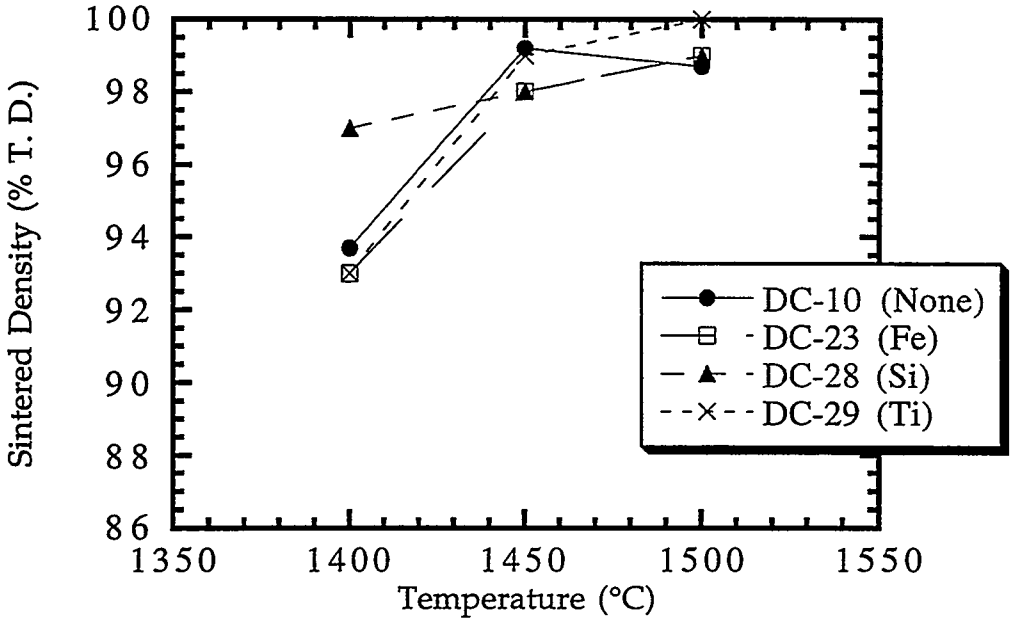

Fig. 18. The effect of alloying additives (Fe, Si and Ti) on the sintering behavior of the aluminide-bonded TiC. All samples fabricated with 30 vol. % of the Ni_3Al binder phase by reaction sintering of elemental powders.

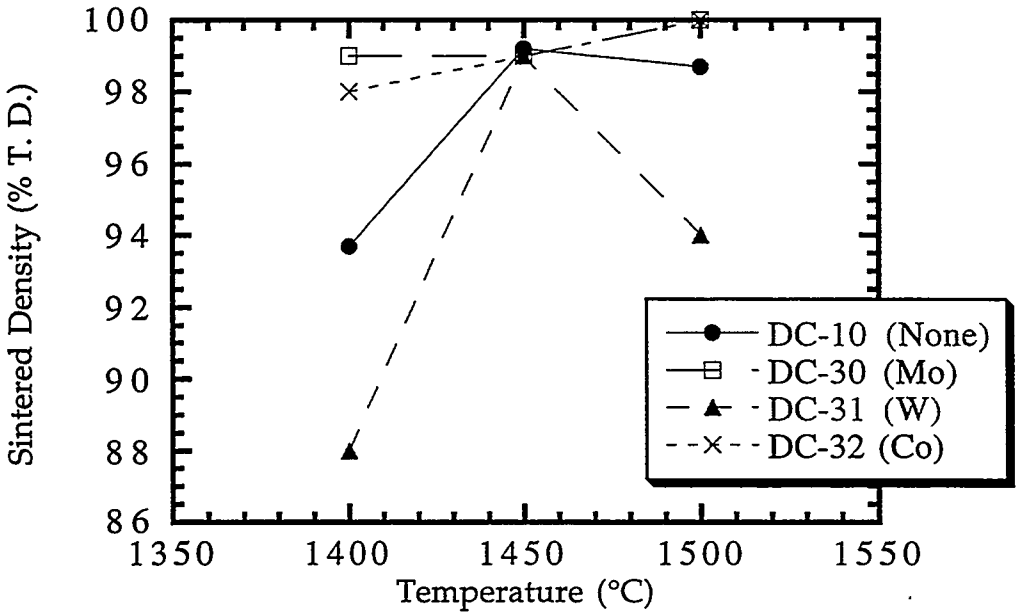

Fig. 19. The effect of alloying additives (Mo, W, and Co) on the sintering behavior of the aluminide-bonded TiC. All samples fabricated with 30 vol. % of the Ni_3Al binder phase by reaction sintering of elemental powders.

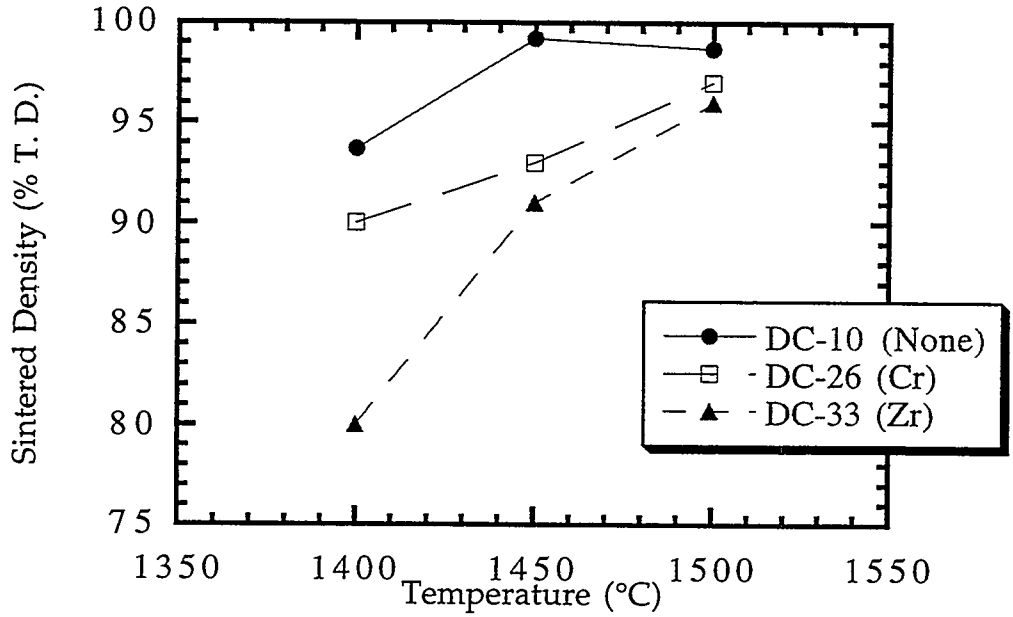

Fig. 20. The effect of alloying additives (Cr and Zr) on the sintering behavior of the aluminide-bonded TiC. All samples fabricated with 30 vol. % of the Ni_3Al binder phase by reaction sintering of elemental powders.

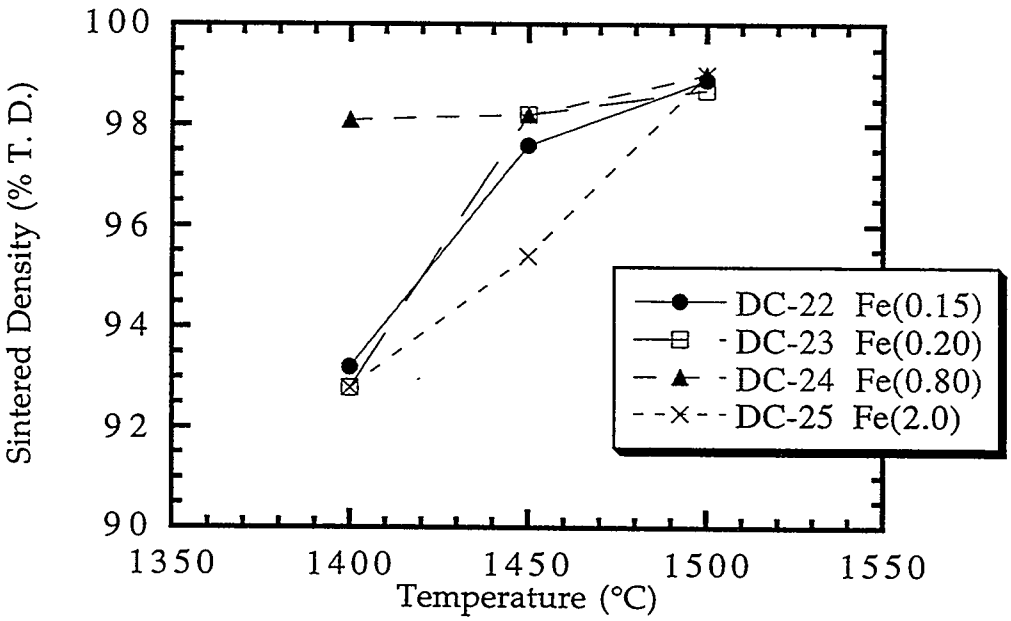

Fig. 21. The effect of various Fe alloying additive contents on the sintering behavior of the aluminide-bonded TiC. All samples fabricated with 30 vol. % of the Ni_3Al binder phase by reaction sintering of elemental powders.

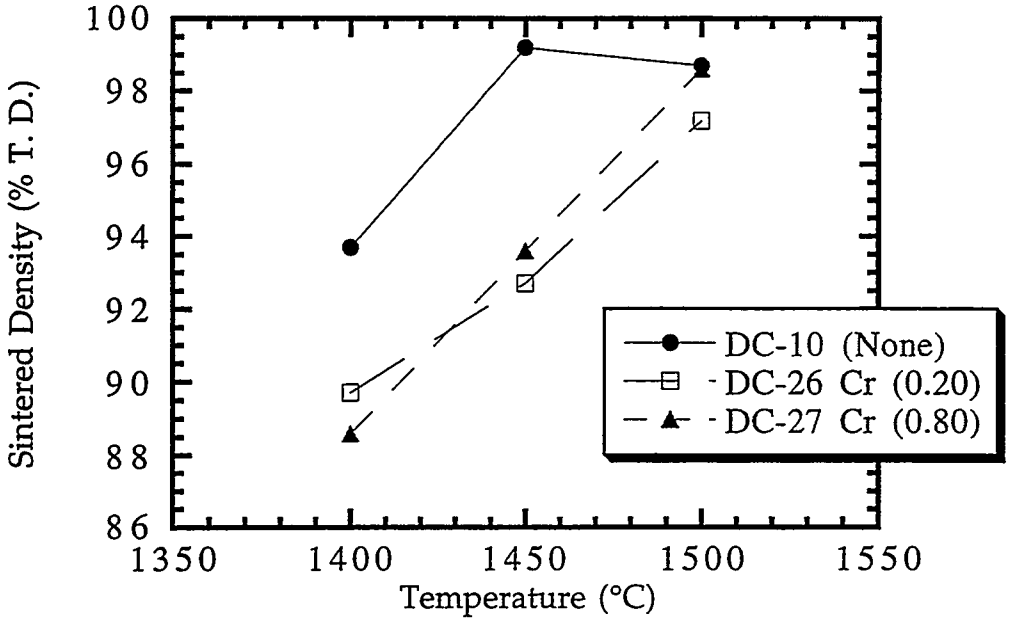

Fig. 22. The effect of various Cr alloying additive contents on the sintering behavior of the aluminide-bonded TiC. All samples fabricated with 30 vol. % of the Ni_3Al binder phase by reaction sintering of elemental powders.

Cost Effective Sintering of Silicon Nitride Ceramics (SIU-C)-
D. E. Wittmer, Southern Illinois University, Carbondale, IL 62901

Objective/Scope

The purpose of this work is to investigate the potential of cost effective sintering of Si_3N_4 through the development of continuous sintering techniques and the use of lower cost Si_3N_4 powders and sintering aids. The addition of a recent task has added the objective of investigating the cost effective sintering of advanced carbides and cermets.

Technical Highlights

Task 1. Refine Economic Model and Design for Chosen Furnace Configuration

This task was completed as reported in a previous semiannual report.

Task 2. Continue evaluation of sintering parameters on properties of selected Si_3N_4 compositions

Prototype Belt Furnace

The graphite hot zone was installed in the Model 44-BF belt furnace, during this reporting period. The temperature controls are presently being calibrated, since the graphite hot zone utilizes both retractable thermocouples and pyrometers for temperature control. The long thermocouple used to measure the temperature profile of the furnace, which in turn is used to calculate the heating rate/zone configuration/belt speed relationships, was found to be defective during the first heat. This thermocouple has been returned to the manufacturer for replacement, and it is expected that the temperature profile will be mapped during the next reporting period. The furnace control thermocouples continue to read over 200°C lower than the optical pyrometers. It is believed that this is because the line of sight of the pyrometers is directed at the radiant glow of the element. The result is that the pyrometers cannot be used to correctly control the furnace temperature without the establishment of the true temperature off-set. This situation has been reported to CVI and they are working on a design fix.

During this reporting period, temporary insulation was added at the ends of the furnace's water cooled jail assembly. This insulation has dropped the furnace top temperature, but it is still well outside of the design operation limit as specified by CVI. CVI is still in the process of redesigning the jail assembly and insulation package to enable the furnace to run within the correct safety and design. This was expected to be completed during this reporting period, but has not yet been completed by CVI.

1. Collaboration with Industrial Partners and Affiliates

Norton Advanced Ceramics

The additional funds that were requested by NAC to continue investigations involving sintering warpage and consistency of the exhaust valves under the ACMT contract have been approved. In this program extension, some smaller valves were sintered and were returned to NAC for evaluation. The conditions and data have been supplied to NAC for incorporation in the ACMT report. Initial evaluations indicate that sintering in the graphite hot zone is comparable to the tungsten hot zone, so long as the same BN boats are used.

Allied Signal, Inc.

No activity to report during this reporting period.

Caterpillar Tractor Company

No activity to report during this reporting period.

Kennametal, Inc.

Kennametal has shown an interest in using continuous sintering for parts other than cutting tools. Initial discussions have centered around cooperation between Kennametal/SIU/ORNL/Other Industries. It is hoped that other industries will be identified during the next reporting period and proposals/CRADA's can be established during this fiscal year.

2. Silicon Nitride Valves for SAE Car

Previously 32 small valves of NT451 were received from Norton Company and were then remachined by Chand Kare into 16 exhaust and 16 intake valves that would fit a Honda 600 cc racing motorcycle engine. These valves constituted 2 full sets of valves. Jim Newton, a student researcher in the advanced ceramics group at SIU, conducted the valve spring evaluation and retrofitted his Honda CBR600 with one set of these valves. A dynamometer test was conducted on the engine prior to the installation of the silicon nitride valves. Another set of dynamometer runs will be conducted to determine any inherent improvement in horsepower and torque and the effected of the valves on the shape of the power and torque curves. This information will be utilized in the future by the SIU-SAE Car team for modification of the Honda 600 cc engine used in the SAE car. At present the engine has over 2,000 road test miles on the silicon nitride valves and has been driven on an official race track.

4. Evaluation of Continuous Sintering of Silicon Nitride-Titanium Carbide

As reported previously, during the last reporting period, 3 lots of Ube silicon nitride containing 5 wt% TiC (H. C. Starck high purity grade) were processed in the A3Y9 composition. The test bars have been received from Chand Kare and the physical properties which have been determined are listed in Table I.

As seen in this table, none of the formulations achieved high density at the temperatures normally used to sinter the A3Y9 formulation. This was because the TiC converts to TiN at elevated temperatures, causing out-gassing of CO. At low sintering temperatures, moderately high densities have been achieved. The strength and toughness values measured for the TC3 are comparable to some commercial silicon nitride products. These values are expected to improve with increase in density. Because of the TiC conversion to TiN, TiN substitution for TiC is also being investigated.

During this reporting period, 2 addition lots A3Y9 using Ube silicon nitride containing 5 wt% TiC (H. C. Starck high-purity grade and a high-purity, ultra-fine grade of TiC produced by Dr. R. Koc at SIUC with funding from DoE) and 1 lot of A3Y9 using Ube silicon nitride containing 5 wt% TiN (H. C. Starck high-purity grade) were processed. These lots will be sintered along with the baseline A3Y9 formulation during the next reporting period.

Task 3. Continue Evaluation of Low Cost Si_3N_4 Powders

Nothing to report this reporting period.

Task 4. Design and Construct Prototype Belt Furnace

This task has been completed.

Task 5. Continuous Sintering of Inter-metallic Bonded Carbides

During this reporting period, the 13 formulations of inter-metallic bonded carbides prepared by Terry Tiegs at ORNL were continuous sintered in flowing nitrogen at 1450°C for 1h and 1400°C for 1 h. Following sintering the density and weight change for each formulation was determined and then the specimens were returned to ORNL. The sintering results are given in Table II(A) through (D). Because nitrogen was used, all of the formulations experienced a weight gain from the TiC to TiN conversion. It was hoped that because of the high heating rates achievable in the belt furnace that these composites could be liquid phase sintered with minimal reaction. ORNL is presently preparing more test materials for sintering in Ar during the next reporting period.

Status of Milestones

1.	Refine Economic Model and Design for Chosen Furnace Configuration	Completed
2.	Continue Evaluation of Sintering Parameters on Properties of Selected Si_3N_4 Compositions	On Schedule Continuing
3.	Continue Evaluation of Low Cost Si_3N_4 Powders	On Schedule Continuing
4.	Design and construct prototype belt furnace	Completed
5.	Continuous sintering of inter-metallic bonded carbides	On Schedule

Problems Encountered

None

Publications and Presentations

D. E. Wittmer, "Processing of Silicon Nitride for Commercial Applications," Presentation at the SAE Earthmover Conference and Exposition, Peoria, IL, April 8-10, 1998.

Dale E. Wittmer, Steven P. Etherton and Per Magnus Holgesson, Southern Illinois University, Carbondale, IL 62901-6603 USA, and Mike McGown and James Kellogg Centorr Vacuum Industries, Inc., Nashua, NH 03062-3126 USA, "The Influence of Continuous Sintering on the Properties of Si_3N_4," Presented at International Symposium on Nitrides II, Limerick, Ireland, June 9-12, 1998. To be published by Trans Tech Publications Ltd., Zurich, Switzerland.

Table I. Continuous Sintering Results for A3Y9-TiC Using Commercial TiC

Designation	Sintering Conditions		% Theor. Density	4-Pt. Flexural Strength (MPa)
	Temperature (°C)	Time (min)		
Baseline Silicon Nitride A3Y9 Formulation	1790 1775	120 120	100 99.8	953 +/- 52 **
TC1 95/5 As-received TiC Granulated & CIP'ed	1750 1725 1700	120 120 120	90.1 90.9 91.6	526 +/- 25 464 +/- 31 482 +/- 42
TC2 95/5 Pre-milled TiC Granulated & CIP'ed	1750 1725 1700	120 120 120	91.0 91.2 91.6	510 +/- 44 437 +/- 97 485 +/- 27
TC3 95/5 Pre-milled TiC Pressure Cast & CIP'ed	1700 1725	120 120	91.3 94.4	704 +/- 67 **

** Data not yet completed.

The commercial TiC was provided by H. C. Starck for evaluation purposes.

Table II(A). Continuous Sintering Results for Inter-metallic bonded TiC Composites 1450°C/1 h

Sample ID	Matrix/% Binder Type	Apparent Density (g/cc)	Bulk Density (g/cc)	Apparent Porosity (%)	Percent Weight Change (%)	Percent Target Density (%)
DC-1	TiC/20% Ni+NiAl+B	5.19	3.23	37.7	7.79	62.24%
DC-2	TiN/20% Ni+NiAl+B	5.54	3.95	28.7	0.85	71.30%
DC-3	Ti(C,N)/20 Ni+NiAl+B	5.51	3.78	31.4	2.01	68.60%
DC-4	TiC/20 Ni+NiAl+ZrNi	5.28	2.92	44.7	9.42	55.30%
DC-5	TiC/20 Fe+Al+B	Bloated	Bloated	Bloated	6.00	Bloated

Table II(B). Continuous Sintering Results for Inter-metallic bonded TiC Composites 1450°C/1 h

Sample ID	Matrix/% Binder Type	Apparent Density (g/cc)	Bulk Density (g/cc)	Apparent Porosity (%)	Weight Change (%)	Target Density (%)
DC-10	TiC/30 Ni3Al (IC-50)	5.15	3.76	27.0	7.3	66.20%
DC-11	TiC/40 Ni3Al (IC-50)	5.54	4.04	27.1	6.5	68.13%
DC-12	TiC/50 Ni3Al (IC-50)	5.89	4.46	24.2	5.4	72.05%
DC-13	TiC/30 Ni3Al RS	5.01	4.92	1.8	2.5	87.23%
DC-14	TiC/40 Ni3Al RS	5.36	5.25	2.2	2.5	89.29%
DC-15	TiC/50 Ni3Al RS	5.55	5.45	1.8	2.8	89.05%
DC-19	TiC/30 Fe-40Al PA	4.62	4.07	11.8	10.2	77.67%
DC-20	TiC/30 Fe-40Al RS	4.69	3.86	17.8	7.8	76.13%

PA = Pre-alloyed Powder RS = Reaction Sintered Powder

Table II(C). Continuous Sintering Results for Inter-metallic bonded TiC Composite 1400°/1 h

Sample ID	Matrix/% Binder Type	Apparent Density (g/cc)	Bulk Density (g/cc)	Apparent Porosity (%)	Percent Weight Change (%)	Percent Target Density (%)
DC-1	TiC/20% Ni+NiAl+B	5.10	3.24	36.4	7.8	63.53%
DC-2	TiN/20% Ni+NiAl+B	5.54	3.92	29.3	1.2	70.76%
DC-3	Ti(C,N)/20 Ni+NiAl+B	5.46	3.76	31.1	1.7	68.86%
DC-4	TiC/20 Ni+NiAl+ZrNi	-----	-----	-----	-----	-----
DC-5	TiC/20 Fe+Al+B	----	-----	-----	-----	-----

Table II(D). Continuous Sintering Results for Inter-metallic bonded TiC Composites 1400°C/1 h

Sample ID	Matrix/% Binder Type	Apparent Density (g/cc)	Bulk Density (g/cc)	Apparent Porosity (%)	Weight Change (%)	Target Density (%)
DC-10	TiC/30 Ni3Al (IC-50)	5.03	3.67	27.0	6.6	64.61%
DC-11	TiC/40 Ni3Al (IC-50)	5.41	3.89	28.0	6.7	65.60%
DC-12	TiC/50 Ni3Al (IC-50)	5.85	4.32	26.1	5.9	69.79%
DC-13	TiC/30 Ni3Al RS	5.07	4.58	9.8	2.9	81.21%
DC-14	TiC/40 Ni3Al RS	5.22	4.74	9.1	3.4	80.61%
DC-15	TiC/50 Ni3Al RS	5.40	4.88	9.8	4.6	79.74%
DC-19	TiC/30 Fe-40Al PA	4.70	4.04	13.9	11.2	77.10%
DC-20	TiC/30 Fe-40Al RS	4.90	3.75	23.5	9.6	73.96%

PA = Pre-alloyed Powder RS = Reaction Sintered Powder

W.B.S. Element 1.2.4.3
CHARACTERIZATION AND TESTING OF LOW-EXPANSION CERAMIC MATERIALS

V. M. Vaubert, K. Breder, and D. P. Stinton

Objective/Scope

Insulated exhaust portliners are needed in advanced diesel engines to increase engine efficiency by increasing the combustion temperatures and reducing the combustion heat that is lost through the head and into the water cooling system. Low-expansion materials have a potential for this application due to their very low thermal conductivity, extraordinary thermal shock resistance, and reduction of attachment stresses. Thermal shock resistance is critical because the complex shape of the portliners requires that they be cast into the metallic cylinder head. Functioning exhaust portliners are inaccessible after they are cast into cylinder heads, hence, must not require maintenance for the life of the head (~1 million miles). A contract has been placed with LoTEC, Inc. to develop cost-effective processes for the fabrication of portliners. LoTEC is investigating $Ba_{1+x}Zr_4P_{6-2x}Si_{2x}O_{24}$ (BS-25) and $Ca_{1-x}Sr_xZr_4P_6O_{24}$ (CS-50). Oak Ridge National Laboratory (ORNL) is assisting with the characterization and evaluation of the above compositions.

Technical Highlights

Casting of low-expansion ceramic portliners into cast iron requires a compliant layer that insulates the portliner from the high temperatures and absorbs clamping stresses that are created by the metal as it cools. Clamping stresses result because the coefficient of thermal expansion (CTE) of the metal is many times more than that of the ceramic. Straight-wall portliners have been successfully cast into aluminum without any compliant layer because of the low aluminum melting point. An investigation to evaluate the effect of three different portliners, two types of compliant layers and casting metal, on the casting behavior of ceramic portliners continued this period. The three variations of low-expansion portliners are a BS-25 material with a CTE of $1x10^{-6}$/°C, a low-modulus CS-50 material with a CTE of $3x10^{-6}$/°C, and a high-strength CS-50 material with a CTE of $3x10^{-6}$/°C. The two compliant layers being examined are a very porous, low-expansion ceramic that is fabricated at LoTEC and a fibrous material that is purchased commercially.

The iron-casts were cut open and the aluminum-casts were slowly melted to recover the liners. The ceramic tubes remained intact after this operation. Fifteen flexure bars were then machined from each tube for mechanical testing. Measurement of the mechanical properties of the liner materials and comparison to the as-fabricated materials should provide information on possible damage of the ceramic. Any degradation of the mechanical properties resulting from metal casting would indicate that the thermal stresses were too high.

Dynamic Young's modulus was measured with a grindo-sonic MK4I instrument according to ASTM standard C 1259-95. Fifteen samples were tested for each material and each

sample was measured 5 times. During the test, the specimens are excited mechanically by a strike and a transducer measures the resulting mechanical vibrations. The fundamental resonant frequency is then determined and used to calculate the dynamic Young's modulus with software Emod 9.10. The elastic modulus of the ceramics as a function of material's density is presented in Figure 1. It appears that the dynamic elastic modulus varies linearly as a function of density. No significant difference was observed between as received and cast materials. The history of the material did not affect its elastic mechanical behavior.

The samples were then broken in flexure using a four-point bending fixture (inner span 20 mm, outer span 40 mm). The fracture strength of the ceramics as a function of material's density is presented in Figure 2. The modulus of rupture also varies linearly as a function of density. No significant difference was observed between as received and cast materials.

The strength of ceramics is statistical in nature, depending on the probability that a flaw, severe enough to cause fracture at the given stress, is present in the volume of material. The Weibull modulus is a measure of the data scatter and thus the flaw size distribution; therefore it is believed that comparing the Weibull modulus of the different materials might indicate if they contained different types of flaws. In particular, we want to determine if metal casting generates microcracks in the liner. The Weibull curves generated from the strength data are presented in Figure 3 and Figure 4. No particular trend seems to link the type of metal casting, the nature of the compliant layer or even whether the liner was subjected to metal casting, to the Weibull modulus. Metal casting does not seem to have induced micro cracking of the liner.

One of the goals of the study is also to determine the best compromise between strength and ductility of the liner. A compliant material will deform as the metal contracts and the liner will experience less severe compressive stresses. On the other hand, smaller stresses might be sufficient to cause failure. An increase in the CS-50 strength is obtained by reducing the ceramic particle size prior to processing the slurry. Higher solids loading slips are then obtained, the green parts are denser, and shrinkage during drying and sintering is reduced. Computed tomographic analysis of the cast high-density and medium-density liners did not indicate which material was the most reliable. Likeliness of failure appears to be more influenced by the metal casting process and nature of the compliant layer than by the density of the ceramic liner. Hence, comparison between high and medium density CS-50 must be made in terms of reliability to determine the best material candidate. The value of the Weibull modulus for low-density samples is surprisingly high, since values larger than 20 usually correspond to very reliable materials. The Weibull theory was developed for high strength, brittle ceramics yet, the value of the average flexure strength of CS-50 is very low, and all the samples broke at stresses within a relatively small range of values. Since the Weibull modulus is the value of the slope when plotting the probability of failure (related to the number of specimen) versus $\ln(\sigma)$, where σ is the strength, $\Delta\ln(\sigma)$ will be small, therefore a high value of the Weibull modulus is found which does not necessarily indicate that the material is highly reliable.

As shown on Figure 4, the higher strength material does not either follow a Weibull distribution curve. Different families of flaws seem responsible for the material's failure. Examination of the fracture surface of the different samples helped to determine the nature of the flaws. Different types of crack initiation sites were found as summarized in Table 1 and some typical fracture surfaces are shown in Figure 5. Failure is often caused by the presence of large agglomerates for the medium-density samples and caused either by air bubbles, pores, medium or small agglomerates for the high-density material. A more controlled ceramic slurry and

casting process would result in the elimination of most of these flaws. Reduction of the agglomerate size and de-airing of the slurry prior to casting is needed. Small particle size, high quality CS-50 would be the best candidate for the port-liners. Also, as was discussed in earlier progress reports, the geometry of the ceramic liner must be very closely controlled, since variations in the wall thickness causes deformation of the ceramic liner during sintering and regions of stress concentration during metal casting. Additionally, metal casting needs to be very carefully monitored since air gaps in the metal cast were found during NDE evaluation and these regions corresponded to cracks in the liner.

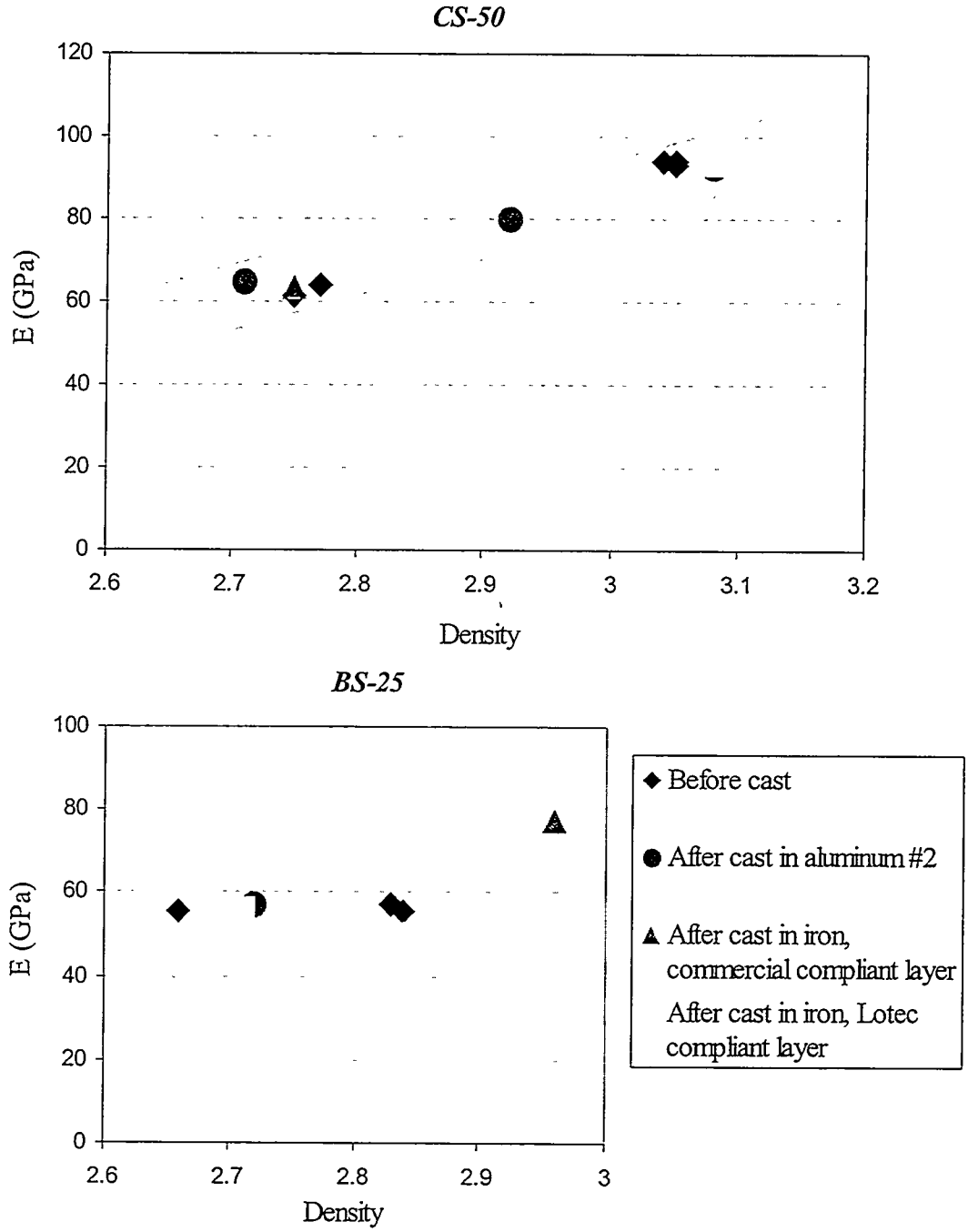

Remark: Error bars are not indicated on the graphs because they were smaller than the symbols.
X direction: Density ±0.01 Y direction: E ±2 GPa

Figure 1: Dynamic elastic modulus as a function of material's density for CS-50 and BS-25

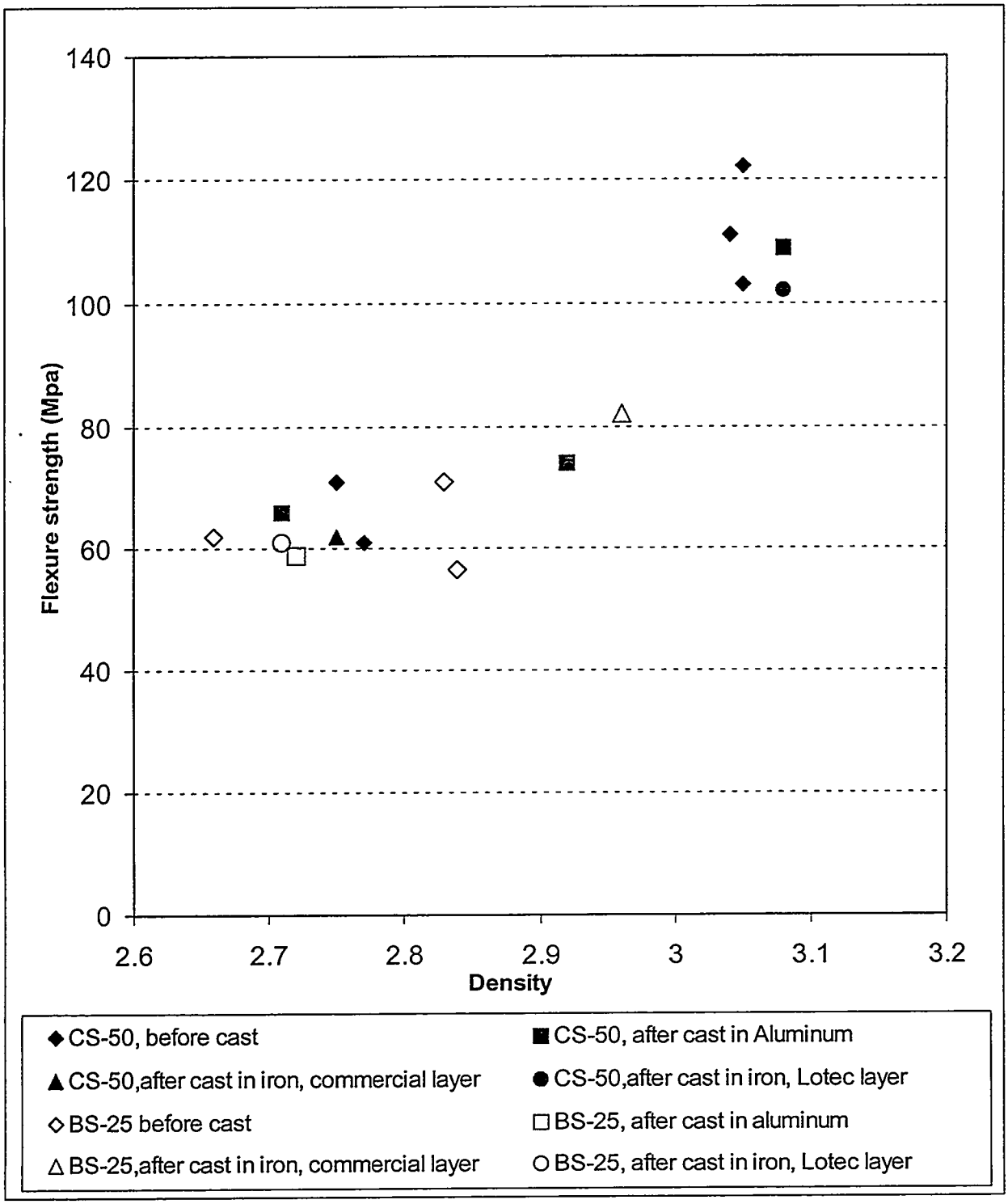

Figure 2: Flexure strength as a function of material's density for CS-50 and BS-25

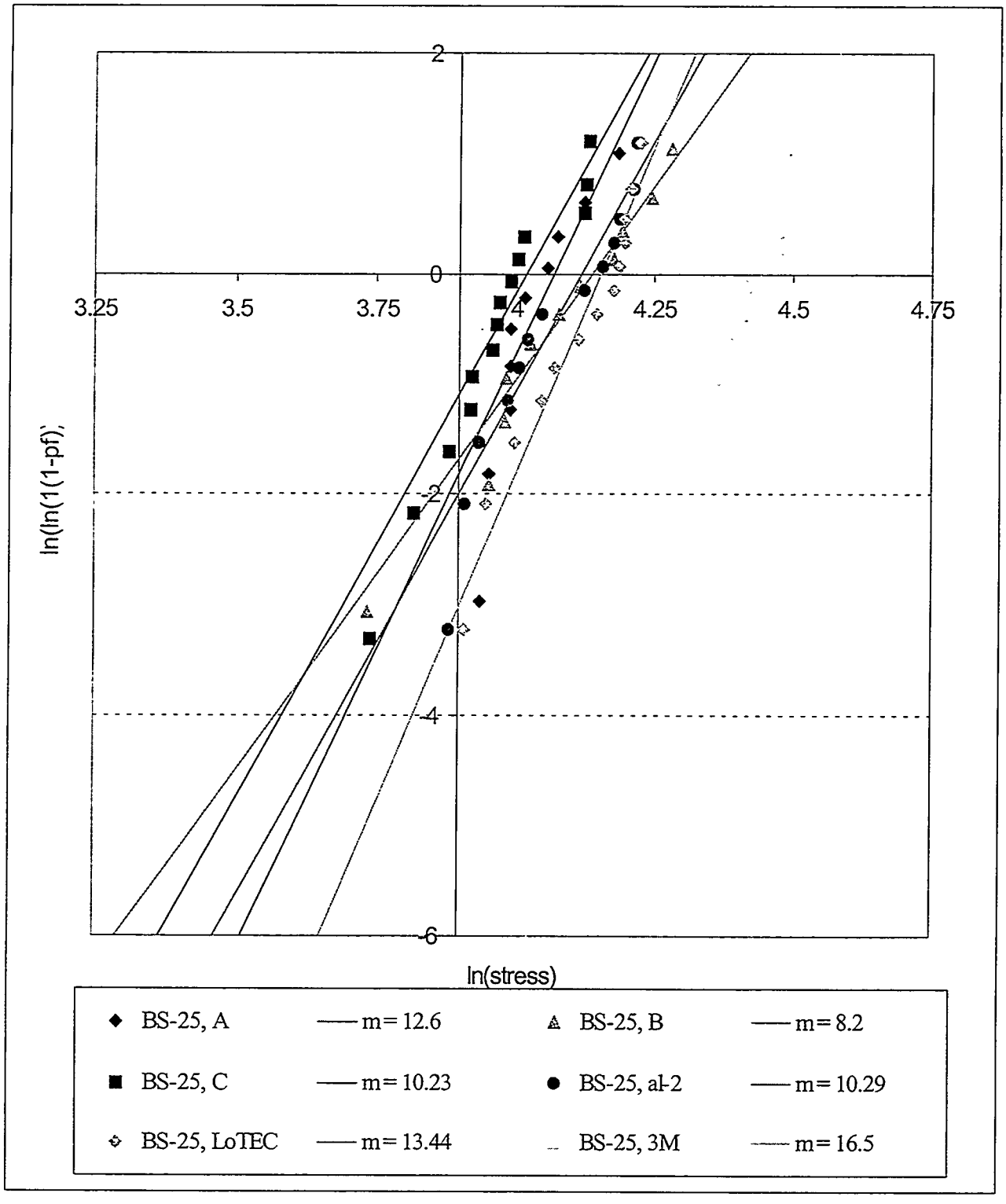

Figure 3: Weibull curves for BS-25

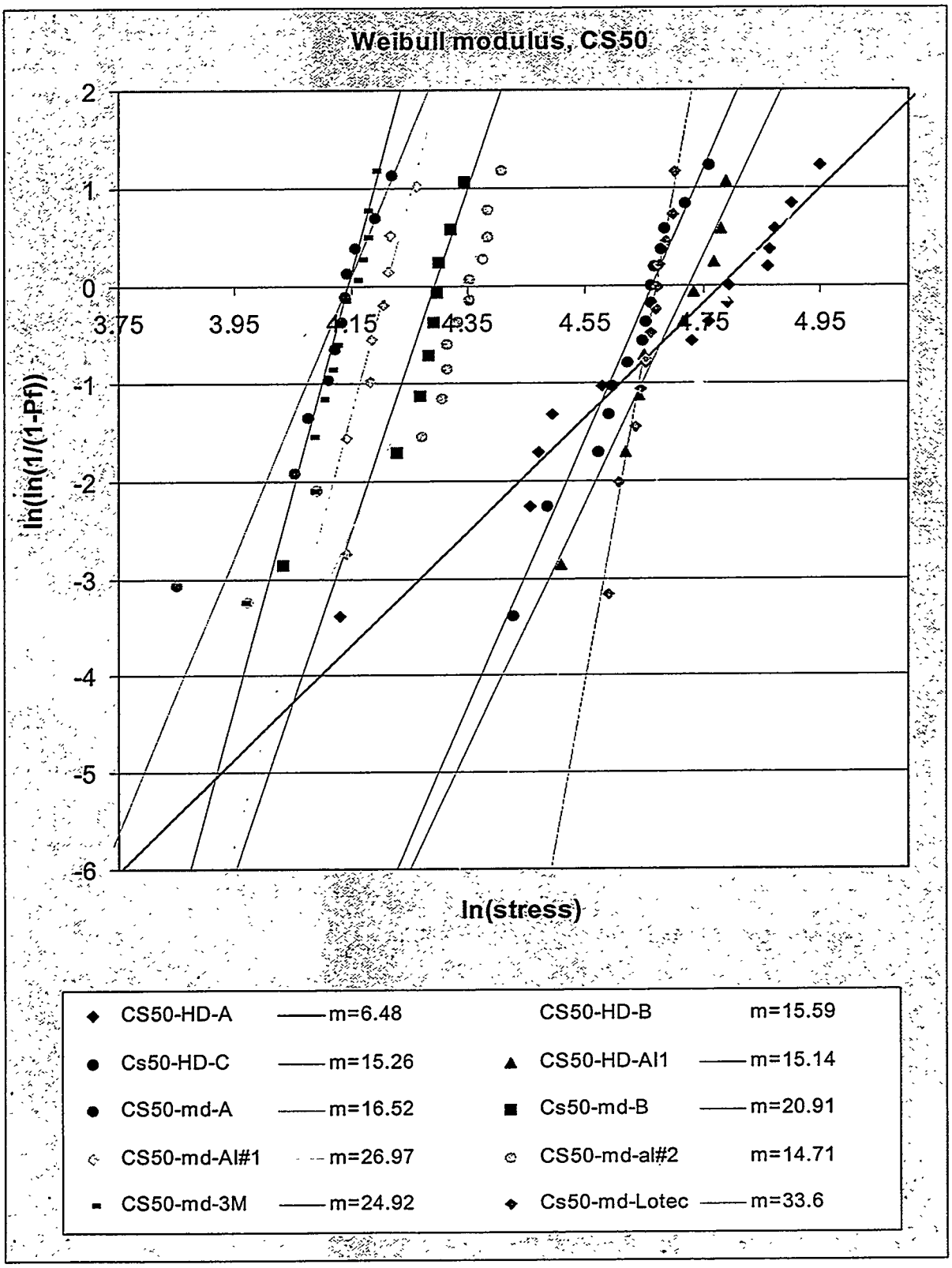

Figure 4:Weibull curves for CS-50

Material	Density	Average strength (Mpa)	Weibull Modulus	Typical fracture initiation site
CS-50 medium density, Aluminum cast, A	2.71	66	26.9	Big particles, grainy surface
CS-50, medium density, no cast, B	2.75	59	20.9	Big agglomerates, grainy surface, air bubbles
CS-50 medium density, iron cast, commercial compliant layer	2.75	63.2	24.92	Big agglomerates and air bubbles
CS-50, medium density, no cast, A	2.77	61	16.5	Big agglomerates, grainy surface
CS-50 medium density, Aluminum cast, B	2.92	74	14.7	Very grainy surface, and air bubbles
CS-50, high density, no cast, A	3.04	114	7.5	Many variations: very porous and dense regions
CS-50, high density, no cast, B	3.05	118	15.6	Agglomerates, small pores, smooth surfaces
CS-50, high density, no cast, C	3.05	103	15.3	Many variations: pores, air bubbles, smooth surfaces
CS-50, high density, Aluminum cast, A	3.08	109	15.1	Many porous zones and bubbles
CS-50 medium density, iron cast, LoTEC compliant layer	3.08	102	37.8	Very flat and smooth surface
BS-25, C no cast	2.66	53	10.23	Big agglomerates, grainy surface
BS-25, iron cast, LoTEC compliant layer	2.71	53	10.23	Grainy surface, big agglomerates
BS-25, aluminum cast, B	2.72	59	10.3	Big agglomerates, grainy surface
BS-25, B no cast	2.83	59	8.2	Big agglomerates, grainy surface
BS-25, A no cast	2.84	57	12.6	Big particles and discoloration (densities?)
BS-25, iron cast, commercial compliant layer	2.96	85.2	16.5	Big air bubbles

Table 1: Mechanical properties and typical fracture surfaces of the ceramic liners

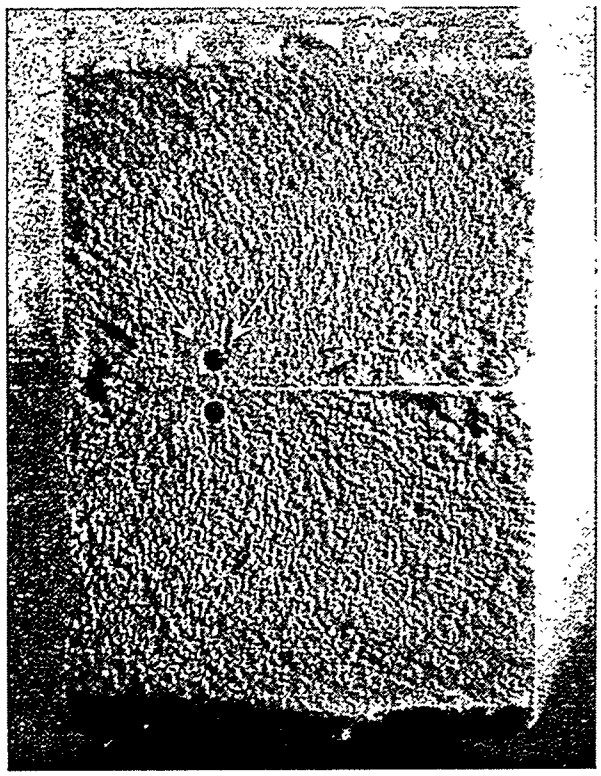

Initiation site: air bubble

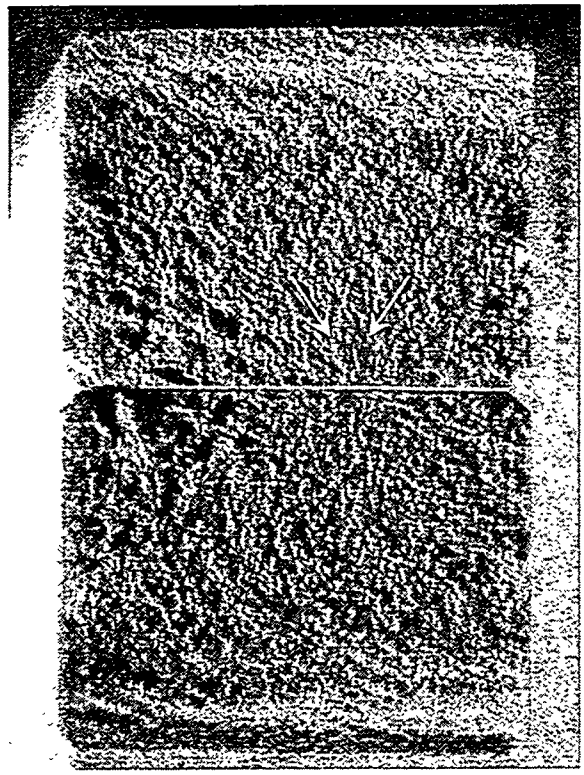

Initiation site: small agglomerate

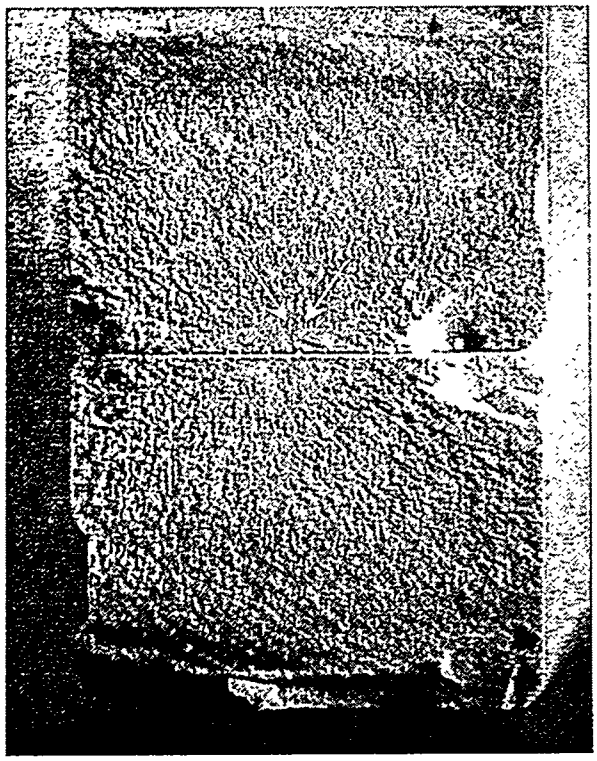

Initiation site: small air bubble

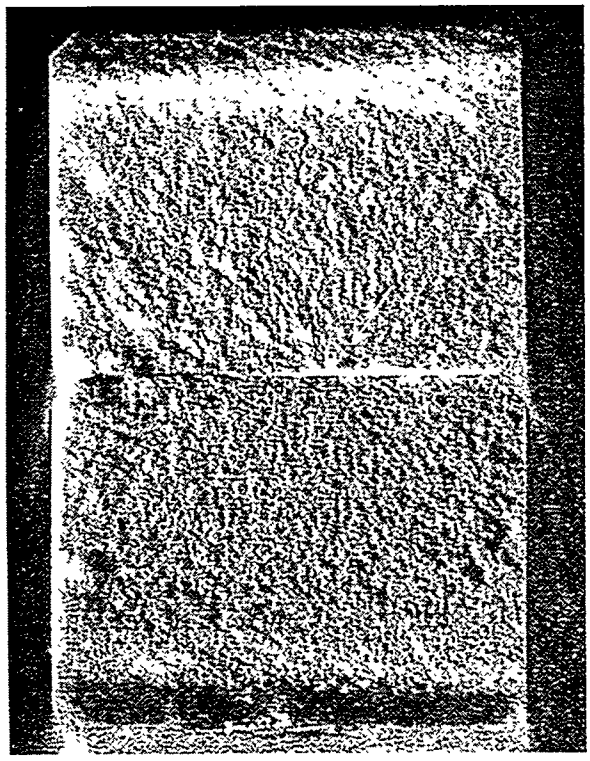

Initiation site: big agglomerate

Figure 5: Typical fracture surfaces of CS-50 samples

ADVANCED MANUFACTURING TECHNOLOGY

Durability of Diesel Engine Component Materials

Peter J. Blau, R. L. Martin, and B. C. Dumont
Oak Ridge National Laboratory

Objective/Scope

The objective of this effort is to enable the development of more durable, low-friction moving parts in diesel engines for heavy vehicle propulsion systems by conducting friction, lubrication, and wear analyses of advanced materials, surface treatments, and coatings. The scope of materials and coatings is broad and includes any metallic alloy, intermetallic compound, ceramic, or composite material which is likely to be best-suited for the given application. Parts of current interest include valves, valve guides, and scuffing-critical components, like fuel injector plungers. Hot scuffing is a primary surface damage mode of interest, although reciprocating sliding friction and wear are also of interest. Bench-scale simulations of the rubbing conditions in diesel engine environments are used to study the accumulation of surface damage, and to correlate this behavior with the properties and compositions of the surface species. The effects of mechanical, thermal, and chemical factors on scuffing and reciprocating sliding wear are being determined, and the results will be used to refine material selection strategies for durability-critical engine components.

Technical Highlights

Evaluation of Potential Valve Guide Materials Twin-bar-on-cylinder reciprocating friction and wear tests were conducted using a new ORNL-designed apparatus (see Fig. 1). The test is intended to simulate a valve stem and guide situation wherein the valve stem is canted so as to induce contact stress concentrations at both ends of the guide. Two standard modulus-of-rupture (MOR) type specimens with 3 x 4 mm cross sections are rubbed along the surface of a valve stem (i.e., the 'cylinder'). A drip feed system was incorporated into the MOR specimen holder to permit adding lubricant through fine holes between the two sliding bars.

The twin-bar-on-cylinder arrangement represented significant challenges in specimen alignment. Only a fraction of a degree of misalignment could lead to irregular wear patterns on the test specimens. Alignment characteristics of the new twin-specimen holder were evaluated under the following conditions:

stroke: 6 mm
normal force (applied on the two bars): 200 N
frequency: 10 Hz
duration: 2 h 10 min
lubrication: diesel engine oil supplied by Caterpillar Inc.

Wear volumes of the twin silicon nitride bar specimens in the early trials were not measurable with either the Rodenstock (Munich, Germany) non-contact laser system or the stylus profiling system (rank Talyor Hobson, Leicester, UK). Three measurements (2-D) were done on each scar using the stylus method. For the non-contact method, four line profiles were extracted from the laser scan of each scar to calculate the cross-sectional worn area. Wear measurements using the two techniques were compared and found

to agree well (Table 1). One scar had about twice the area of the other. The average areas differed between measurement methods by about 9% on scar 1 and 5% on scar 2.

Table 1. Comparison of Wear Using Two Measurement Methods

Scar number	Method	Number of profiles	Average cross-sectional area (μm^2)	Standard deviation in cross-sectional area (μm^2)
1	laser	3	37840.	1450.
	stylus	4	34800.	4000.
2	laser	3	19780.	6800.
	stylus	4	18840.	6880.

From this work on establishing the test methodology, we concluded that:

(1) Alignment problems are improved over a single bar-on-cylinder with the new, twin-bar holder design, but it still requires careful attention during set-up.

(2) Laser and stylus methods of determining wear volumes on the valve stems provide reasonably good agreement, with the stylus method giving slightly lower numbers.

Four different materials combinations and two different lubricating oils were then evaluated using the twin-bar-on-cylinder test. MOR specimen materials were:

1. SN1 (a Japanese grade of silicon nitride)
2. a silicon nitride-based composite (SN, 8%Y, 4% Al_2O_3, 10% SiC, 30% TiC)
3. NT-451
4. NT-551

The first material was obtained from K. Breder, ORNL; the next from G. Crosbie, Ford Motor Company, Dearborn, MI; and the last two from R. Licht, Norton Company, Northboro, MA. The Ford material was formulated to have a thermal expansion coefficient offering good compatibility with engine materials. It also offered the potential to combine some of the attractive wear characteristics of SiC/Si_3N_4 composites reported by Yust and DeVore based on earlier work at ORNL[1].

The ceramic specimens were worn against sections cut from Cr-plated steel diesel engine valves. Two oils were used. M. Long, Caterpillar Tech Center, provided one of the oils, a typical grade of diesel engine oil. The second oil provided by R. Spence, Lubricant Additives Research, Cleveland, Ohio, this specially-compounded lubricant contains Ag additives, and its viscosity is around 10.3 cSt at 100C (grade 15W30). Silver is suspended in the form of angstrom-sized particles which are intended to become activated and form lubricating films during contact. The lubricants were compared to determine whether the Ag would offer any advantages for lubricating ceramics than would the conventional diesel oil.

The conditions used for the tests were:

- Stroke: 8 mm
- Normal force (distributed on both bars): 200 N
- Duration: 4h20m30s
- Sliding distance: 2.5 km
- Lubrication: diesel engine oil and oil containing Ag
- Temperature: ambient

Replicate tests were run for each material pairing in each type of oil. Irrespective of the type of MOR specimen material, the friction coefficient usually started relatively high then decreased. However, in the oil with no Ag, the composite ceramic (30% TiC) against steel exhibited the highest value in the beginning of the test. After a sliding distance of 2.5 km, the friction coefficient of the couple 30% TiC/steel remained higher ($\mu = 0.16$) than for the other couples ($\mu = 0.10$ - 0.12). Under lubrication with the oil containing Ag, same behavior was observed, but at the end of the test each slider material had a lower friction coefficient: SN1 ($\mu = 0.11$), NT-451 ($\mu = 0.13$), NT-551 (($\mu = 0.16$), and 30% TiC ($\mu = 0.19$).

No measurable wear was obtained on the MOR specimens. However, the Cr-plated stems wore more against 30% TiC than against the other ceramics, irrespective of lubricant. Wear on the valve stem was greater in the oil containing Ag than in the Caterpillar diesel oil. If we compare the results for NT-451 and for NT-551, rubbing against the latter induced more wear in the stem section than against the former.

In order to evaluate the relative wear rates of the ceramics, plans were made to conduct more severe sliding tests using a reciprocating ball-on-flat geometry. Type 316 stainless steel, being similar in hardness to the Cr-plated valve stems, and possessing similar chromium oxide on the surface, was chosen as the ball material. Results will be reported later.

Scuffing Literature Survey Being Compiled. A detailed, annotated bibliography on the mechanisms of scuffing is being compiled. This information will be used to develop a new, high-temperature scuffing system at ORNL for testing candidate materials for scuffing-critical components of diesel engines. Cummins Engine Company has provided data relevant to scuffing, and will work closely with us in developing scuffing test methods that offer advantages over the currently-available testing methods.

Reference:

[1] C. S. Yust and C. E. DeVore, "The Friction and Wear of Lubricated Si_3N_4/SiC(w) Composites," *Tribology Transactions*, Vol. 34 (4), 497-504.

Future Plans

a) A new series of friction and wear tests will be performed using the reciprocating ball-on-flat geometry. The ball material will be stainless steel 316 and the flat specimens will be NT-451 and the 30% TiC composite material prepared by Ford Motor Company. Diesel oil and Ag-containing oil will be used in these tests.

b) A compilation of an annotated bibliography on the mechanisms of scuffing will be completed.

Status of Milestones

On schedule

Communications/Visitors/Travel

None

Problems Encountered

Intermittent testing machine motor problems were encountered. After a motor and speed controller diagnosis by the ORNL electricians, the electrical problem has been rectified.

Publications and Presentations

None

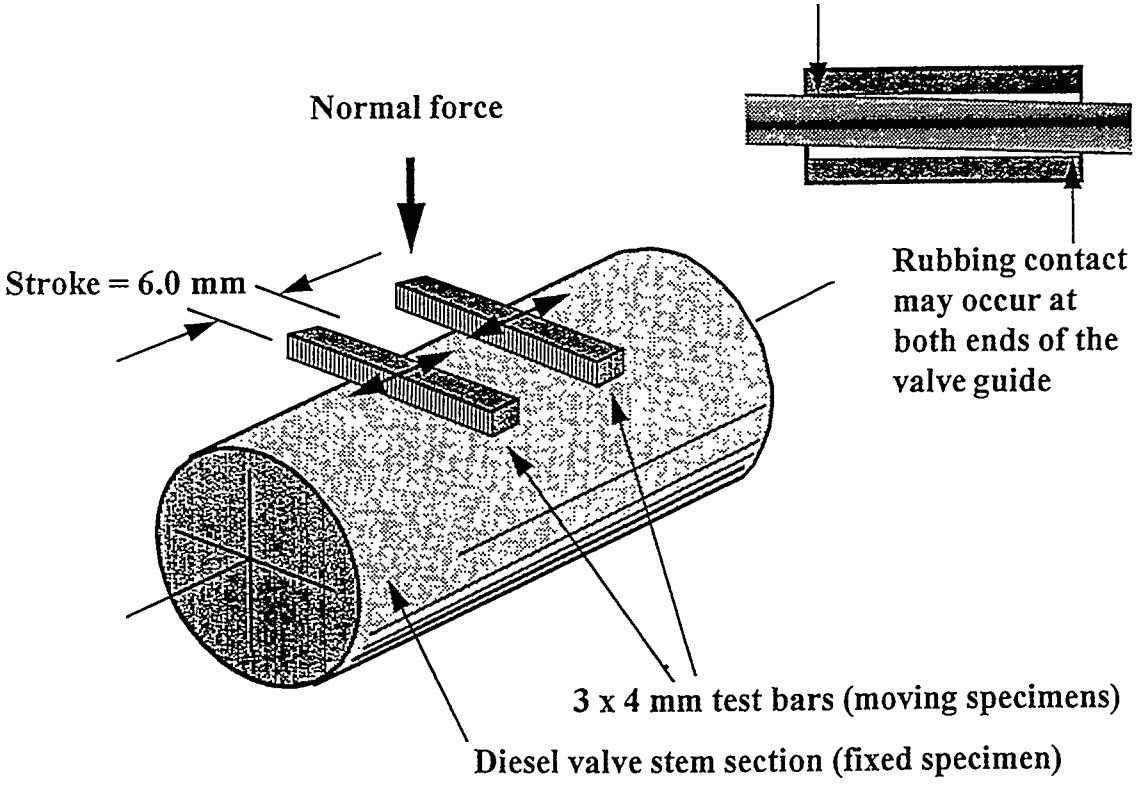

Fig. 1. Diagram of the twin bar-on-cylinder apparatus. Tilting of a value stem, as indicated at the upper right, may cause contact stresses to be locally larger at the ends of the valve guide than would occur if the stem were centered in the bore. Thus, the two concentrated contacts in the twin bar test bear a closer resemblance to the actual situation than might initially be supposed.

Development of an "Intelligent Grinding Wheel" for In-Process Monitoring of Ceramic Grinding

S. Malkin, R. Gao, C. Guo, B. Varghese and S. Pathare
Department of Mechanical and Industrial Engineering
University of Massachusetts
Amherst, MA 01003-2210

U. S. Department of Energy
Identification Number : DE-FG05-96OR22524

Introduction

This is the fourth semi-annual report for the project "Development of an Intelligent Grinding Wheel for In-Process Monitoring of Ceramic Grinding." This report covers the period from March 1, 1998 to August 31, 1998.

The overall objective of this project is to develop sensor-integrated "intelligent" diamond wheels for grinding of ceramics. Such wheels will be "smart" enough to monitor and supervise both the wheel preparation and grinding processes without the need to instrument the machine tool. Intelligent wheels will utilize re-useable cores integrated with sensors: to measure the acoustic emission (AE) and grinding force. Signals from the sensors will be transmitted from a rotating wheel to a receiver by telemetry. Wheels will be "trained" to recognize distinct characteristics associated with truing, dressing and grinding.

Technical Progress

This overall project is divided into six tasks as follows:

1. Development of miniaturized sensors and data transmission system,
2. Wheel design and sensor configuration,
3. Calibration of the sensor integrated wheel,
4. Training of the intelligent wheel,
5. Grinding tests,
6. Prototype demonstration.

The technical progress is summarized in this report according to the tasks. All activity during this period has been concerned with the first two interrelated tasks, which need to be completed before undertaking the remaining tasks.

Task 1. Development of Miniaturized Data Transmission Electronics

As mentioned in the third Semi-Annual report, the grinding wheel has a total of fifteen embedded sensors. Eleven of them are configured as force sensors and located around the periphery of the grinding wheel. The remaining four are acoustic emission sensors and placed on the face and towards the center of the grinding wheel. Design considerations for sensor selection and their placement strategy were described in the previous report.

The development of data acquisition and transmission electronics has been conducted in three consecutive stages:

1) Bread-board level design and implementation of various functional modules of the entire circuitry,
2) Integration of various functional modules on a PCB for interfacing and combined circuit operation verification, and
3) Design, simulation, and fabrication of a miniaturized circuit board using surface-mount devices (SMD).

For the previous reporting period, research was focused on stage three where the surface mount technique was explored for circuit miniaturization. Results from the first and second stage development provided valuable inputs to fine tune the final design. In

addition to meeting the circuit functionality requirement, the design also has taken into account the space limitation determined by the targeted grinding wheel.

Figure 1.1 shows a block diagram of the final miniaturized circuit. The circuit was implemented as a six-layered PCB board (Printed Circuit Board) which has been fabricated by a commercial vendor. A photograph of the fabricated PCB is shown in Figure 1.2, with components soldered on both sides. Of the six layers, four have been used as signal routing layers and two for the power supply rails (V_{cc} and Ground). The use of four routing layers significantly reduces the length of connection tracks between individual components. The two dedicated layers for power supply rails are essential for providing a ripple-free voltage supply to the circuitry. Furthermore, they provide good shielding for the entire circuitry against ambient electrical noise. This is especially important considering the high frequency range in which the circuits will operate.

1.1 Description of the Circuitry:

As shown in Figure 1.1, there are three main functional modules within the circuitry:

1) An analog front-end which provides interface to the fifteen sensors and contains an Analog-to-Digital Converter,
2) A digital signal processing module centered around a 16-bit DSP, and
3) An RF transmitter for wireless data transmission.

In order to prevent interference and cross talk, inductors have been used to separate AC links between the analog and digital circuitry. This is necessary to prevent high frequency noise generated by a fast switching digital circuit from corrupting the analog signals.

There are three components in the circuit which need a clock signal: the Analog-to-Digital Converter (ADC), Digital Signal Processor (DSP), and the RF interface circuit. In order to minimize the size of the entire circuitry, a single clock chip operating at 1.84 MHz was used. Therefore, the ADC is operated at a frequency slightly lower than its nominal value of 3 MHz. An internal Phase Locked Loop (PLL) within the DSP is used to step up the clock frequency by fifteen times to 27.6 MHz, such that the DSP can be operated at its full speed. The RF interface circuit divides the input clock of 1.84 MHz and transmits data at 4800 bits per second.

The anti-aliasing filter used in the miniaturized version of the circuit is a simple RC filter. Earlier versions of the circuit utilized a four-pole active filter. Preliminary tests revealed that this type of filter introduced distortion to input signals of more than 0.8 V p-p amplitude, which considerably limited the dynamic operating range of the charge amplifier.

1.2 Verification of the Circuit Board:

The fabricated circuit boards were visually and functionally tested for bad or wrong electrical connections. In the next step, SMD components were hand-soldered on to the board under a specially designed magnifier. A digital signal processor emulator was used for programming the DSP. The program further verified various functional blocks of the

circuit including the attenuator selector, sensor selector, ADC, RF transmitter interface, and RF transmission.

Several software driver modules have been developed using the "C" language to access the DSP peripherals. Further development of signal processing algorithms is currently under way.

Task 2. Wheel Design & Manufacture

The design of the sensor integrated grinding wheel was described in detail in the Third Semi-Annual Report. This section describes the design of the adapter disk which houses the on-board electronics and the manufacture of the sensor-integrated grinding wheel.

2.1 Design of the Adapter Disk

As described in the previous report, an adapter disk is used to house the electronic circuitry. The adapter disk is fastened to the wheel core during grinding for the purpose of monitoring the process in real-time. This design minimizes the need for structural alterations to the wheel core and facilitates easy access to the electronics.

The layout of the adapter disk together with the on-board electronics is shown in Figure 2.1. A set of fifteen connectors is mounted on the periphery of the adapter disk. Each sensor is electrically connected to the "on-board" electronics by means of these connectors. The electronics is physically separated into three segments: data acquisition system, radio frequency (RF) transmitter, and power supply. The data acquisition system

consists of a signal multiplexer, charge amplifier, anti-aliasing filter, analog to digital converter, and digital signal processor (DSP). Wires laid out in the annular recess of the adapter disk provide connections to the RF transmitter and the power. The electronic circuitry, together with the power supply, are anchored to the adapter plates by means of screws. An aluminum cover on the outer face of the adapter disk provides EMI shielding.

2.2 Manufacture of the Sensor Integrated Grinding Wheel

The wheel core is designed with 11 equally spaced slots around its periphery which hold the piezoceramic sensors. Prior to being mounted in the wheel, responses of the individual sensors were measured by subjecting each of them to a fluctuating load of 5 ± 2 lbs applied by a universal testing machine (Instron) at a frequency of 5 Hz. The results are summarized in Figure 2.2. Clearly there are some variations in the individual responses of these sensors, which is taken into account during electronic calibration of the wheel.

After testing, brass strips were attached to the positive face of each sensor (the negative face has a distinguishing "black dot"). The negative face of each sensor was then attached to the periphery of the wheel core in its slot as shown in Figure 2.3. Each sensor was fixed in place by means of a two-component epoxy adhesive (EPOTECH) and cured for two hours at 60° C. The brass strip was soldered to the connection pads. The connection pads together with the wheel core form the positive and negative terminals of the sensor. The entire machined slot was filled with epoxy adhesive to ensure adequate abrasive-sensor contact and to provide sensor protection (physical & thermal) during wheel manufacture and operation.

The wheel core with the sensors mounted was machined on the outer periphery to form a clean surface for bonding the abrasive. Diamond abrasives segments were attached to the sensor integrated core at the Norton Company. Two sensor integrated grinding wheels were manufactured in this manner. One of these wheels is shown in Figure 2.4.

Task 3 Testing & Calibration

This section describes the procedure and results obtained while testing the individual components of the grinding wheel monitoring system.

3.1 Wheel Balance & Spin Test

The two sensor-integrated grinding wheels were statically balanced and spin tested at Norton Company in Worcester, Massachusetts. For this purpose, each sensor-integrated grinding wheel together with the mounting flanges was placed on a static balancing device. Both wheels were statically balanced by removing excess material from the wheel core. The balanced wheels were then spin tested at peripheral speeds up to 90 m/s to ensure safe operation during grinding. The wheels were qualified by Norton Company to operate at a maximum surface speed of 60 m/s (3275 rpm , 14 inch diameter wheel).

After the manufacture of all sub-systems is completed, the wheel along with the adapter disk and the miniaturized electronics will be dynamically balanced at Norton Company.

3.2 Response of the Sensor Integrated Wheel

A set of experiments was conducted to determine the response of the sensor-integrated wheel. Using an Instron universal testing machine, a precise cyclic radial load of 5 ± 2 lbs was applied to the wheel periphery at five locations 2 degrees apart in the vicinity of each sensor. The sensors were connected to a data acquisition system to acquire data in real-time.

Figure 3.1 shows the response of each sensor to the dynamic load. It is clear that there is some variation among the individual sensor responses. These variations can be attributed to such factors as the inherent sensor variability, voids in the epoxy adhesive, and variation in angular location of the loading member. Furthermore, it can be seen the sensor response is only about 10% of that observed for the individual sensors, which was expected. This is due to the added stiffness of the abrasive and epoxy layer placed above the sensor. The variation in sensor response will be taken in account during electronic calibration of the wheel prior to actual grinding.

3.3 Testing a Model System

In order to facilitate the development and implementation of data conditioning/processing routines and telemetry, a test system was fabricated. The test system consisted of a sensor embedded wheel, bread board level data acquisition and digital signal processor circuitry, and an RF transmitter/receiver. Data processing software with a graphical user interface was developed for data reception, processing, grinding feature extraction, and presentation. The digital signal processor (DSP) was programmed to acquire data when

the wheel was excited by an impulse and to transmit the acquired data to an external receiver. This task was successfully accomplished and demonstrated.

The system was also used to test the reliability of data transfer by telemetry in the vicinity of the machine and in the presence of grinding sparks. The test system was placed approximately 6 feet from the grinding machine, while the receiver was positioned very close (within 3 inches) of the grinding zone. The DSP was programmed to transmit a pre-defined signal during grinding. The transmitted data was acquired by means of the RF receiver and displayed on an external computer. Figure 3.2 shows the results of this test. Although there is some noise in the data, the presence of grinding sparks does not appear to significantly affect the data transfer. It should be noted that the data was transmitted without any error checking/correcting code. Errors in data transmission can be minimized by implementing a simple error checking code, reducing the transmission distance, and re-transmission of data.

Publications

- S. Pathare, R. Gao, B. Varghese, C. Guo, and S. Malkin, "A DSP-based telemetric data acquisition system for in-process monitoring of grinding operation", *Proc. IEEE Instrumentation and Measurement Technology Conference (IMTC/98)*, pp. 191-196, St. Paul, MN, May 18-21, 1998.

Trips and Meetings

Robert Gao attended the 1998 IEEE Instrumentation and Measurement Technology Conference (IMTC/98) at St. Paul, Minnesota in May 1998 and presented a paper on DSP-based telemetric data acquisition system development for the current project (see Publications). In June 1998, he also attended a workshop on the frontiers of microfabrication sponsored by the Beckman Institute at the University of Illinois at Urbana-Champaign. This material covered in this workshop is directly applicable to the intelligent grinding wheel project.

Changsheng Guo, Biju Varghese and Sumukh Pathare visited Norton Company in April 1998 to discuss ways to bond the abrasive segments on to the wheel core. Biju Varghese visited Norton Company again in May in order to conduct static balance and spin testing on the sensor integrated grinding wheel.

Biju Varghese was selected to attend a workshop on "Team Building Skills" at the University of Michigan, Ann Arbor on June 15 and 16. The purpose of this workshop was to develop skills necessary for effective participation in interdisciplinary teams, such as the grinding wheel project. The registration fee and travel expenses for his participation in this workshop were covered by the University of Michigan.

Personnel

- Stephen Malkin, Sc.D., Distinguished Professor, Principal Investigator

  Overall project management, grinding test and analysis.

- Robert Gao, Ph.D., Assistant Professor, Co-Principal Investigator

  Design of miniaturized sensors, telemetry, and microelectronics; testing, and prototype demonstration.

- Changsheng Guo, Ph.D., Senior Research Fellow, Co-Principal Investigator

  Mechanical design, setup, testing and prototyping of grinding wheel.

- Biju Varghese, Graduate Research Assistant, Ph.D. Student

  Mechanical design, calibration, training and testing of the grinding wheel prototype

- Sumukh Pathare, Graduate Research Assistant, M.S. Student

  Sensor development, electronic circuits design, implementation, and testing

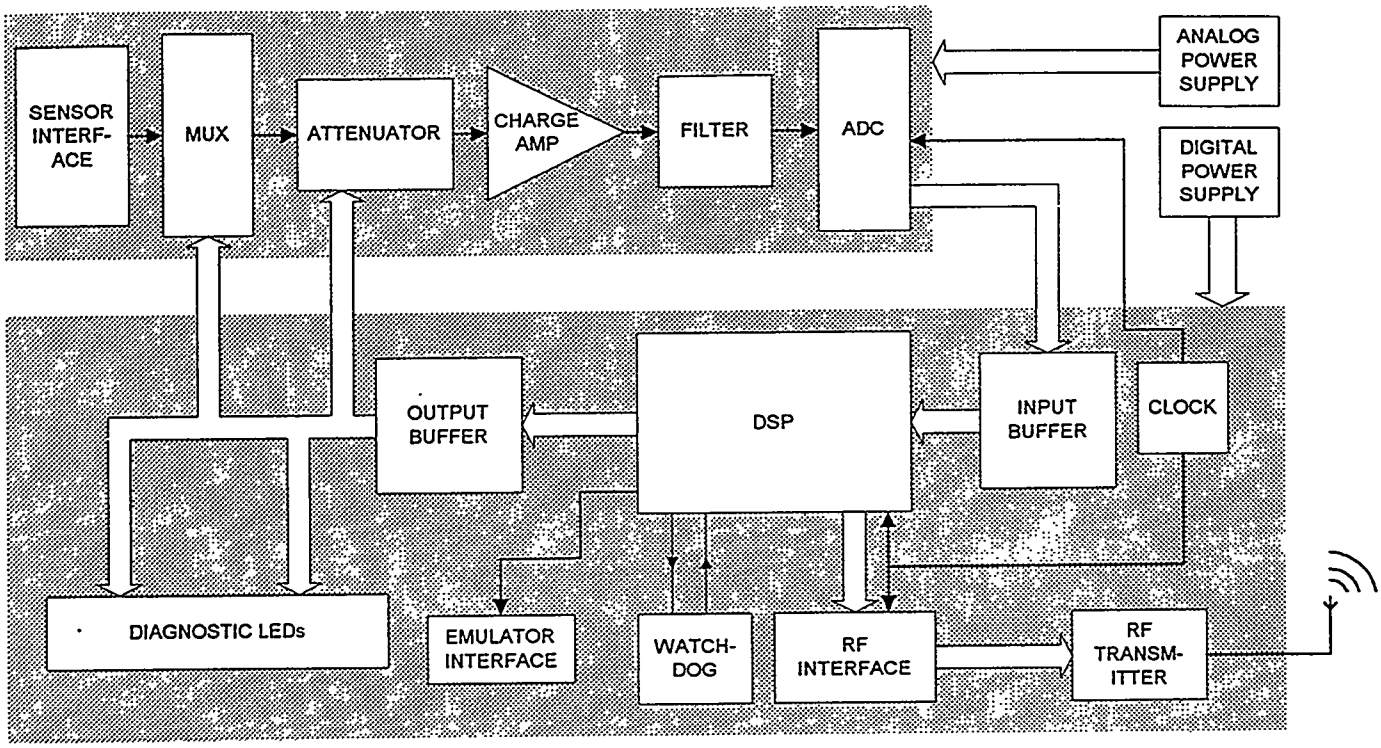

Figure 1.1 Block diagram of the miniaturized circuit

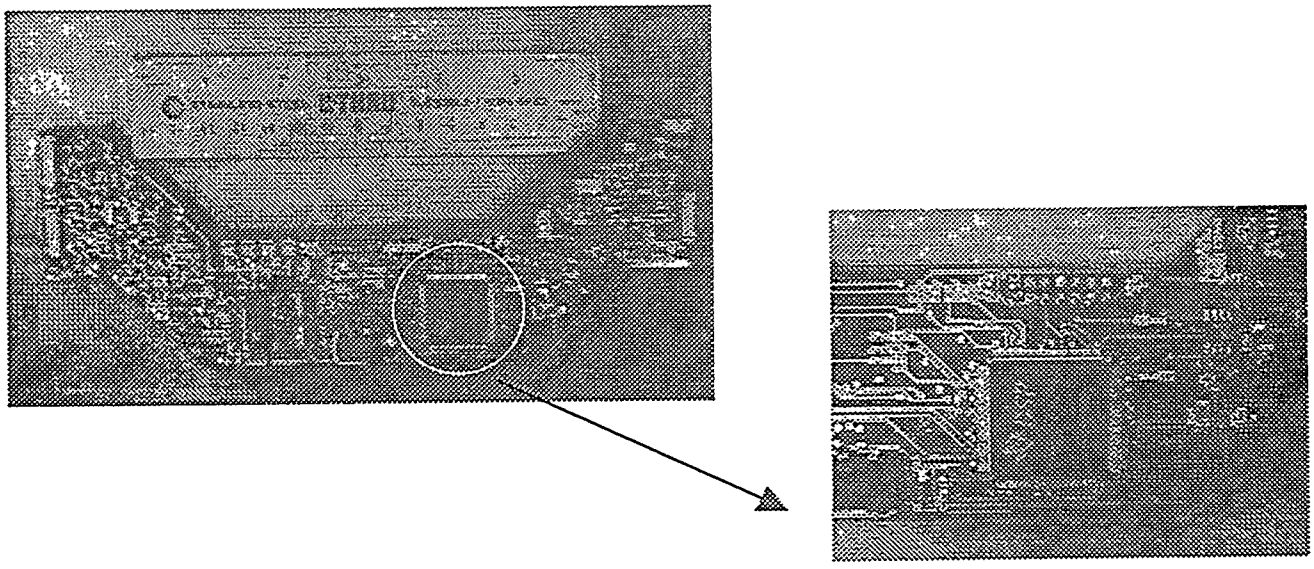

Figure 1.2 Photograph of the fabricated circuit

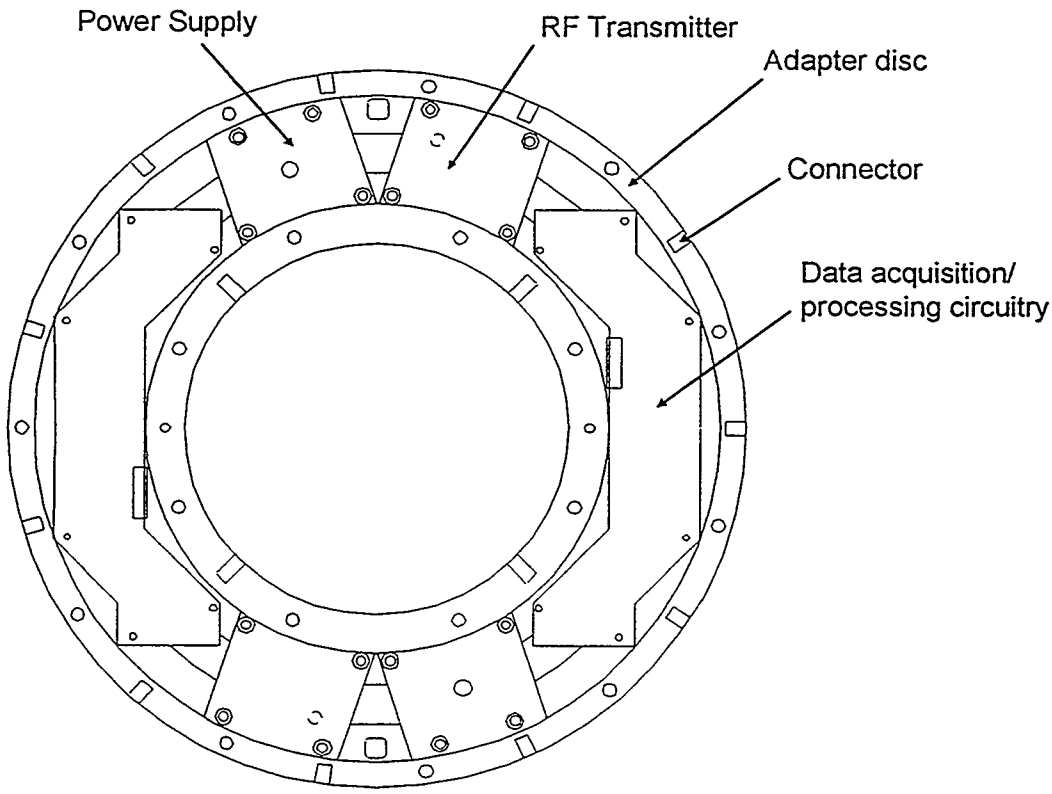

Figure 2.1 Adapter disk assembly

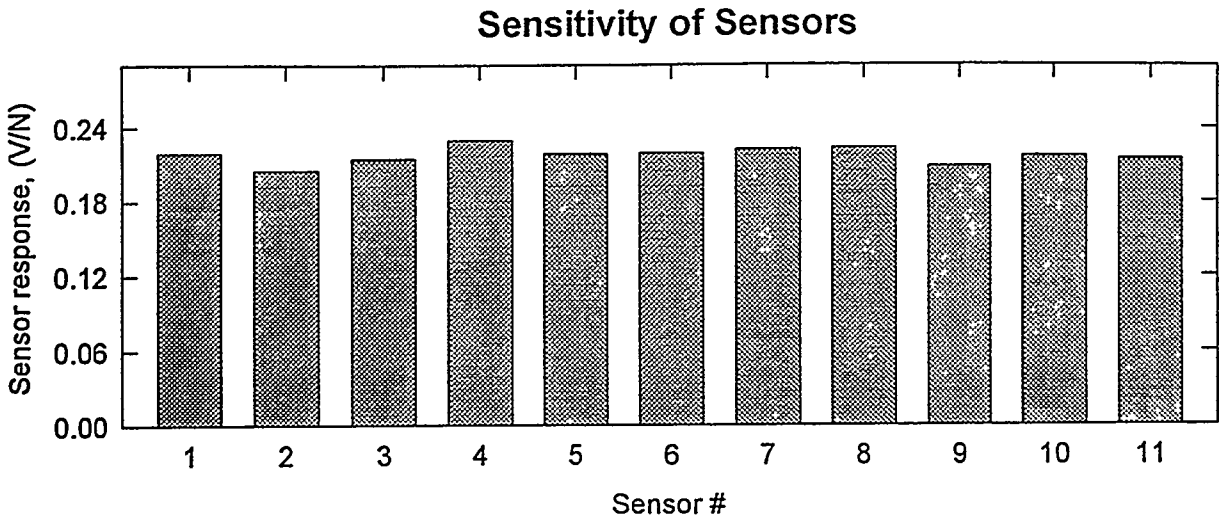

Figure 2.2 Response of individual sensors prior to their integration into the wheel core

(load : 5 ± 2 lbs at 5 Hz)

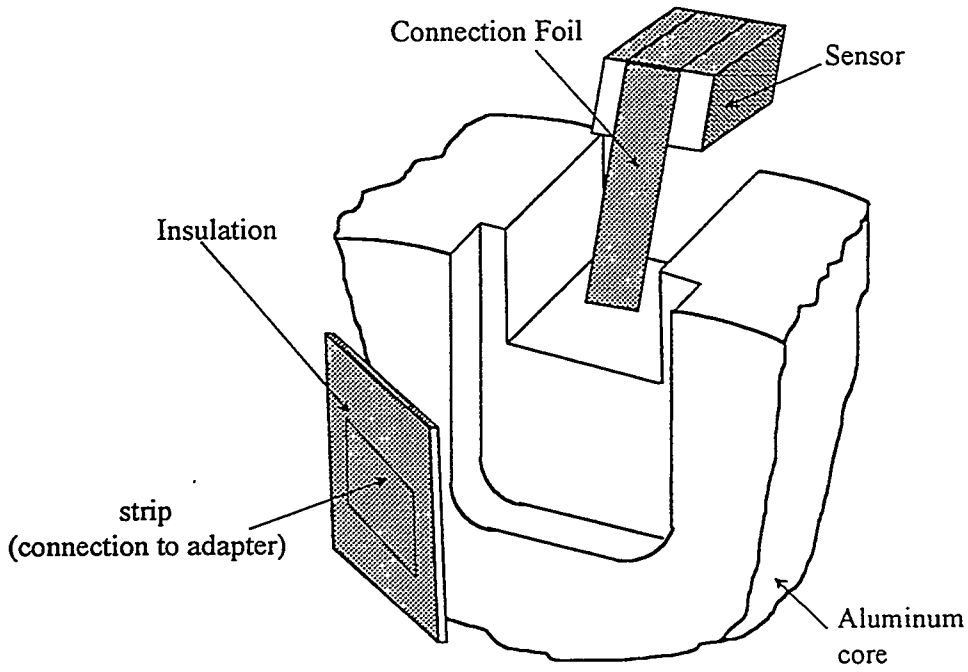

Figure 2.3 Arrangement for mounting sensors in slots around wheel core periphery.

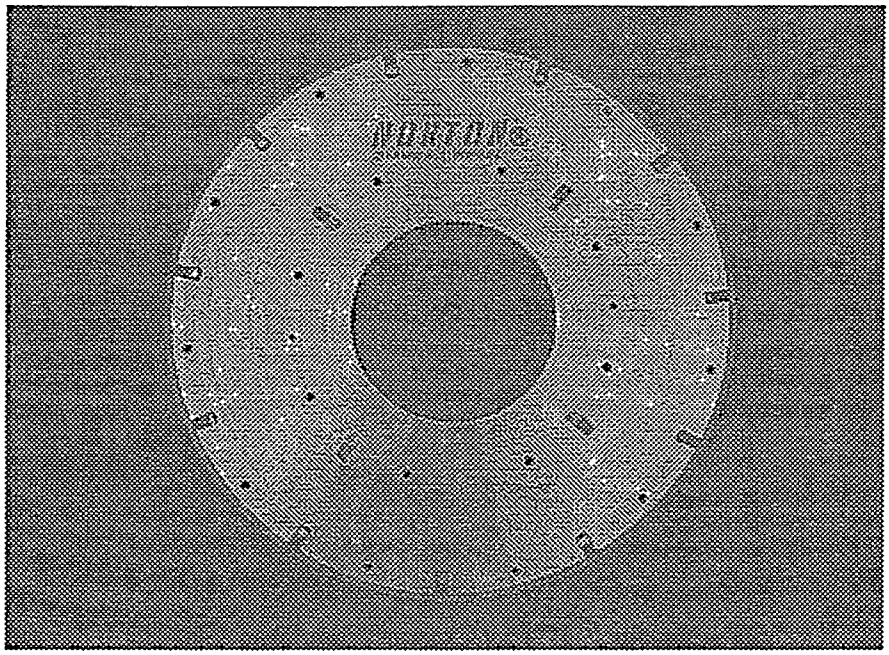

Figure 2.4 Photograph of grinding wheel

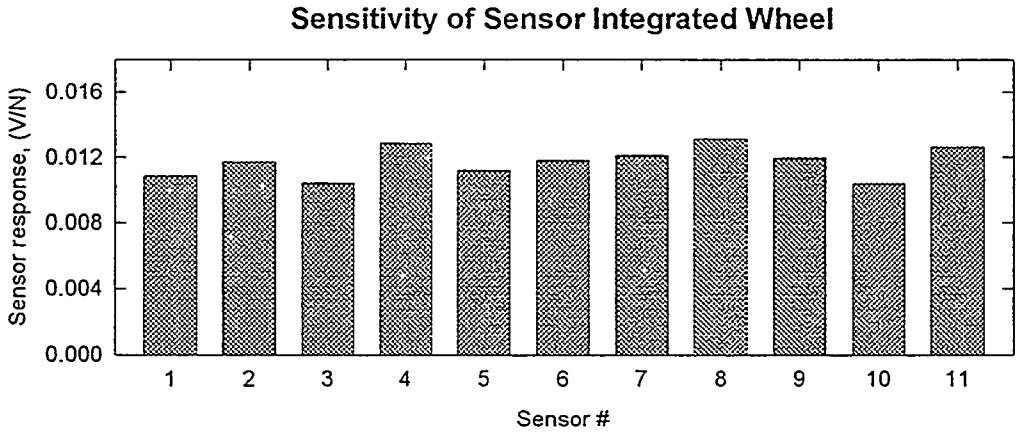

Figure 3.1 Response of sensor-integrated wheel
(load : 5 ± 2 lbs at 5 Hz)

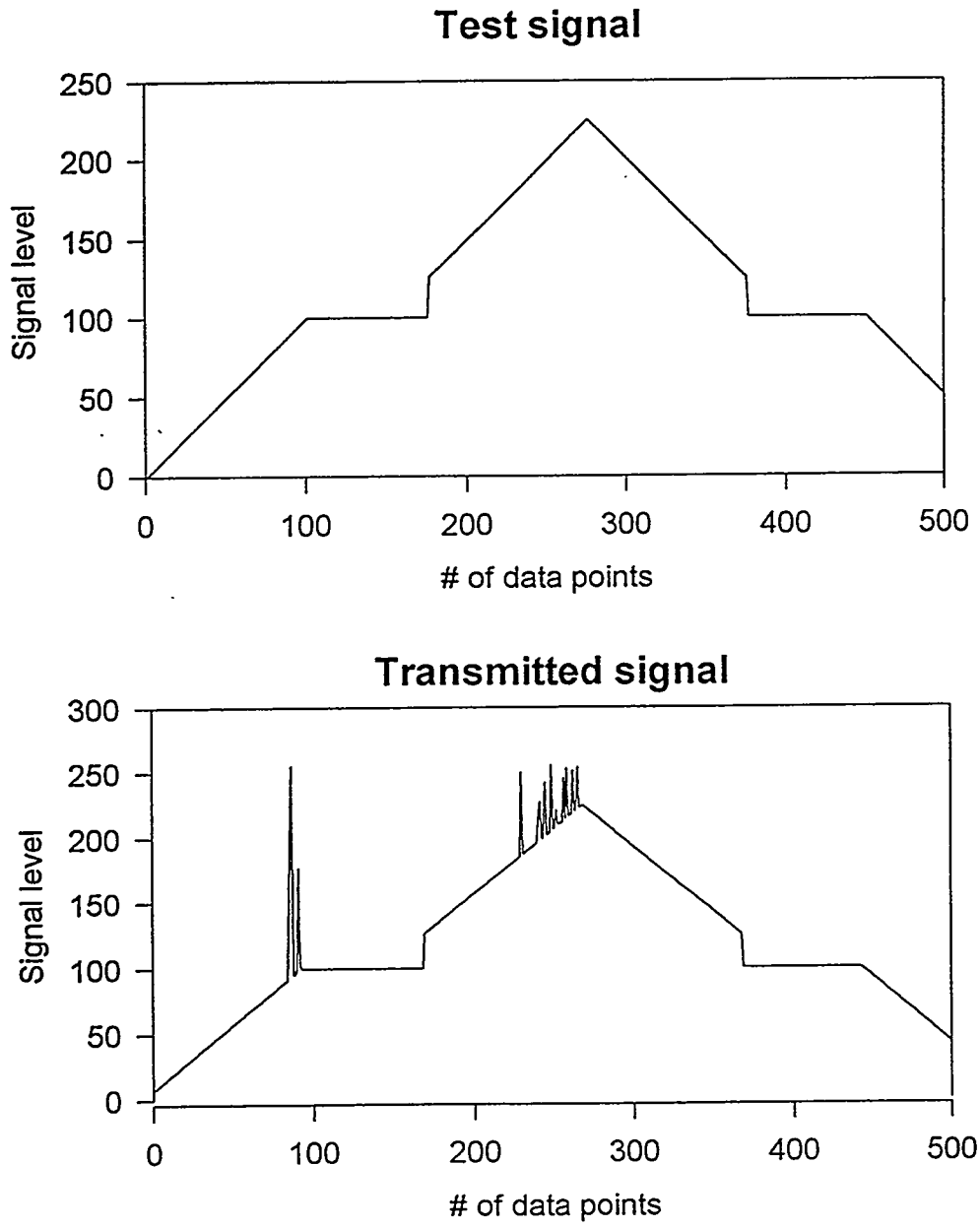

Figure 3.2 Results of telemetric data transfer test in the vicinity of the grinding process

Laser Scatter Methods for Detecting Subsurface Machining Damage in Ceramics – Jiangang Sun, William A. Ellingson, (Argonne National Laboratory), Michael C. Long, Michael H. Haselkorn, and Charles J. Anderson (Caterpillar Inc.)

Objective/scope

The primary objective of this program is to develop a laser-based elastic optical scattering procedure which would provide a direct (near real-time) method to detect machining induced damage in monolithic ceramics. Median and lateral crack detection are of primary importance. The laser-based elastic optical scattering program is being executed in three steps. The first step is to optimize the elastic scattering procedure by examining specimens machined using innovative machining techniques. The second step involves correlation of the elastic scattering results with mechanical properties in "real" machined ceramic specimens. The final step involves the development of a prototype instrument to be evaluated for on-line implementation in a production environment.

Technical progress

1. Elastic Optical Scattering Results

1.A Caterpillar Samples

We continued the effort to establish correlations between the elastic optical scattering data and the surface microstructure and machining damage, using the diamond-ground GS44 specimen CAT8B which has a high material removal rate. Our technique is to sequentially do the following steps: a) obtain laser scatter data, b) obtain optical photomicrographs, c) polish to remove a layer of material and repeat the sequence.

The ground surface of the specimen CAT8B has been polished and examined at several depths. Figure 1 shows a photomicrograph of the specimen surface after a 21-μm layer has been polished off. It is seen that there are four deeper grinding groves where machining damage would be severe. The region enclosed in a black frame has been studied at various polishing depths. Figures 2a-c show the photomicrographs of this surface region at depths 21, 38, and 51 μm below the ground surface. Figures 3 and 4 show elastic optical scattering ratio and sum images (at 5-μm resolution) of the surface region after the original ground surface was polished by 38- and 51-μm layers, respectively. Several prominent features (flaws) are indicated in the figures. The features identified as "cracks" and "spot" are material defects, while that identified as "line" is presumably due to machining damage. The micrographs (at 1000X) in Figs. 5 and 6 show that the "spot" region contains a subsurface void and the "line" region is associated with high porosity in the subsurface. In the scatter images, the surface-breaking "cracks" and the porous "spot" are clearly detected. The machining "line" is detected after the polishing of a 38-μm layer, Fig. 3; but it is not detected after the polishing of a 51-μm layer, Fig. 4. This observation indicates that the machining

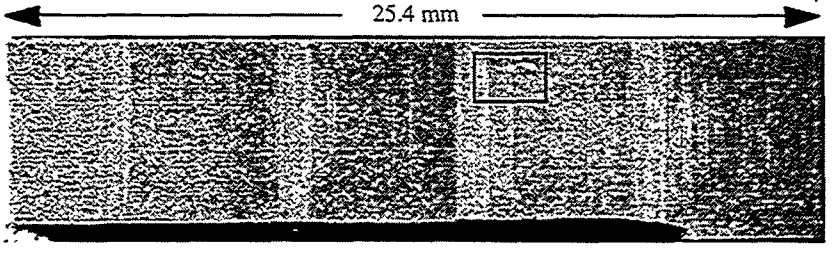

Figure 1 Photo micrograph of the surface of the GS44 specimen CAT8B, after a 21-μm layer has been polished off from the ground surface.

damage is not very deep. In addition, the laser scatter method detected subsurface porous regions shown in Figs. 3 and 4 as white spots in the sum images and corresponding darker spots in the ratio images.

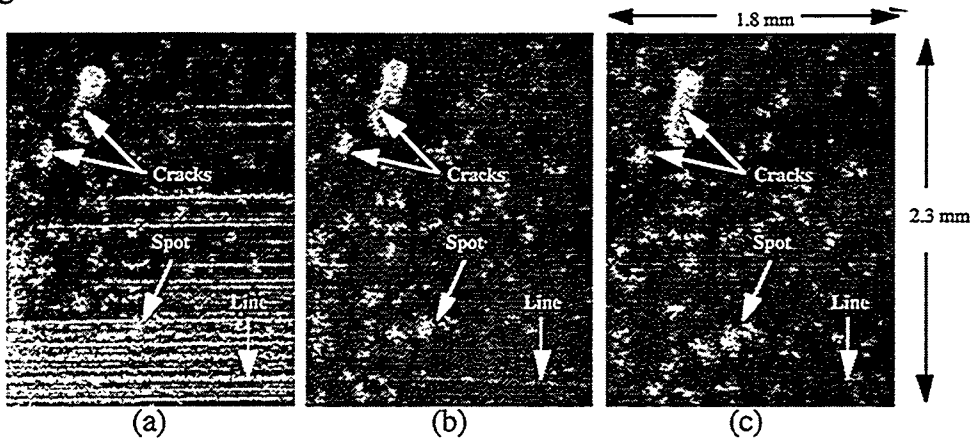

Figure 2 Photo micrographs (50X) at (a) 21, (b) 38, and (c) 51 μm below the ground surface region enclosed in the black frame shown in Fig. 1.

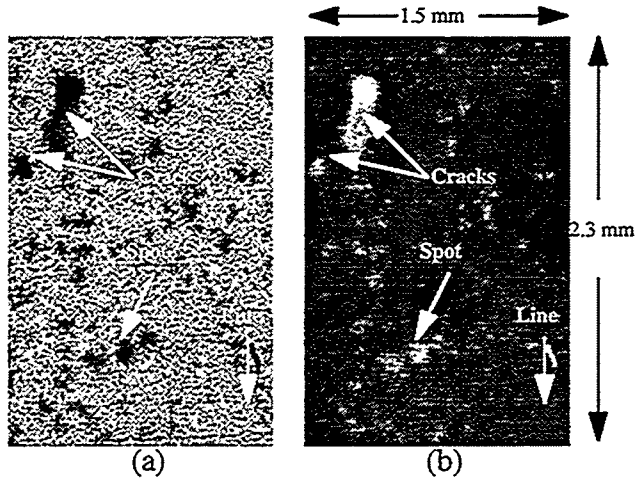

Figure 3 Elastic optical scatter (a) ratio and (b) sum images of diamond-ground GS44 specimen CAT8B, after polishing off a layer of 38 μm from the ground surface.

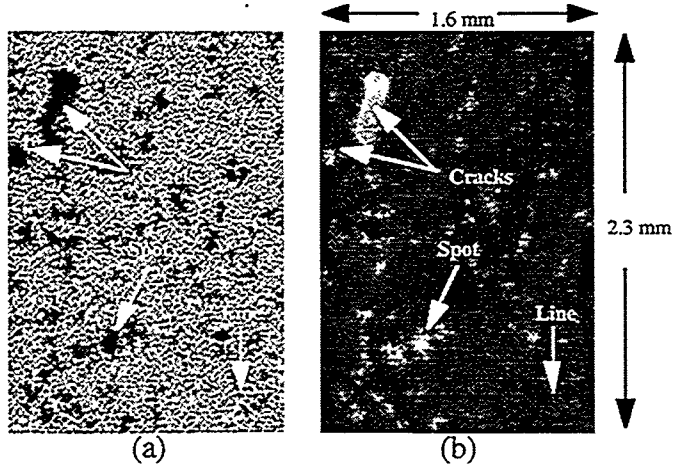

Figure 4 Elastic optical scatter (a) ratio and (b) sum images of diamond-ground GS44 specimen CAT8B, after polishing off a layer of 51 μm from the ground surface.

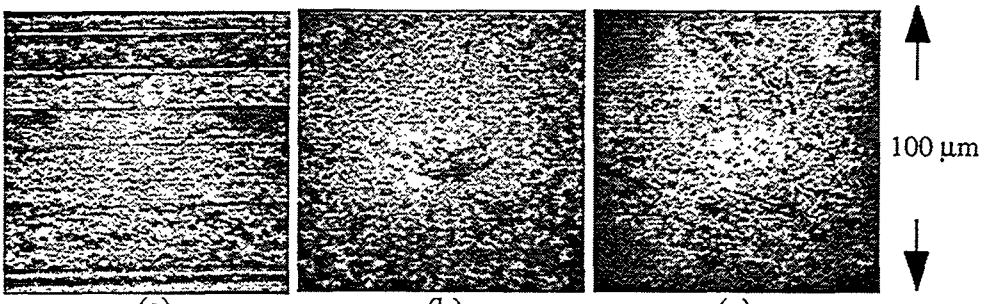

Figure 5 Surface photo micrographs (1000X)) of the "spot" region of the diamond-ground GS44 specimen CAT8B shown in Fig. 2, (a) original ground surface, and after removing (b) a 38-μm and (c) a 51-μm layer by polishing.

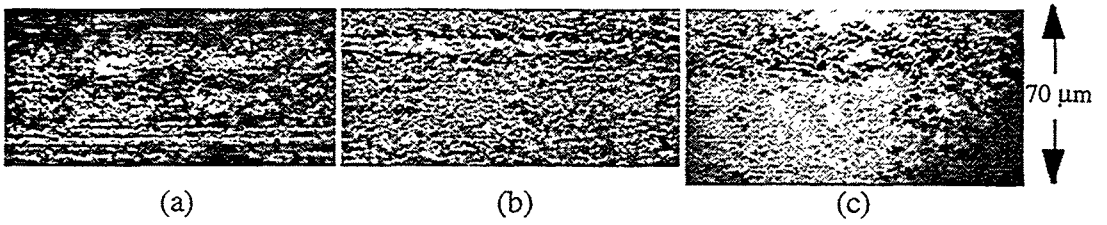

Figure 6 Surface photo micrographs (1000X)) of the "line" region of the diamond-ground GS44 specimen CAT8B shown in Fig. 2, (a) original ground surface, and after removing (b) a 38-μm and (c) a 51-μm layer by polishing.

Figure 7 shows laser scattering ratio and sum images at 5-μm resolution on a 0.5-mm x 0.5-mm surface region of the polished GS44 specimen CAT8B. Two darker spots in the sum image are marked, which are not detected in the ratio image. By examining the surface photo micrographs of this region, shown in Fig. 8, it is seen that there is no apparent damage in this region while there is optical property change (low scattering) in the regions of the two spots. Therefore, we may tentatively conclude that the two darker spots in the sum image represent subsurface material contamination (or inclusion).

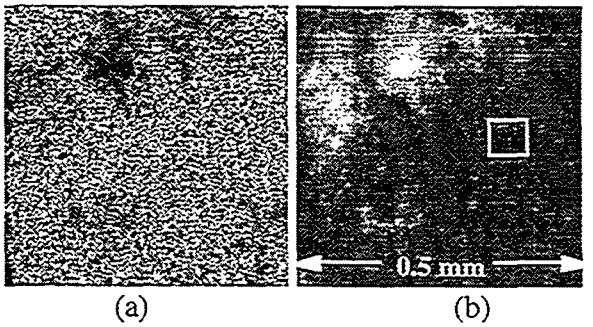

Figure 7 Elastic optical scatter (a) ratio and (b) sum images of the ground surface of the diamond-ground GS44 specimen CAT8B.

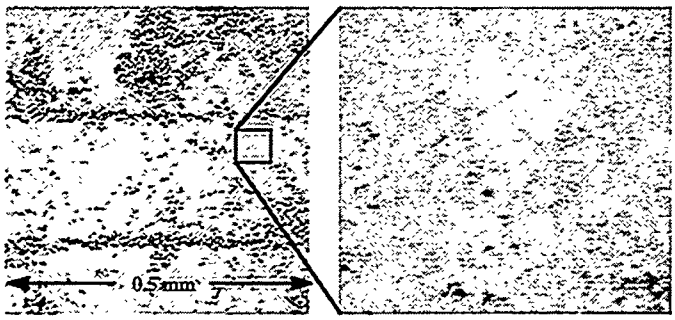

Figure 8 Photo micrographs at (a) 50X and (b) 1000X on the surface region of the diamond-ground GS44 specimen CAT8B shown in Fig. 6.

A set of 7 ground RBSN specimens were received from Caterpillar during this period, and their machining condition (power consumed during machining) is listed in Table 1. Figure 9 shows optical scatter sum and ratio images of specimens No. 5 (6.0HP), No. 2 (7.5HP), and No. 7 (8.6HP) scanned in surface areas of 1 cm x 1 cm with a coarse resolution of 20 μm. It is seen that there are considerable white spots in the sum images and corresponding black spots in the ratio images, and their number increases with the increase of the machining power. Therefore, these spots in the scatter images may be the results of machining damage. Further microstructural analysis is needed to identify the nature of these features.

Table 1 Machining Conditions of RBSN specimens from Caterpillar, Inc.

Specimen No.	Power Consumed in Machining (HP)
1	
2	7.5
3	7.2
4	7.8
5	6.0
6	(As received)
7	8.6

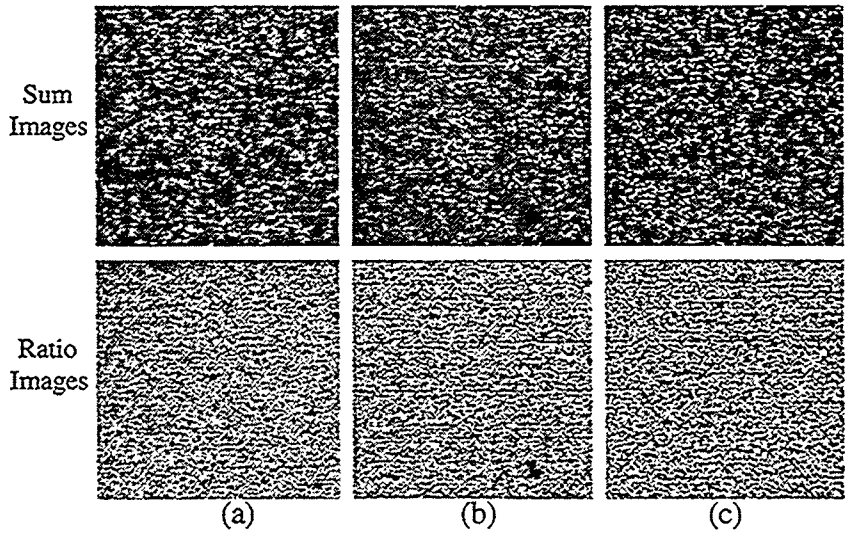

Figure 9 Elastic optical scatter sum and ratio images of ground RBSN specimens: (a) No. 5 with 6.0HP, (b) No. 2 with 7.5HP, and (c) No. 7 with 8.6HP consumed in machining.

We have also performed statistical analysis of the laser scatter data and correlated with machining conditions. The statistical parameter C_v (= standard-deviation/mean) calculated from the laser scatter sum (or intensity) images was determined for all diamond-ground specimens (CAT6 - CAT10). Three machining parameters are used for the correlation: material removal rate (MRR), grit concentration, and grit number. Figure 10 shows the correlation for GS44 specimens, the parameter C_v increases with the MRR, but decreases with the grit concentration. For Ceralloy specimens, shown in Fig. 11, the parameter C_v increases with the MRR, decreases with the grit concentration, and decreases with the grit number. These results are reasonable. However, they are preliminary because there are not enough specimens to establish statistical trends.

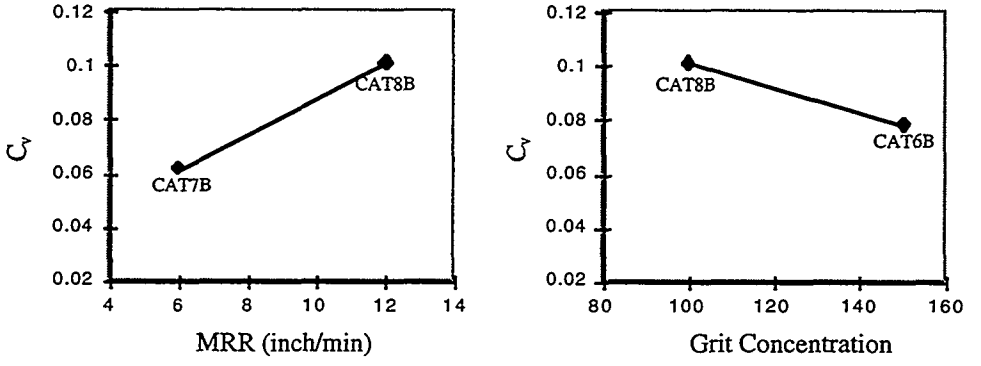

Figure 10 Correlation of C_v derived from the laser scatter sum images of diamond-ground GS44 specimens with (a) MRR and (b) grit concentration.

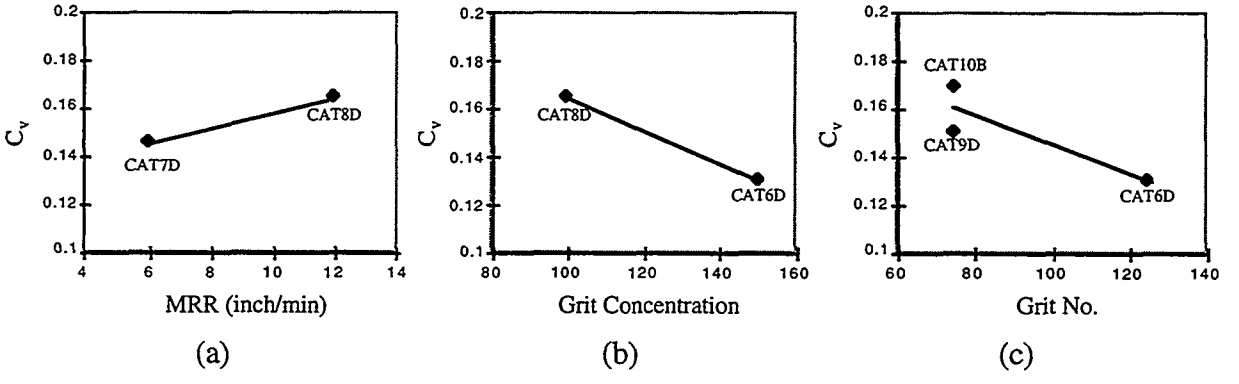

Figure 11 Correlation of C_v derived from the laser scatter sum images of diamond-ground Ceralloy specimens with (a) MRR, (b) grit concentration, and (c) grit number.

The statistical parameter C_v for the ground RBSN specimens (listed in Table 1) has been correlated with the power consumed in machining, as shown in Fig. 12a. For a comparison, Fig. 12b shows the correlation obtained by Caterpillar for a set of similar specimens. Although the values of C_v in the Caterpillar results are less than half of the ANL results, the trends of both correlations are essentially the same, i.e., C_v increases with increasing machining power. One exception was at 7.8HP. We do not know the reason at this moment.

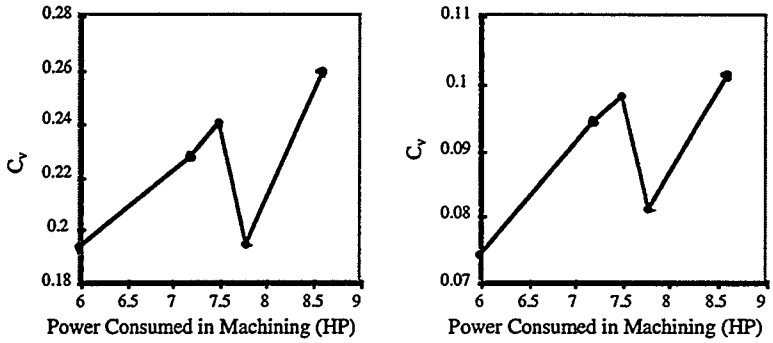

Figure 12 Correlations of C_v derived from laser scatter sum images of ground RBSN specimens obtained by (a) ANL and (b) Caterpillar, Inc.

The statistical parameter C_v derived for the laser-machined/diamond-ground Ceralloy and GS44 specimens is correlated with the specimen strength, as plotted in Fig. 13. A general trend can be observed, i.e., specimens with higher strengths have lower C_v values, or have "smoother" scattering machined surfaces. This result represents a first correlation of the laser scatter data with the specimen mechanical property.

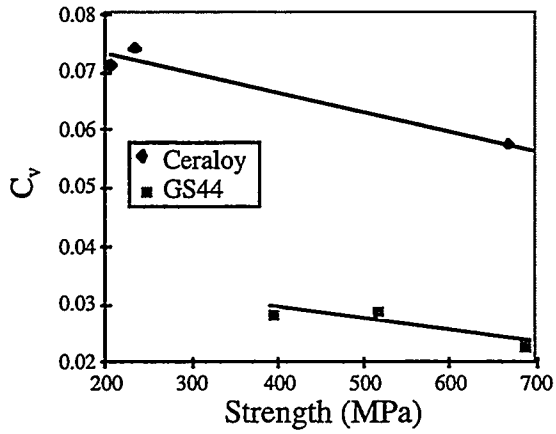

Figure 13 Correlation of C_v derived from the laser scatter sum images with the strength for the laser-machined/diamond-ground Ceralloy and GS44 specimens.

1.B Eaton Samples

We continued optical scattering studies of the ground samples provided by Eaton. Figures 14 and 15 show the elastic optical scattering ratio and sum images of Samples 9703-2-5 and 9703-3-4 which were machined with a vitrified-bond wheel of grit size 180 and at speed 12000 and 18000, respectively. The scanned surface area is 2-mm x 10-mm with a coarse resolution of 20-μm. The optical scatter images of Sample 9703-2-5 show large-scale irregular patterns on the ground surface. These patterns were observed on some other samples machined with vitrified-bond wheels but not on those machined with resin-bond wheels. Further investigation is needed to understand the cause of these patterns.

The statistical parameter C_v was calculated from the sum images of all specimens scanned with the coarse resolution of 20 μm. It is plotted in Fig. 16 as a function of the maximum stress (τ_{max}) of the samples. It is seen that there is a correlation between C_v and τ_{max} in the higher stress

region, i.e., C_v decreases as τ_{max} increases. The scatter of the data is large at the lower stress region, but these data were come from samples machined with vitrified-bond wheels. This correlation will be further examined with additional optical scattering tests at finer resolutions.

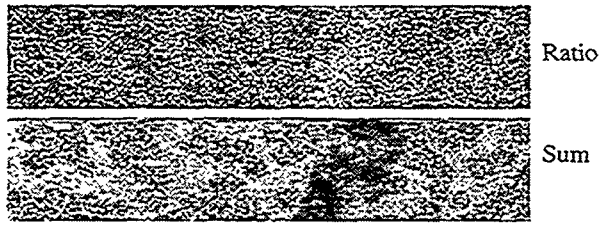

Figure 14 Elastic optical scatter images of ground Eaton sample 9703-2-5 (grit size = 180, speed = 12000).

Figure 15 Elastic optical scatter images of ground Eaton sample 9703-3-4 (grit size = 180, speed = 18000).

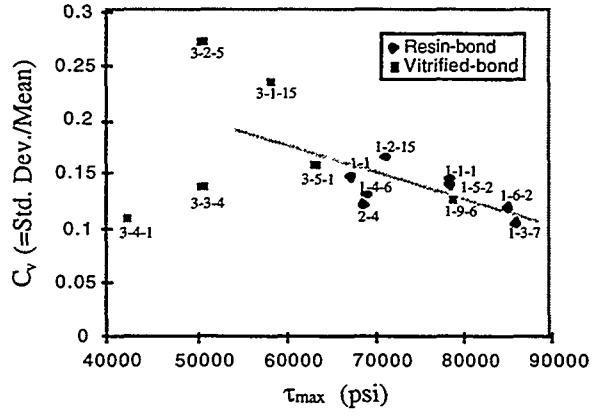

Figure 16 Calculated C_v from optical scatter sum images as a function of maximum stress τ_{max} for Eaton samples.

2. Automation for On-Line Inspection with Optical Scattering

We did not devote any effort to this part of the project this period because we have been working to establish correlations before we continue this work.

3. Impact Acoustic Resonance

We are in the process of adding a scanning laser vibrometer setup so that fundamental mode shape can be correlated to the acoustic signals already received. A single point laser vibrometer was ordered this period (to be delivered Oct. 15) so that fundamental mode shapes can

be correlated to the acoustic signals already received. We plan to output these data to STAR MODAL software to allow determination of the mode shapes. New x-y precision translation stages were ordered, received, and checked out. These were interfaced to the LabView front-end software for data acquisition. We also designed and had fabricated the frame to hold the scanning system.

Status of Milestones

Current ANL milestones are on or ahead of schedule. We are redefining the milestones in view of the current results from the Caterpillar samples.

Communications/Visits/Travel

Travel:

1. W. A. Ellingson and J. G. Sun visited Caterpillar Technical Center at Mossville, IL on April 3, 1998 to discuss project issues.

2. W. A. Ellingson and J. G. Sun visited Caterpillar Technical Center at Mossville, IL on September 10, 1998 to discuss project issues.

Communication:

1. Discussions have been taking place with Eaton Corporation and St. Gobain Industrial Ceramics to obtain additional machined specimens with carefully controlled machining conditions.

Problems Encountered

None this period.

Publications

None this period.

Milestone Schedule

FY97

Complete initial elastic optical scatter data acquisition on high material removal rate (HMRR) Si_3N_4 flat plate specimens.	May 30, 1997	**Completed**
Complete Impact Acoustic Resonance (IAR) data acquisition on HMRR flat plate specimens.	June 30, 1997	**Completed**
Complete microstructural analysis of HMRR specimens and correlate to optical and resonance data.	Sep. 15, 1997	**Completed**

FY98

Complete initial elastic optical scatter data acquisition on low material removal rate (LMRR) Si_3N_4 flat plate specimens.	Nov. 15, 1997	**Completed**
Obtain mechanical properties and correlate data of HMRR specimens.	Dec. 15, 1997	**Completed**
Complete IAR data acquisition on LMRR flat plate specimens.	Feb 15, 1998	**Completed**
Complete microstructural analysis, obtain mechanical properties and correlate data of LMRR specimens.	May 15, 1998	**Completed**
Obtain HMRR and LMRR round specimens of Si_3N_4.	May. 30, 1998	(being redefined)
Complete initial elastic optical scatter and IAR data acquisition of round HMRR and LMRR specimens.	Sep. 15, 1998	

FY99

Complete IAR data acquisition on round HMRR and LMRR specimens.	Nov. 30, 1998
Complete microstructural analysis of round HMRR and LMRR specimens.	Feb. 15, 1999
Correlate IAR and elastic optical data on round HMRR and LMRR specimens.	Apr. 15, 1999
Prepare limited mechanical property specimens from round specimens and correlate to NDE data.	July 15, 1997
Complete and test set up of initial high speed optical scatter system on grinding machine.	Aug. 15, 1999
Submit project report.	Sep. 30, 1999

INTERMETALLIC-BONDED CERMETS

P. F. Becher and C. G. Westmoreland
Oak Ridge National Laboratory
Oak Ridge, TN 37831-6068

Objective /Scope

The goal of this task is to develop materials for diesel engine applications, specifically for fuel delivery systems and wear components (e.g., valve seats and turbocharger components). This will require materials with a minimum hardness of 11 GPa and a thermal expansion coefficient of between 10 to 15 x 10^{-6}/°C over the temperature range of 25° to 300° C. The material should also have excellent corrosion resistance in a diesel engine environment, a flexure strength in excess of 700 MPa, and a fracture toughness greater than 10 MPa m to ensure long term reliability. The material should also be compatible with and not cause excessive wear of the steel counter face. The upper temperature limit for fuel delivery systems applications is 540° C, and for the other wear applications, the limit is 815° C. Finally, the total material processing costs for these advanced materials should be competitive with competing technologies such as TiN or other ceramic coatings on high speed tool steels.

Technical Highlights

Initial wear test results from Cummins indicate that TiC-25 vol. % Ni_3Al cermet with submicron TiC grain size exhibited excellent wear resistance. Wear of metallic counter-face materials is still an issue. However, analysis of the wear processes is incomplete at this time. Samples of these submicron grain size cermets were prepared and a dense submicron grain size TiC cermet that contains ~ 10 vol. % Ni_3Al was sent to Cummins for test and evaluation.

The thermal expansion data over the temperature range of - 100°C to 600°C for seven TiC–Ni_3Al cermets containing from 8 to 40 vol. % Ni_3Al were obtained and analyzed after the repair of the liquid helium cooling system on the low temperature dilatometer. The data were forwarded to Tom Yonushonis of Cummins Engine Company.

The densification responses of two different lots of TiC–Ni_3Al powder mixtures were characterized at the request of Jim Stephen of Advanced Materials Technologies. This study revealed effects of sintering temperature and environment upon as-sintered densities achieved in these two powder mixture lots.

Efforts will now resume on the processing of cermets containing other carbide matrices in an attempt to explore the influence of matrix hardness on the wear response of the cermet versus the steel counterface material in the Cummins wear test environment.

Status of Milestones
On Schedule

Communication/Visits/Travel
In discussions with Jim Stephan of AMT, he revealed that they have had considerable success in processing cermets at the Coors facilities with high strengths with very narrow strength distributions based on our processing approaches and compositions. They will be preparing components for testing by Cummins in the near future. (June 1998).

Presented current status of project and future plans at the Heavy Vehicle Propulsion Systems Materials Program task review held at ORNL on July 22, 1998.

Thermal expansion data on TiC-Ni3Al cermets were sent to Cummins Engine on Sept. 17, 1998.

Problem Encountered
The liquid helium cryostat used with the low temperature dilatometer system developed a vacuum leak. The transfer tube was replaced and cooling unit repaired. Measurements of low temperature thermal expansion coefficients for Cummins were delayed but completed in September.

Publications
K. P. Plucknett and P. F. Becher, "TiC/Ni_3Al Composites Prepared by Melt-infiltration Sintering: Processing and Microstructure Development," submitted to *J. Am. Ceram. Soc.*

COST EFFECTIVE MACHINING OF CERAMIC ENGINE COMPONENTS

S. B. McSpadden, Jr.
T. O. Morris

Oak Ridge National Laboratory
Box 2008, Building 4515
Oak Ridge, Tennessee 37831-6069

Objective/Scope

To develop and demonstrate optimized, cost-effective grinding processes for the production of ceramic components for use in diesel engines.

Technical Highlights

Cooperative Research and Development Agreements (CRADA's)

Work is continuing on two separate CRADA's with Cummins and Caterpillar, respectively. An extension has been requested for the Cummins CRADA, entitled *Precision Grinding of Components for Diesel Fuel Systems Application.* Under the extended CRADA, each party will make additional in-kind contributions valued at $50K. The Cummins principal investigator, Dr. Albert Shih, has recently accepted a position as an associate professor at North Carolina State University and has left Cummins. However, he will continue to work closely with both Cummins and the HTML, and will participate in joint efforts involving ceramic machining. Darryl Gust has been named the Cummins principal investigator for the CRADA.

The Caterpillar CRADA is entitled *Studying the Scuffing Resistance of Zirconia Fuel Injector Components for Diesel Engine Applications.* The initial group of scuffing specimens was ground onder controlled conditions to achieve specific surface roughness values, and have been sent to Caterpillar for further tests. A group of Zirconia specimens was also tested on the Chand Kare Grindability System to determine a relative grindability number for the material. Caterpillar is also discussing a possible extension of the existing CRADA to cover other areas of interest.

High-speed Grinding on the Cincinnati Milacron Centerless Grinder

High speed centerless grinding is being investigated as a cost-effective method for producing ceramic engine components. The process is attractive because the need is eliminated for workpiece fixtures and workpiece alignment. Compared to other grinding processes, centerless grinding is fast, wheel wear rates are low (due to the large surface area of the grinding wheel), and the process produces high quality parts. The work has been delayed due to previously reported mechanical problems. Two diamond-coated work rest blades have been procured and are being installed. Work on ceramic button head tensile specimens is expected to resume before the end of July.

High-Speed Grinding on the Weldon Cylindrical Grinder

As a part of the ongoing CRADA with Cummins Engine Company, four groups of Zr_2O_3 specimens were ground under various conditions on the Weldon cylindrical grinder to determine the effect of wheel speed on grinding ratio. (Grinding ratio is simply the volume of workpiece material removed divided by the

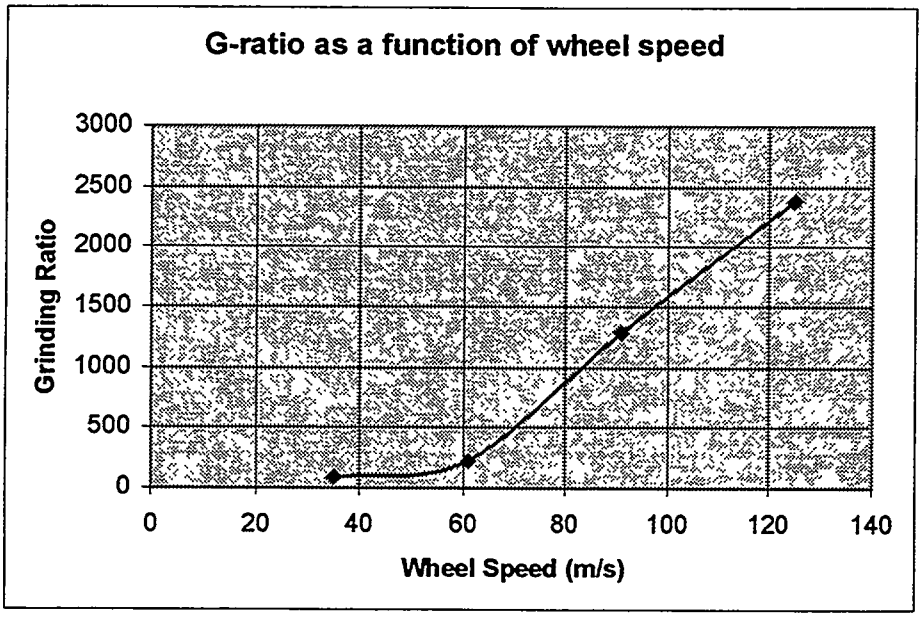

Figure 1. Grinding ratio for Zirconia parts, using a cubic boron nitride grinding wheel with constant in-feed rate.

volume of wheel material expended). As can be seen from the table, much higher material removal rates can be achieved at higher wheel speeds. A higher grinding ratio is advantageous because it means less wheel wear during grinding and better control of form tolerance on the workpiece. The tests were designed to measure grinding ratios at four different wheel speeds – 35, 61, 91, and 127 m/s. The in-feed rate was held constant at 0.34 mm/s for all four wheel speeds. The above tests were repeated to ensure the validity of previous results.

The procedure for G-ratio tests, as shown in Fig. 2, is summarized in the following three steps:

1. The wheel is trued straight and used to grind a zirconia sample at low feed rate. The taper of the part is measured using a laser micrometer. If necessary, the orientation of the work-head is adjusted to minimize the taper on the ground part (Fig. 2a).

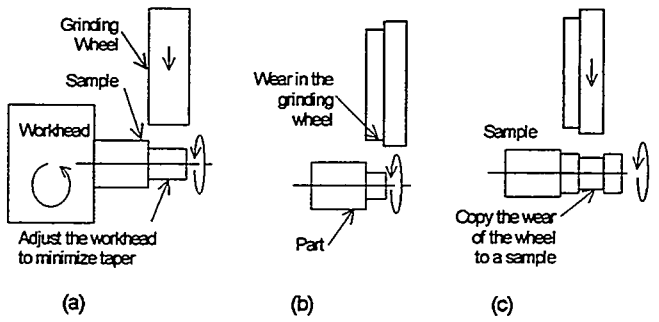

Figure 2. Three steps in the G-ratio tests: (a) orient the work-head to minimize taper on the ground part, (b) perform multiple plunge grinding to produce wear on the wheel and (c) copy the wheel wear to a sample part for measurement.

2. The wheel is then used repeatedly for plunge grinding on the zirconia or silicon nitride workpiece, as shown in Fig. 2b. The objective is to generate measurable wear on the grinding wheel during the test. The diametrical wheel wear needs to be in the 10 to 20 μm range in order to obtain repeatable measurements using simple measuring techniques.

3. After the wheel wear reaches the 10 to 20 μm range, a sample part is touched at slow feed rate to copy the pattern of wheel wear to the sample part (Fig. 2c). Diameters of different sections of the sample part are measured using a laser micrometer. The difference in diameter is used to calculate the

wear of the grinding wheel. Zirconia is used as the material for the sample part. The sample part is ground at a very at low in-feed rate and a small total infeed so that any additional wheel wear is assumed to be negligible.

Because the amount of wheel wear was very small, the wheel-wear profile on the sample part was extremely shallow, and was also tapered. In an attempt to obtain more consistent measurements, a precision coordinate measuring machine was used to scan the wear profile pattern (in addition to the simpler laser micrometer measurement). When the scanning technique was used, analysis software was also used to determine the area under the wear-profile curve. Since the width of the wheel was known, an average "wear depth" was easily computed. This technique is believed to be very accurate, but it proved to be impractical due to the time required for measuring and analyzing the sample part. For zirconia grinding at high speed (127 m/s), the grinding ratio is quite high – over 2000. Therefore, a large number of parts (over 200) had to be ground for a single G-ratio data-point.

Chand Kare Grindability Test System Upgraded

The grindability test system has been upgraded by the addition of a digital tachometer and a load cell, which aid in the calibration of the abrasive belt speed and applied test load, respectively. The equipment is now attached to a dedicated computer system on which a grindability database is being maintained. The database completely automates calculation of the grindability index, which was previously a tedious, manual calculation. Additional studies are planned to quantify the repeatability of this equipment and to develop a more rigorous test standard.

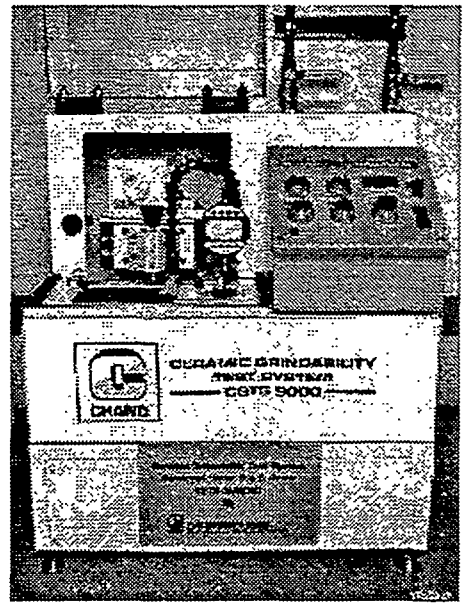

Figure 2. The Chand Kare Grindability Test System.

Upgrade of CAD/CAM Software

Three new 3D CAD/CAM software packages are being evaluated to replace the 2D SmartCAM™ software that is used to program the instrumented grinders. Three-axis programming capability is required in order to machine complex shapes. In order to evaluate the CAD/CAM three packages, a simple alumina test component that requires the use of full 3-axis machining capability was designed, and a machining program was generated for the Sabre 3-axis grinder. The final selection of software will be based on ease-of-use, applicability to work performed by the machining and inspection research group at the HTML, compatibility with widely used CAD/CAM systems in industry, and overall performance.

Communications/Visits/Travel

Sam McSpadden attended the Ultra-hard Materials Conference in Windsor, Ontario (sponsored by the Industrial Diamond Association and the University of Toledo).

Tom Morris and Sam McSpadden attended a Grinding Meeting and Open House hosted by Dr. Steve Malkin at the University of Massachusetts. The stated objectives of the meeting were to provide attendees with an update and overview of the UMASS research program on Grinding Fundamentals and Applications; to discuss the current needs of industry; and to develop productive, collaborative, and leveraged initiatives for grinding research with individual companies and groups of companies. We also visited the Norton World Grinding Technology Center to discuss current activities and possible future collaborations.

Jeff Bougher, Mike Hinrichsen, and Raj Tandon visited the HTML to discuss our respective ceramic machining capabilities and past experiences. The visit also gave Caterpillar manufacturing personnel an opportunity to see the facilities and equipment available at the HTML, and to discuss current and future needs of Caterpillar that might be addressed at the HTML.

Publications

A paper entitled *Vitreous Bond CBN High Speed and High Material Removal Rate Grinding of Ceramics* has been accepted for presentation at the 1998 Annual Meeting of the American Society for Precision Engineering in St. Louis.

TESTING AND CHARACTERIZATION

X-RAY COMPUTED TOMOGRAPHIC IMAGING

W. A. Ellingson, H.R. Lee, E. R. Koehl, H. P. Engel
Argonne National Laboratory
and D. Twait, AlliedSignal Ceramic Components

Objective/Scope

Last year, because of changes in the ceramic materials under study for diesel engines, the objective of Phase III was redefined to the study of 3D density variations in slip cast GS-44 material with chopped carbon fiber. GS-44 material with chopped carbon fiber is being developed as a candidate material for diesel engine valve guides with reduced wear. Caterpillar is a cooperating partner. The selected approach to the nondestructive evaluation of this material is 3D x-ray computed tomographic imaging with an emphasis on the correlation of image data with subsequent destructive analysis of the sample. Subsequently, however, these materials have not shown the desired wear characteristics and this effort is being refocused. Discussions have taken place with Allied Signal and Caterpillar.

Technical Highlights

The technical highlights will be described in four areas:
1) Discussion of the CRADA work on the new amorphous silicon x-ray detector;
2) Discussion of dual-energy x-ray CT technology; and
3) Discussion of the new GS-44 specimens.

X-Ray Detector (Amorphous Silicon) CRADA

The ANL - EG&G CRADA, signed on August 4, 1997, is set up to test EG&G's new amorphous silicon detector. This detector is a fast, high-sensitivity, x-ray area detector which will be used for sensing density gradients in ceramic materials such as the GS-44/chopped carbon samples being developed by Allied-Signal Ceramic Components, Torrence, CA

Manufacturing problems delayed receipt of the detector until March 1998. EG&G delivered the new area detector, model MX-1024, s/n 002, on March 17. This detector is a 2-dimensional array of 100 um pixels, 10 cm by 10 cm square with 12-bit dynamic range. Heat dissipation methods are under development because of a need to dissipate 30 watts of heat. An aluminum frame to allow convection cooling to ambient room air was designed and is being fabricated at ANL.

Also, extensive effort was devoted to selection of a 16-bit A/D board. Three main vendors were selected for further discussions and the DIPIX technologies XPG-1000 board was selected.

One initial issue was the need to identify the pin connectors to allow communication between the A/D board and the MX-1024 detector.

An interim cable was assembled and connected between the XPG-1000 interface and MX-1024 detector. This configuration allowed signal synchronization line "break-out" for initial setup and diagnostic purposes. Signal synchronization is an issue. The detector is essentially a "free-running" device which tells the interface when data is ready. Cable length, type, and termination affect the quality of the timing signals.

We worked closely with Dipix Technologies to develop a working software driver for the XPG-1000/MX-1024 link. This driver is a Dynamic Load Library, which runs under Windows 95 and is callable by LabView 5.0. The driver performs all signal synchronization, detector control, and data acquisition. Currently, full data frames are acquired from the detector every 125 mS.

Images have been acquired from the EG&G detector, but the quality of these images suffers from severe defect anomalies typical in early prototype designs. A typical image from detector S/N 002 is seen in Fig. 1. EG&G is planning on replacing the current detector (Serial number 002) with an improved design in the near future.

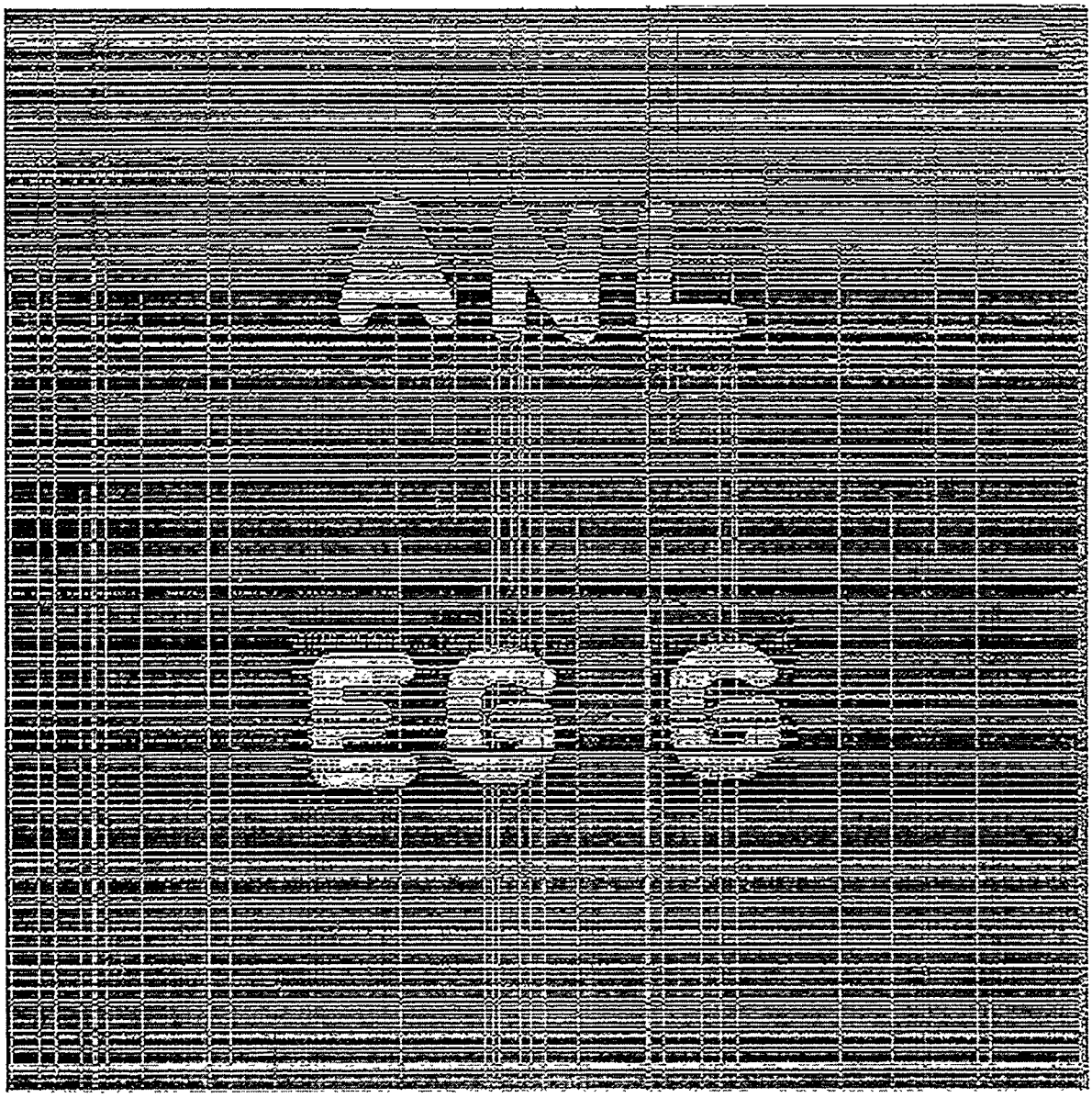

Fig. 1. Demonstration of image acquisition for new amorphous silicon detector showing typical high noise image obtained. This detector is serial number-002 and has many bad pixels.

Additional problems addressed included:

1. Learning how to handle the high clock speed and high computer component density which present a heat management issue affecting the operation of the software interface. Additional cooling fans were installed on the computer.

2. Continue development of a more efficient software driver for the detector.

April 1998 – September 1998

3. Learned how to handle image distortion from production flaws and reduced dynamic range, 12-bit not 16-bit

Also, during this period a new replacement detector (S/N 007) was received to replace the previous S/N 002 detector. This new detector S/N 007 represents the status of production run detectors.

Prior to receipt of the new detector, a system malfunction occurred in the data acquisition computer due to a malfunction in the interface board. It is believed that a heat related failure caused the Dipix XPG-1000 detector interface board to quit operation. During this period the board was returned to the vendor, analyzed, and replaced under warranty. The new detector was initially tested after this repair.

To prevent overheating in the future, the CPU cabinet of the computer was modified with four fans (2 push and 2 pull) to move 200 cfm of air through the cabinet. The Dipix interface board generates a significant amount of heat in the VLSI circuit modules as does the on-board RAM. As delivered, the standard CPU cabinet moves only 30 to 60 cfm. The upgraded air system allows the replacement board to now operate "near ambient" temperature.

We noted last period that a custom cable was needed. This custom interface cable was received in August. It will be checked out and used on the upgraded equipment.

The new detector, S/N 007, was tested with the 125 kVp microfocus x-ray machine. The data obtained suggests that the efficiency of x-ray-to-visible-light conversion screen Lanex, is poor and the detector could not, at the moment, be a favorable device for real-time image acquisition. It can be improved by replacing the converter with other type of scintillator. Figure 2a shows a dark current image (without x-ray power) and Fig. 2b shows an x-ray image of a letter '4' made of lead, which was taken at 12.5 cm from x-ray source operating at 85 kVp, 0.5 ma. As shown in Fig. 2b, the area irradiated by x-rays is a circular region. Image artifacts which appear as white lines and dots in the letter image correspond to detector cells that do not have enough energy to generate image. Figure 3 makes this more obvious. The longer the distance from the detector to the x-ray source, the higher the number of white lines in the image. Further test is currently underway.

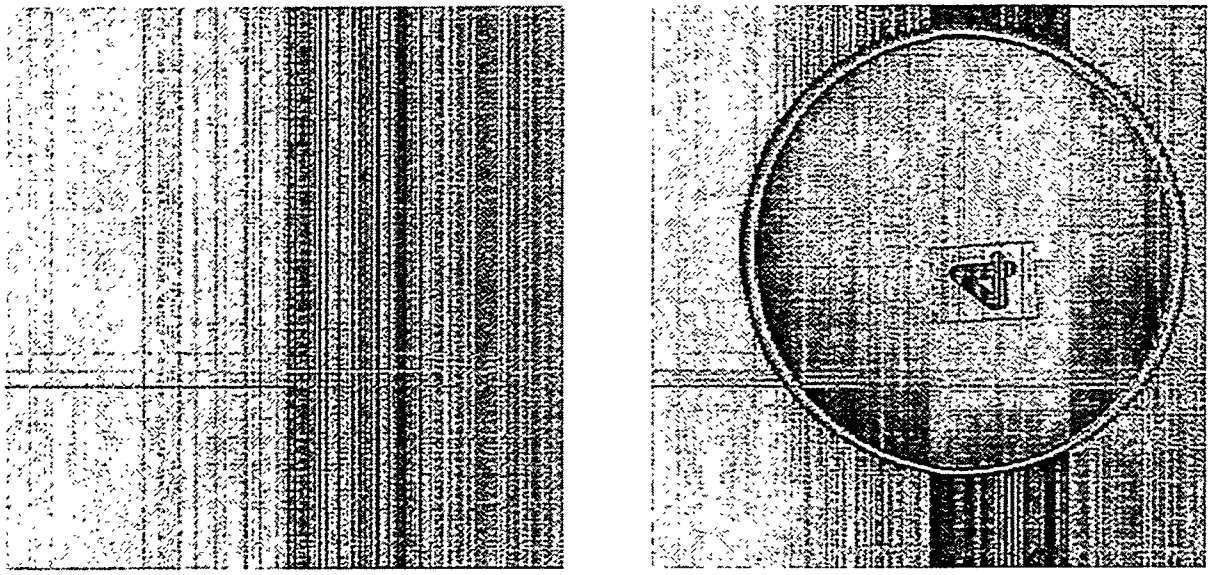

(a) (b)

Fig. 2. MX-1024 Amorphous Silicon detector data. (a) Dark current image (no x-ray incidence); (b) X-ray image (uncorrected) taken at 12.5 cm with X-ray source at 85 kVp, 0.5 ma.

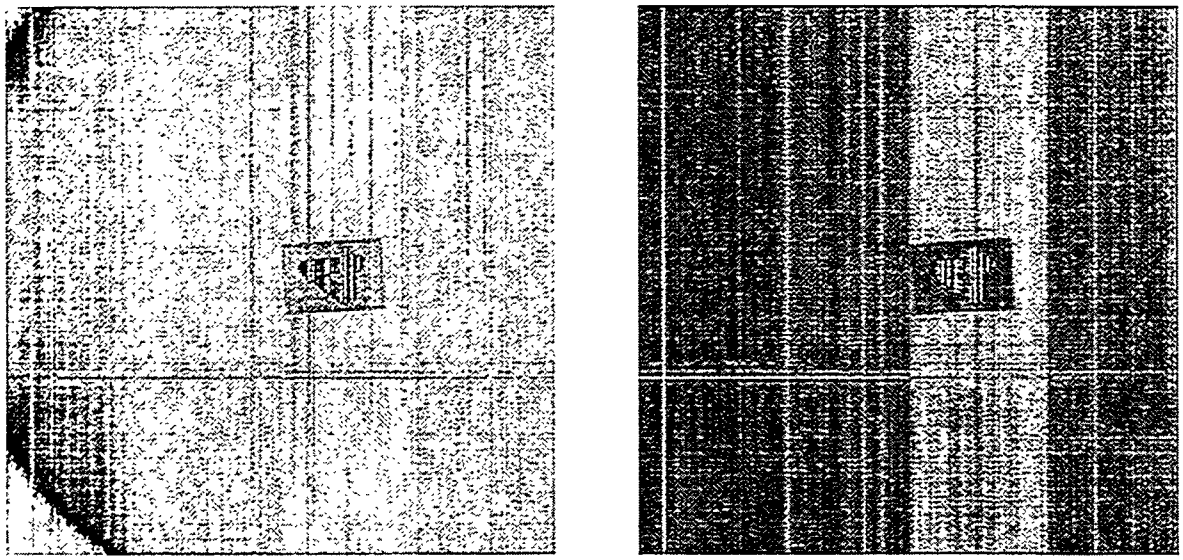

(a) *(b)*

Fig.3. X-ray images taken at two different positions of the detector: (a) image taken 25 cm away from source and (b) image taken 38 cm away from source. The number of white lines and dots in the number 4, which mostly appear as lines in these demagnified pictures, increases with distance. These lines are caused by the small number of photons that the detecting pixel receives.

April 1998 – September 1998

Dual energy computed tomography

At the moment, we have concluded that the GS-44/chopped carbon fiber samples used for densitometry sets are not favorable to dual energy analysis (DEA) because no significant difference exists in density or atomic number between the two main component materials, silicon and carbon, whose density is 2.33 and 2.26 g/cm3 respectively. Prior test for DEA were done by using aluminum (Al) and plexiglass (Pl), whose density is 2.70 and 1.18 g/cm3, as basis materials. Basis functions of these materials, expressed as four independent equations were determined by using the logarithm of normalized intensity as function of thickness.

Eq. 1 $$\ln \frac{I_o}{I}\Big|_{H,Al} = 0.08768 t_{Al}$$

Eq. 2 $$\ln \frac{I_o}{I}\Big|_{L,Al} = 0.11927 t_{Al}$$

Eq. 3 $$\ln \frac{I_o}{I}\Big|_{H,Pl} = 0.04747 t_{Pl}$$

Eq. 4 $$\ln \frac{I_o}{I}\Big|_{L,Pl} = 0.05860 t_{Pl}$$

Examples of projection image data are shown in Fig. 4. This shows projection images of step wedges of aluminum and plexiglass with an overlapped region.

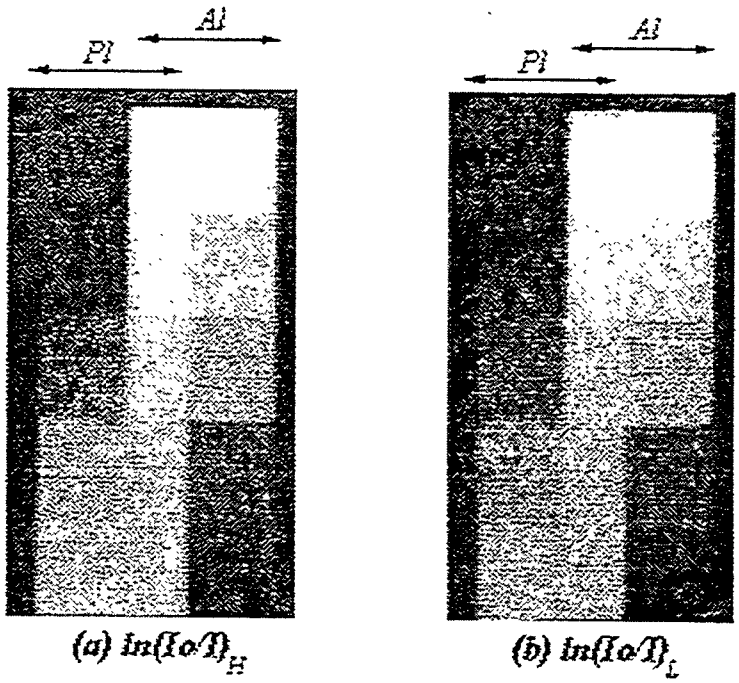

Fig. 4. X-ray image of step wedges using log normalized transmission data: (a) image taken at 130 Kvp and (b) image taken at 86 Kvp.

Figure 5 shows resulting basis function images which represents the thickness of each basis material. It demonstrates that the small deviation in density or in atomic number between the two materials under examination cannot overcome the high background noise. Thus, these basis images could not be used for 3D reconstruction.

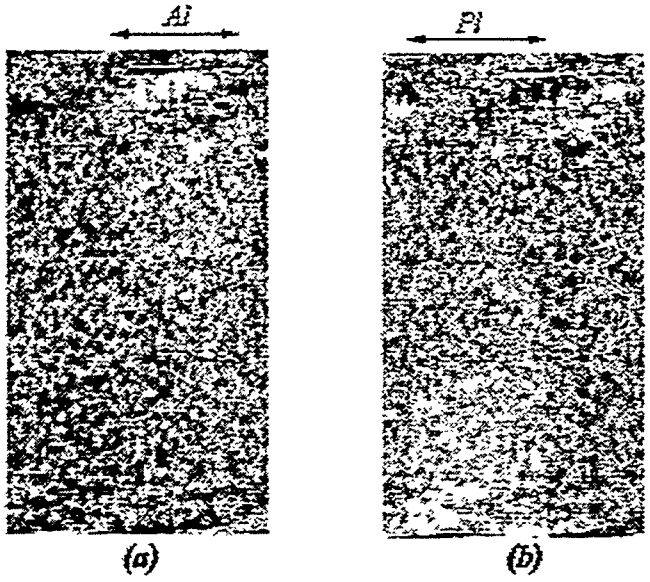

Fig.5. Basis function images of step wedges: (a) aluminum basis image and (b) plexiglass oasis image.

Densitometry based on computed tomography

Work continued relative to use of x-ray tomographic imaging for densitometry of chopped carbon for all data on GS-44 specimens. These were quantitatively analyzed for relative density and density variation depending on carbon-fiber concentration. As before, the chopped carbon is Amoco P-75 and the GS-44 is spray dried. Sample set two used dry-bag cold isostatic pressing (CIP) and set one used wet-bag CIP. Chopped carbon content was 7.5, 10, 12.5 vol.%. The x-ray CT reconstruction from each data set shows different density profiles through the samples. The x-ray CT sections were taken at axial locations as noted in Fig. 6.

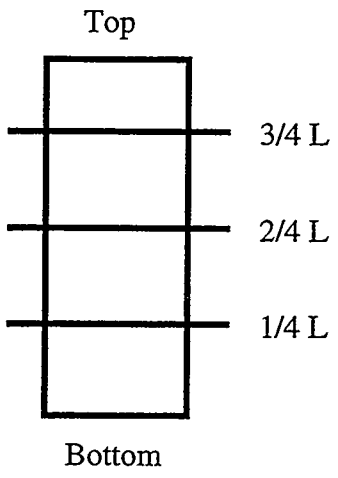

Fig. 6. Schematic diagram showing axial locations of 2 mm thick x-ray CT image data

We ran data on 2 x-ray CT machines. Initially we used a high spatial resolution 160 kVp machine. And now we have used a lower resolution, higher power system. This is a 320 kVp system with a far less sensitive detector. The detector is still an image intensifier/CCD set-up but the camera is only 8-bit dynamic range.

Because of the higher power, with the 320 kVp machine, we were able to do 6 specimens at one time. The specimen test set up we used is shown in Fig. 7.

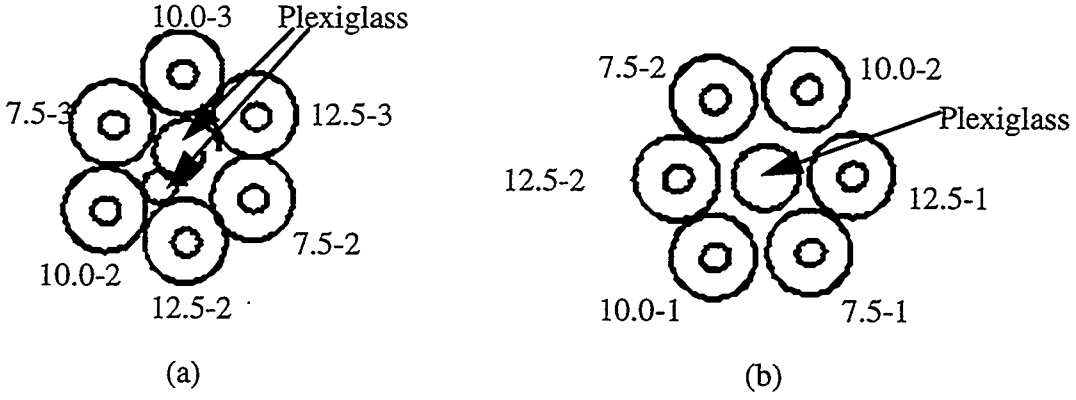

Fig. 7. Schematic diagram showing sample arrangement for 6 specimen simultaneous data acquisition: (a) sample set 1 (wet-bag CIP); (b) sample set 2 (dry-bag CIP).

Typical x-ray CT image data are shown in Fig. 8 for each sample set. Note that we added a plexiglass rod in the middle of the samples so we could normalize the data to this material.

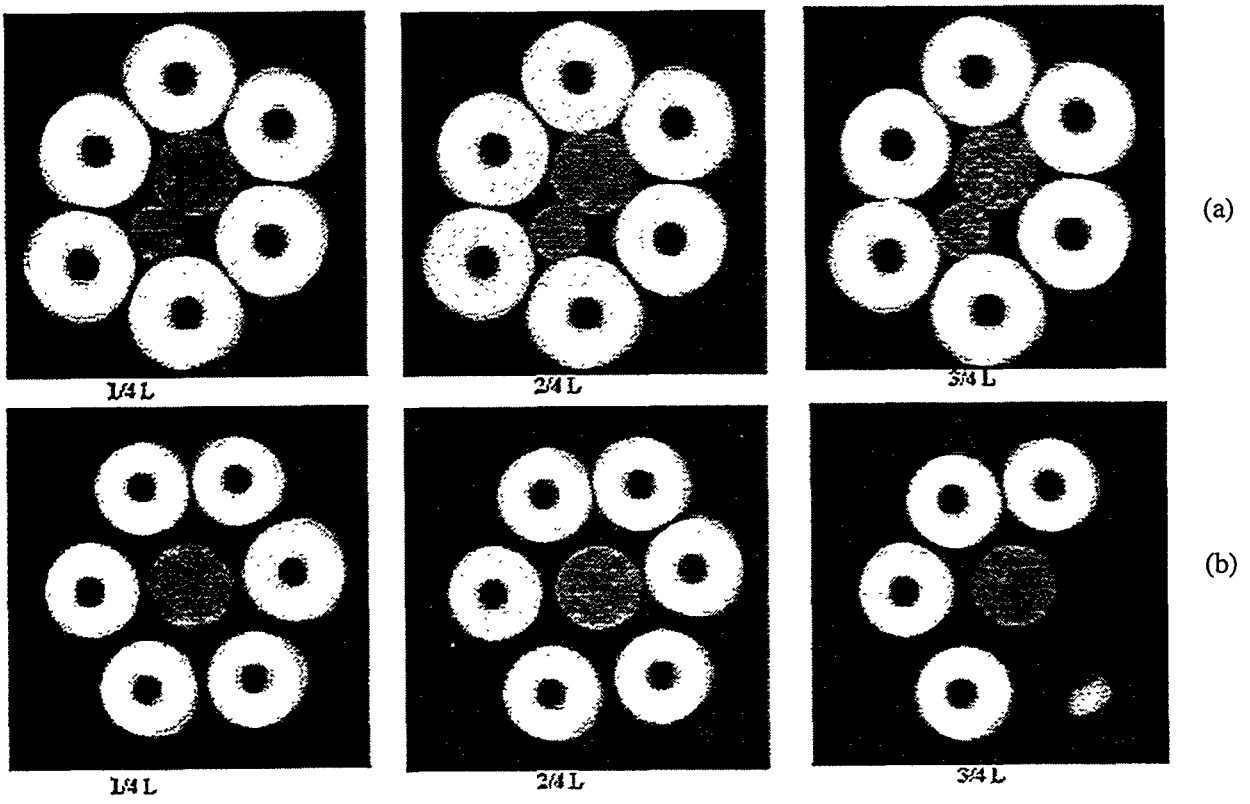

Fig. 8. 320 kv X-ray CT images of 6-specimen simultaneous data acquisition. The orientation of samples was shown in Fig. 6: (a) Sample set 1 (wet-bag CIP); (b) sample set 2 (dry-bag CIP).

Table 1 summarizes the density profiles of sample set number 1 from the different axial locations of the samples at two x-ray energy levels, 130 kVp and 86 kVp. Table 2 summarizes the density profiles of sample set number 2 from different axial location. These show ~2% deviation from the average density and that density depends on sampling location and demonstrates that the higher the carbon-fiber concentration, the lower the density. Further it shows that the density of each sample varies with ~15%. Figure 9 is a plot of density profile of sample set-1 at 130 kVp as a function of axial position. For all samples, the density of middle portion is higher than that either end.

Table 1. Density data of sample set 1 as measured by x-ray CT

Density Profile of Sample Set 1								
	130 kVp				86 kVp			
	1/4 L	2/4 L	3/4 L	Average	1/4 L	2/4 L	3/4 L	Average
7/5 - 2	2.39	2.41	2.32	2.37	2.71	2.76	2.64	2.70
7.5 - 3	2.37	2.39	2.34	2.37	2.72	2.75	2.67	2.71
10.0 - 2	2.32	2.34	2.28	2.31	2.64	2.68	2.58	2.63
10.0 - 3	2.31	2.33	2.26	2.3	2.63	2.68	2.57	2.63
12.5 - 2	2.27	2.29	2.23	2.26	2.59	2.63	2.53	2.58
12.5 - 3	2.28	2.28	2.23	2.26	2.6	2.62	2.55	2.59

Table 2. Density data of sample set 2 as measured by x-ray CT

Density Profile of Sample Set 2								
	130 kVp				86 kVp			
	1/4 L	2/4 L	3/4 L	Average	1/4 L	2/4 L	3/4 L	Average
7.5 - 1	2.57	2.58		2.58	2.9	2.95		2.93
7.5 - 2	2.56	2.57	2.58	2.57	2.9	2.95	2.92	2.92
10.0 - 1	2.52	2.54	2.51	2.52	2.85	2.93	2.91	2.90
10.0 - 2	2.54	2.55	2.52	2.54	2.86	2.93	2.92	2.90
12.5 - 1	2.47	2.48	*	2.48	2.77	2.83	*	2.8
12.5 - 2	2.45	2.46	2.45	2.45	2.77	2.82	2.76	2.78

*Chipped area of sample, no data obtained.

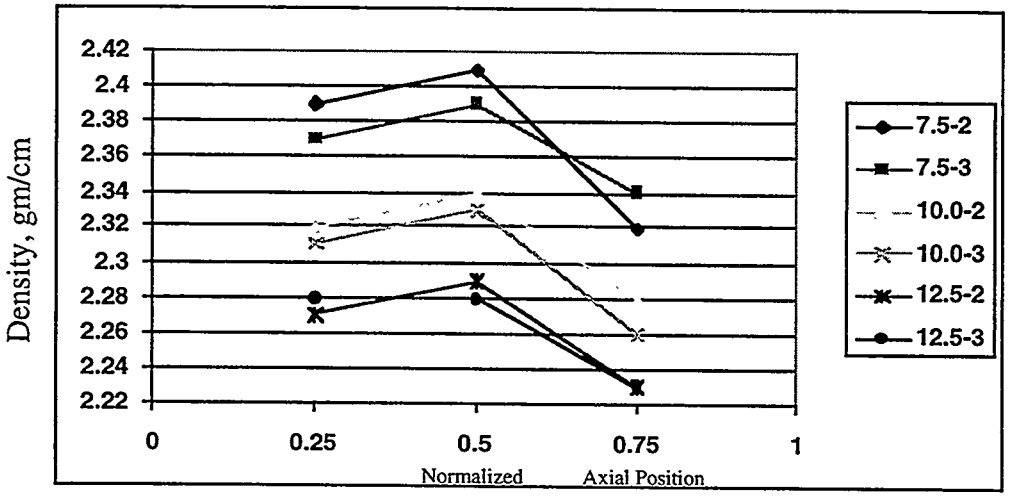

Fig. 9. Effect of chopped carbon fiber loading on density as determined by x-ray CT for set number one.

Figure 10 below shows a plot of axial density for sample set number 2. Note that there is far less density variation than in sample set one.

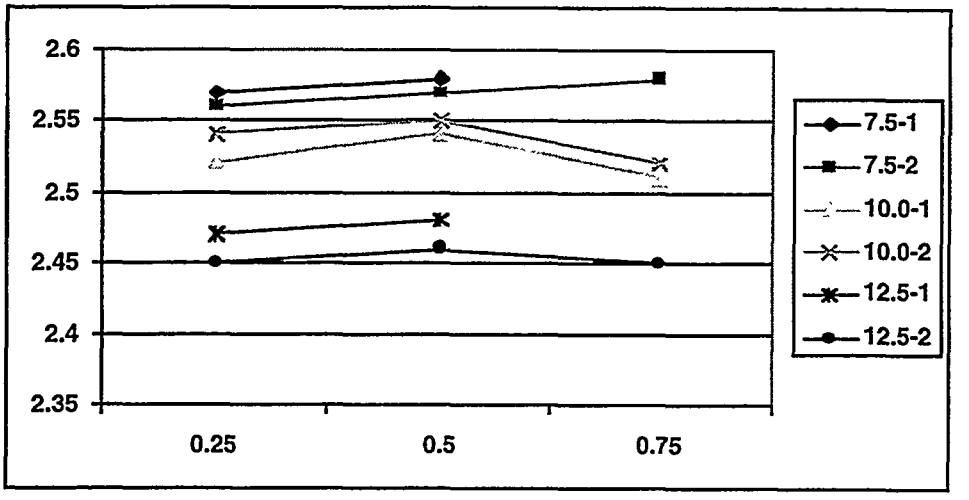

Fig. 10. Effect of chopped carbon fiber loading on density as measured by x-ray CT for sample set number 2.

Other Items

The entire existing x-ray facility 3 machines, is being moved from Building 331A to Building 212, G-wing. This is to be completed by December 25, 1998.

TESTING AND EVALUATION OF ADVANCED CERAMICS AT HIGH TEMPERATURE

J. Sankar, A. D. Kelkar and L. Russell (Department of Mechanical Engineering, North Carolina A & T University, Greensboro, NC 27407)

Objective/Scope

The objective of this research is to test and evaluate the long-term mechanical reliability of a Si_3N_4 at temperatures up to 1300^0C. The required research includes four (4) major tasks:

Task 1. Cyclic Fatigue Testing of PY6 and GS 44

Cyclic fatigue of GTE-PY6 and GS 44 silicon nitride shall be performed at lower temperatures to investigate characteristics of the material at the temperature range of 500^0 - 1100^0C. At these lower temperatures, there may be a true cyclic fatigue effect that enhances failure compared with the static load case.

Task 2. Stress-Rupture Study of PY6 and GS 44

Stress-Rupture testing of GTE-PY6 and GS-44 silicon nitride shall be performed at a lower temperature range of 500^0 - 1100^0C. Since there is little information about the time dependent behavior of this material is available at this temperature regime, this task should provide some valuable data.

Task 3. Four (4) Point Flexural Test

Four (4) point flexural tests shall be performed for AlliedSignal's GS-44 silicon nitride from room temperature to elevated temperature.

Task 4. Thermal Barrier Protective Surface Coating

A basic science understanding of thermal barrier protective surface coating to promote high-temperature performance and the effects of notches and oxidation at the roots of the notches at elevated temperatures for silicon nitride shall be carried out.

Task 5. Microscopy

High-resolution microscopy and fractography work will be a part of all tasks discussed above.

Technical Highlights and Discussion

During this reporting period, flexural experimental data and finite element analysis modeling were completed on GS-44 silicon nitride specimens.

Objective/ Scope

The objective of this research is to develop a numerical model that will simulate the experimental conditions of a four-point bend flexural test. A finite element model (FEM) was developed to compare with the data from the four-point bend flexural test performed on GS-44 silicon nitride specimens. The American Society of Testing and Materials (ASTM C 1161-9) Standard Test Method for Flexural Strength of Advanced Ceramics at Ambient Temperature was followed as a guide for testing. Test were performed on six tests specimen at room temperature using displacement control. Applied Test Systems, Inc., Butler, PA, Four Point Bend Test Series 1605 Computer-Controlled Universal Testing Machine was used to generate flexure strength, Young's modulus, and strain energy. A comparison between finite element modeling, mechanics of materials, and experimental analysis was conducted to determine any variance in results between the three methods.

Experimental Data

Material

The material used for investigation is sintered silicon nitride, GS-44, provided by Allied Signal. The dimensions for the samples used in the bend test are 3 x 4 x 45 millimeters. Earlier studies on silicon nitride states it contains small amounts of Y_2O_3, Al_2O_3, and other minor constituents as densification aids.

Four Point Bend Test

Four-point bend test consists of measuring the deflection of a simple beam subjected to symmetrical loading. The test set-up uses Applied Test System's 4231 High Temperature Bend Testing Extensometer, along the Applied Test System's software TestVue. TestVue software was developed to perform compressive, tensile, and cyclic testing. Acquires multi-point data (time, displacement, load, stress, and auxiliary), and rapidly converts between units, stores batch, and specimen test. Model 1605 has a 5,620 pound capacity. All experiments were conducted using displacement control at 0.5 mm/ minute. Displacement control is the distance of cross- head motion during testing per unit of time.

Mechanical Properties

The modulus of elasticity in bending was determined by using the load verse displacement data from the four-point bend test. The load and deflection data was inserted into equation (1) the modulus of elasticity equation for four-point bending. Where, E_b is the modulus of elasticity in Pa; L is the distance between the two outer support pins, mm; t is the specimen thickness, mm; w is the specimen width, mm; a is the distance between the two inner support pins, mm (load applicators); ΔP is the increment in load, Newtons; $\Delta\delta$ is the increment in displacement. Equation (2) derived from the deflection equation using the double integration technique can also be used to determine the modulus of elasticity when solving for E_b, Young's modulus.

$$(1)\ E_b = \frac{a\,(3*L^2 - 4*a^2)}{4*w*t^3}\,\frac{\Delta P}{\Delta\delta}$$

$$(2)\ E_b = \frac{11*P*L^3}{768*I}\,\frac{\Delta P}{\Delta\delta}$$

The flexural strength is determined by the amount of load the specimen can withstand during bending. The experimental normal stress derived from the standard formula, equation (3) used to determine the flexural strength.

$$(3)\ \sigma_{max} = \frac{3PL}{4wt^2}$$

Where P is the applied load; L is the distance between the two outer support pins, mm; t is the specimen thickness, mm; w is the specimen width, mm.

Finite Element Analysis Modeling

Finite element analysis was completed with the assistance of Dr. Jim Lua, Engineering Technology Center, Applied Mechanics Department, Mystic, CT. The finite element model was developed to compare with the data from the four point flexural test performed on the GS-44 silicon nitride specimen.

The finite element model was developed using NASTRAN. Finite element analysis was used to analyze the structure in order to determine the state of stress in the four-point bend test experiment. Finite element analysis, is a numerical tool that converts the underline differential equations representing engineering problems into algebraic equations which are solved to obtain the solution of the problem. Finite elements are subdivided within the domain of

the structure and interconnected at points around each element called nodes. By subdividing the structure into elements and applying boundary conditions, each element can be numerically solved and combined to obtain the solution for the entire model. A three dimensional model was developed using brick elements with three degrees of freedom.

Comparison: Experimental vs. Finite Element Model

The results of the finite element model were consistent with the data from the four point flexural test. Fig. 1 demonstrates how the load-deflection curves from the finite element model results and the experimental data are within acceptable range. Fig. 2 shows the deflection of the deformed beam under unit load. Tables (1) and (2) display total load, normal stress, and displacement at the center of the beam from the experiment and the FEA model. Table (2), contains the absolute percent error of the normal stress between the experimental data and the FEA model results. The absolute error was calculated by using equation (4).

$$(4)\ \text{Absolute Error} = \frac{|\text{FEM result} - \text{Experimental result}|}{\text{FEM result}}$$

It can be seen from the table 2 that the finite element results and the experimental data are with in two percent using equation (4).

Table 1. Finite Element Results using Ex = 309 GPa; G= 128.8 GPa

Load / Node	Total Load	Displacement	Normal Stress
0.1 N	1 N	.000334 mm	.842 MPa
0.5 N	5 N	.00167 mm	4.21 MPa
5	50	.0167	42.1
20	200	.0668	168
40	400	.134	337
80	800	.267	673

Table 2. Experimental and Mechanics of Materials Results

Total Load	Displacement	Normal Stress	Absolute Error
1 N	0.00033 mm	.833 MPa	1.06 %
5	0.00165	4.16	1.18
50	0.0165	41.6	1.18
200	0.0659	167	0.60
400	0.132	333	1.18
800	0.264	667	0.89

Status of Milestones

On Schedule

Communications/Visitors/Travel

1. Ray Johnson, visited N.C. A&T SU and gave a talk as a part of ASM International Piedmont chapter seminar series.

2. Jag Sankar presented, "Microstructure Changes Associated with Tensile Creep of an in-situ Self Reinforced Si_3N_4", at the MRS meeting, Boston, Dec. 1998.

Problems Encountered

None

Fig. 1 Comparison of FEM Results with Experimental Data
(Load-Deflection Curve)

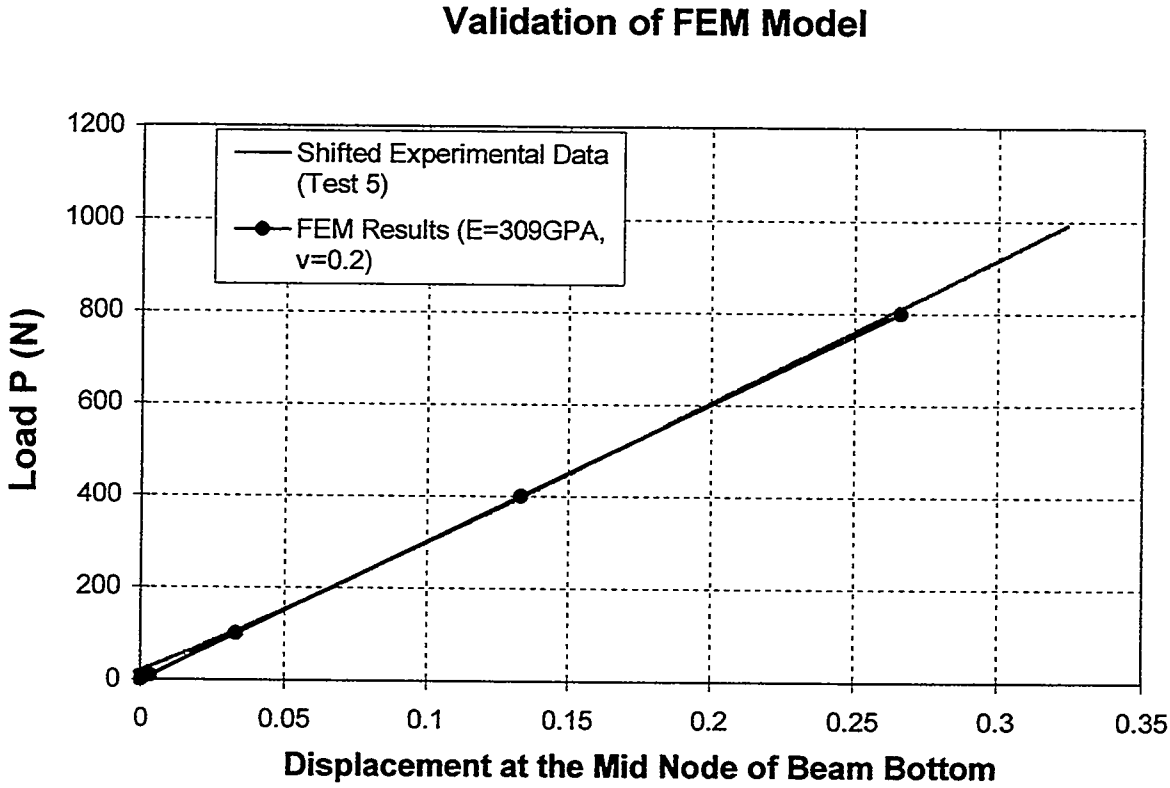

Fig. 2 Deformed Beam Under Unit Load

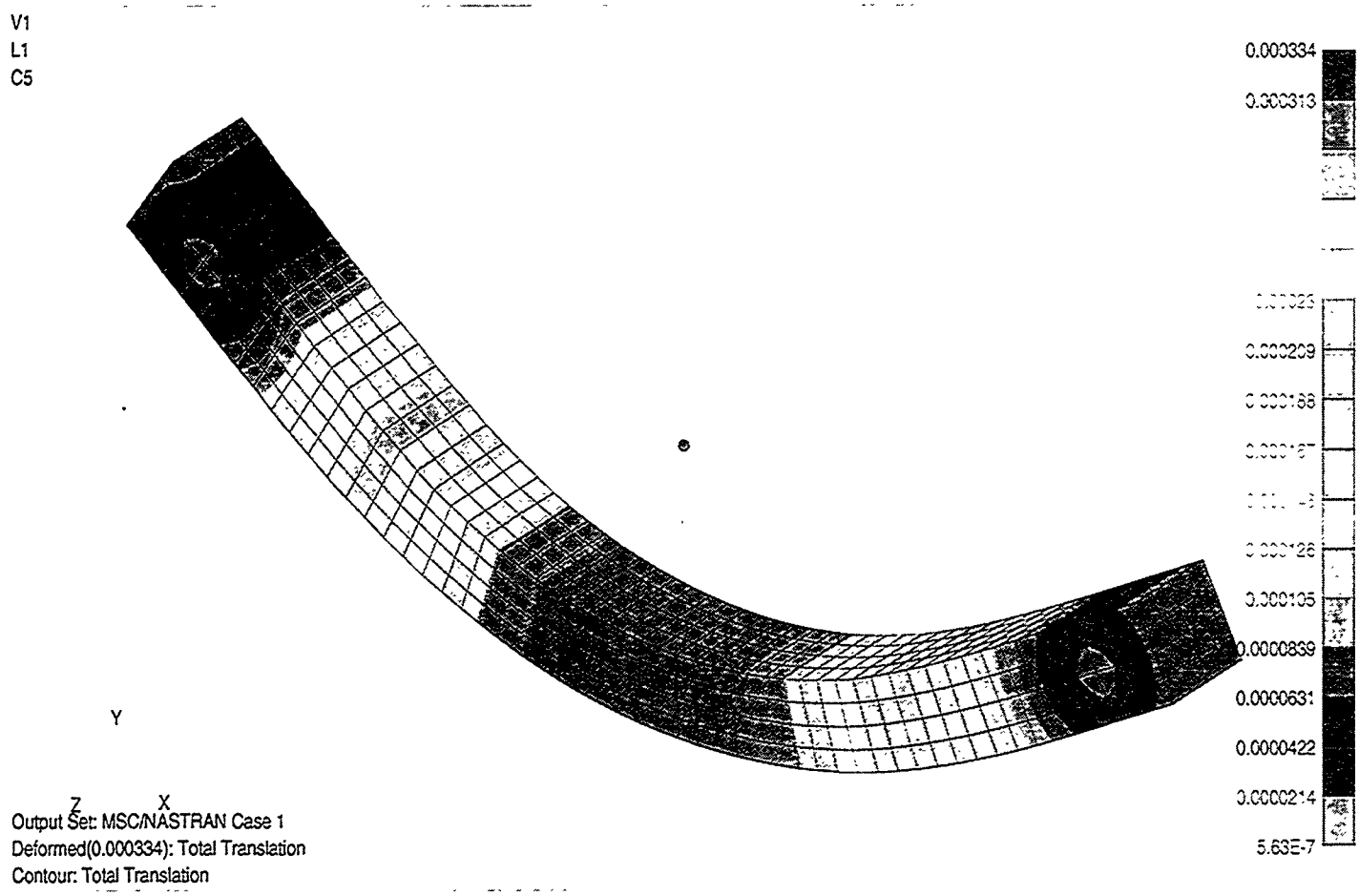

Research sponsored by the U.S. Department of Energy, Assistant Secretary for Energy Efficiency and Renewable Energy, Office of Transportation Technologies, as part of the Heavy Vehicle Propulsion System Materials Program under contract DE-AC05-96OR22464 with Lockheed Martin Marietta Energy Research Corporation.

Life Prediction of Ceramic Diesel Engine Components

A. A. Wereszczak, M. J. Andrews, T. P. Kirkland, and M. K. Ferber (ORNL)

Objective/Scope

The valid prediction of mechanical reliability and service life is a prerequisite for the successful implementation of structural ceramics as components in internal combustion engines. There are three primary goals of this research project which contribute toward that implementation: the generation of mechanical engineering data from ambient to high temperatures of candidate structural ceramics; the microstructural characterization of failure phenomena in these ceramics and components fabricated from them; and the application and verification of probabilistic life prediction methods using diesel engine components as test cases. For all three stages, results are provided to both the material's supplier and component end-user.

The systematic study of the mechanical performance of candidate structural ceramics (primarily silicon nitride) for internal combustion engine components is undertaken as a function of temperature (< 1000°C), time, and machining conditions. Properties such as strength and fatigue will be characterized via flexure, tensile, and rotary bend testing.

The second goal of the program is to characterize the evolution and role of damage mechanisms, and changes in microstructure linked to the ceramic's mechanical performance, at representative engine component service conditions. These will be examined using several analytical techniques including optical and scanning electron microscopy. Specifically, several microstructural aspects of failure will be characterized:

(1) strength-limiting flaw-type identification;
(2) edge, surface, and volume effects on strength and fatigue size-scaling
(3) changes in failure mechanism as a function of temperature;
(4) the nature of slow crack growth; and
(5) what role residual stresses may have in these processes.

Lastly, numerical probabilistic models (i.e., life prediction codes) will be used in conjunction with the generated strength and fatigue data to predict the failure probability and reliability of complex-shaped components subjected to mechanical loading, such as a silicon nitride diesel engine valve. The predicted results will then be compared to actual component performance measured experimentally or from field service data. As a consequence of these efforts, the data generated in this program will not only provide a critically needed base for component utilization in internal combustion engines, but will also facilitate the maturation of candidate ceramic materials and a design algorithm for ceramic components subjected to mechanical loading in general.

Technical Progress

Numerous tasks were worked on during the present reporting period in preparation for the mechanical reliability analyses of the NT551 DDC Series 149 exhaust valves. The efforts included mechanical testing of NT551 specimens and valves, and their fractography.

Tests specimens:

Fractography of the Vintage #3 NT551 cylindrical and ASTM C1161B specimens neared completion. The strengths of these specimens and their two-parameter Weibull distributions were described in the last reporting period's report. Like the earlier vintages of NT551, two primary strength-limiting flaws have been identified: machining damage (a surface flaw type) and porous regions (a volume flaw type). Most of the transversely machined (320 grit) specimens failed from surface machining damage flaws at 20°C at all three stressing rates (30, 0.3, and 0.003 MPa/s). However, as the test temperature increased (700 and 850°C), the dominating strength limiting flaw type in the transversely machined NT551 were porous regions. Additionally, porous regions were

the strength limiting flaw in specimens longitudinally machined specimens (320 grit) and tested at 20°C. The changes in dominance of one flaw type to the other is indicative of a change in failure mechanism in the NT551 silicon nitride.

Tensile dynamic fatigue testing was initiated using a modified ORNL button-head tensile specimen. Three rates are being used: 30, 0.3, and 0.003 MPa/s. Approximately twenty specimens have been tested so far at 20°C. The strength and fatigue data will be pooled with the other flexure strength data that has been generated to predict the mechanical reliability of the NT551 valves.

Fracture toughness testing of NT551 chevron-notched specimens at 20, 700, and 850°C was completed. A minimum of five specimens were tested at each temperature. The average K_{Ic}'s were 7.1 MPa$\sqrt{m}$ at 20°C, 6.2 MPa$\sqrt{m}$ at 700°C, and 6.0 MPa$\sqrt{m}$ at 850°C. Considering the small-valued standard deviations which resulted for each, this decrease in fracture toughness between 20 and 700°C was concluded to be statistically significant. The trends in fracture toughness will be compared to observed trends in flexure strength.

Valves:

In preparation for the valve testing, the concentricity of all 40 received valves were measured using a form tester in HTML's Ceramic Machining and Inspection Group. Their concentricity was documented, and will be referenced should any of the valves fracture in an anomalous fashion.

Strength testing of the NT551 valves was initiated. A unit constructed by a group in ORNL's Engineering Technology Division is being used for the tests. The face of each valve is hydraulically loaded until fracture results. DDC-supplied valve seats and guides are incorporated in the testing. To date, fifteen NT551 valves have been tested: the head/stem fillet of ten were transversely machined while the remaining five were longitudinally machined. The uncensored Weibull strength distributions of these two sets of NT551 valves are plotted in Fig. 1 and are compared with previously-generated NT451 valve strengths [1]. The NT551 valves having their face/stem fillet longitudinally machined exhibited the highest strengths of the three compared sets. Additionally testing is ongoing along with failure-causing-flaw identification for each tested valve.

The maximum tensile stress during valve testing (and during ideal loading in service) is located on the valve's head/stem fillet surface. Interest existed to quantify (using surface profilometry) the surface finish in this location to determine if it could help explain the observed differences in valve strengths shown in Fig. 1. The surface finish for the NT551 longitudinally machined valves was better than the transversely machined NT551 valves, while the surface finishes of the NT451 and longitudinally machined NT551 valves were more equivalent (see Fig. 2). These surface roughnesses are compared with those from test specimens whose strength distributions are being used to predict the mechanical reliability of these valves. The longitudinally machined NT551 valves were stronger than the transversely machined NT451 valves even though their surface finishes were similar; this indicates that either the NT551 silicon nitride is inherently stronger than the NT451 SiAlON or that the grinding orientation is affecting this observed difference in strength distribution. Preliminary fractography indicates that the former may be responsible due to observed differences in active strength-liming flaws between the two materials; large pores tended to limit the strength of the NT451 valves [1], while both small inclusions, small "porous regions," and machining damage are limiting the strength of the longitudinally and transversely machined NT551 valves. Examples of flaws causing fracture of two transversely machined NT551 valves are shown in Fig. 3.

Future Work:

In FY99, a collaboration will initiate with Caterpillar to evaluate the mechanical performance of candidate diesel component silicon nitrides in diesel exhaust environments. Existing environmental testing facilities at the ORNL/HTML will be used. Various gases and water vapor will be mixed to mimic the exhaust gas from diesel engines. The strength of these silicon nitride materials will be measured as a function of temperature (to ≈ 900°C), environment (ambient vs. exhaust gas), and time (dynamic fatigue). Several meetings and conversations with Caterpillar staff and ceramic suppliers have occurred in preparation of this effort.

Status of Milestones

All milestones are on schedule.

Communications / Visitors / Travel

B. Schenk of AlliedSignal Engines, Phoenix, AZ, visited group members on May 11, 1998 to discuss mutual life prediction research and to give a presentation describing AlliedSignal's Life Prediction project.

A. A. Wereszczak gave a presentation entitled ""Strength Distribution Changes in a Silicon Nitride as a Function of Temperature and Stressing Rate" at the 43rd ASME Gas Turbine and Aeroengine Technical Congress, June 3, 1998, Stockholm, Sweden.

R. Tandon and J. Bougher of Caterpillar visited A. A. Wereszczak and K. Breder on July 15, 1998, to discuss the possible programmatic collaboration of the mechanical characterization of candidate ceramic materials for components in CAT's 3600 Series Engines.

A. A. Wereszczak and M. Andrews met with ORNL's ETD's J. Corum and R. Battiste on July 20, 1998, to discuss testing plans and scheduling for the NT551 valves using their existing valve-face pressurization system.

A project review presentation was given to the OHV's Program Manager, S. Diamond, on July 22, 1998.

A. A. Wereszczak visited the Caterpillar Technical Center, Peoria, IL, on August 28, 1998 to meet with R. Tandon, M. Readey, J. Bougher, and K. Koshkarian to discuss a soon-to-be-started collaborative project involving the high temperature mechanical testing and characterization of silicon nitride materials in diesel exhaust environments.

A. A. Wereszczak and M. J. Andrews visited Saint-Gobain Industrial Ceramics, Northboro R&D Center, Northboro, MA, on September 15-16, 1998 to discuss inter-related valve R&D work with V. Pujari and D. Jacobs, and to attend the Final Progress Review Meeting of the Advanced Ceramic Manufacturing Technology Program.

Saint-Gobain's V. Pujari and L. Broderick will be forwarding engine-tested NT551 valves to the project and their residual strength will be measured and compared with presently described NT551 valves (*i.e.*, "as-received" or non-engine-tested). Interest exists to see if the service conditions have affected the strength of these valves; this would be indicative of slow crack growth should a strength decrease be observed.

Arrangements were made to acquire diesel-component-candidate silicon nitride materials for environmental mechanical testing in support of the new collaborative project with Caterpillar. AlliedSignal Ceramic Components's J. Pollinger will be supplying isopressed AS800 and GS44 billets to the present project. Billets of CFI's N7202 silicon nitride were also ordered through R. Walecki (a CFI representative). Lastly, arrangements were made with Kyocera's E. Craft and D. Carruthers to acquire their new developmental grade of silicon nitride, SN237, once it is available (≈ March-April 1999).

Problems Encountered

None.

Publications

A poster entitled "Fast Fracture Life Prediction of a Cylindrical Component Using Standard and Nonstandard Four Point Flexure Test Specimens," was presented by M. J. Andrews at the 100th Annual Meeting of the American Ceramic Society, May 5, 1998, Cincinnati, OH.

"Investigations of the Weibull Modulus as a Function of Stressing Rate," by M. J. Andrews, A. A. Wereszczak, K. Breder, T. P. Kirkland, and M. K. Ferber, In press, *Ceramic Engineering and Science Proceedings*, Vol. 19, 1998.

"Asymmetric Tensile and Compressive Creep Deformation of Hot-Isostatically-Pressed Y_2O_3-Doped Si_3N_4," by A. A. Wereszczak, M. K. Ferber, T. P. Kirkland, A. S. Barnes, E. L. Frome, and M. Menon, In press, *Journal of the European Ceramic Society.*

"Strength Distribution Changes in a Silicon Nitride as a Function of Temperature and Stressing Rate" by A. A. Wereszczak, K. Breder, M. J. Andrews, T. P. Kirkland, and M. K. Ferber, *Paper # 98-GT-527, June 1998 ASME Gas Turbo Expo, Stockholm.*

References

[1] J. M. Corum, R. L. Battiste, R. C. Gwaltney, and C. R. Luttrell, "Design Analysis and Testing of Ceramic Exhaust Valve for Heavy Duty Diesel Engine," CRADA Y12 92-0088 with Detroit Diesel Corporation, ORNL/TM-13253 (1996).

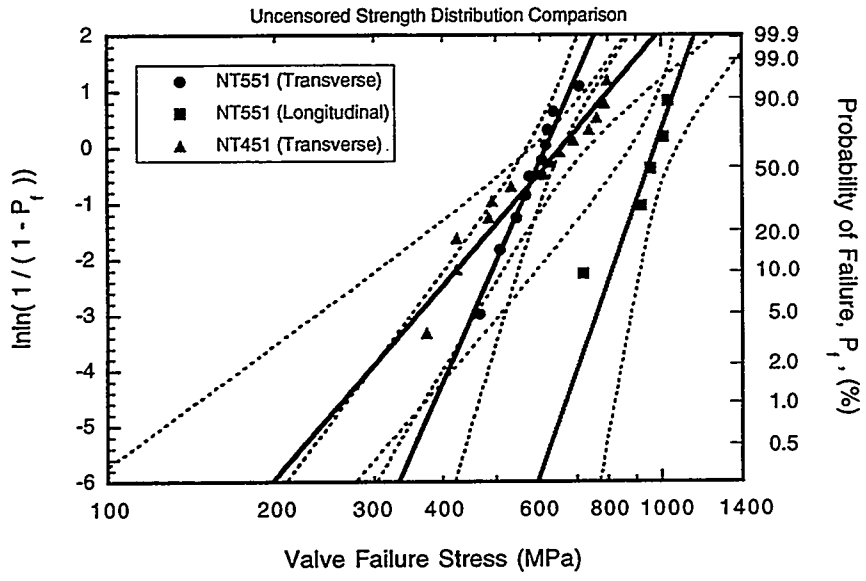

Fig. 1. Comparison of NT451 and NT551 uncensored Weibull valve strength distributions.

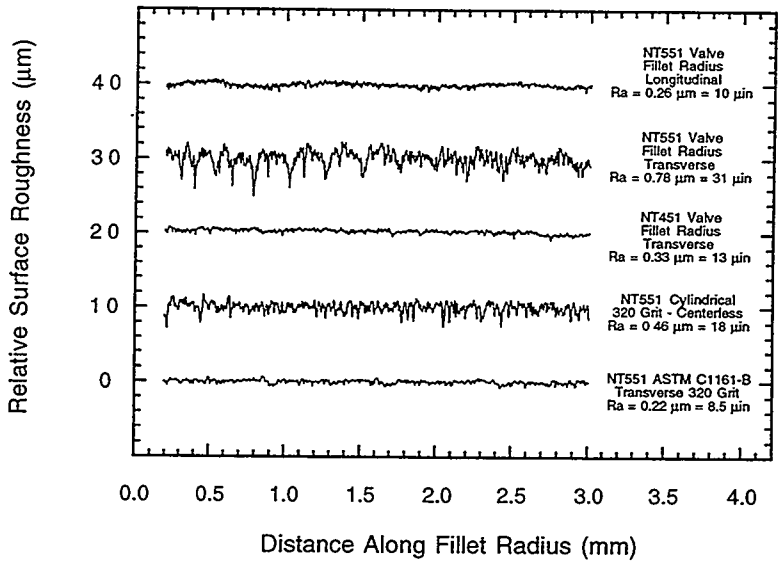

Fig. 2. Comparison of surface roughness profiles measured on the head/stem fillet of NT451 and NT551 valves at the surface location where the maximum tensile exists during testing. These profiles are compared with surface roughness profiles from specimens whose strength distributions are being used in the reliability prediction of these valves.

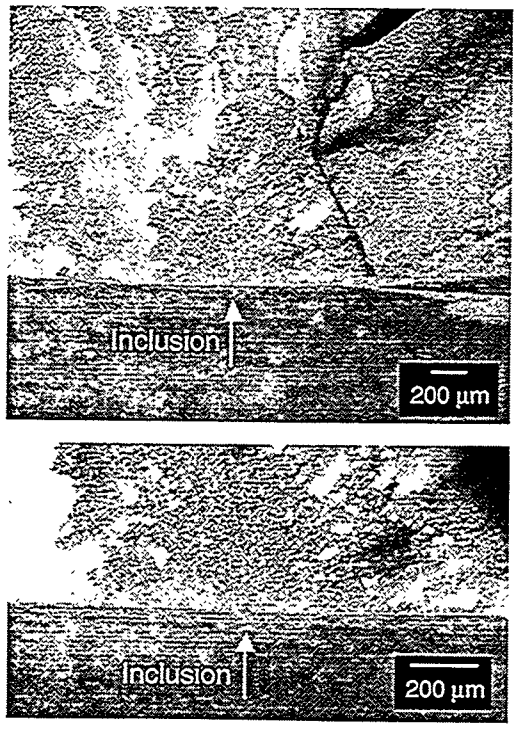

Fig. 3. Examples of flaws that caused fracture in some NT551 valves.

WBS Element 3.1.1.4

Field Emission Analytical Electron Microscopy for Characterization of Catalyst Microstructures

L. F. Allard and T. A. Nolan

OBJECTIVE/SCOPE

The objective of the research is to use analytical and high resolution transmission electron microscopy (TEM) to characterize the microstructures of emission control catalysts. Emphasis is placed on relating microstructural changes to performance of diesel NOx reduction catalysts. The research is focussed on understanding these changes through TEM studies of experimental catalysts materials reacted in an ex-situ catalyst reactor system especially constructed to allow appropriate control of the reaction conditions and the transfer of the sample between reactor and microscope.

TECHNICAL HIGHLIGHTS

We have begun studies of a new series of a series of new catalysts for potential NOx reduction applications, comprising Cu-ZSM-5 zeolite materials doped with La ions, using the Hitachi HF-2000 FE-TEM for high resolution imaging and chemical micro-characterization. This work is being conducted with colleague Dr. Mordecai Sheleff at Ford Research Laboratory in Dearborn, Michigan. The goal of the work is to understand the effects of various steaming treatments on the structure of the catalyst and on the distribution of the active species, copper, and the effects of the tri-valent rare earth species La on resistance to de-alumination under the steaming conditions.

In past work on zeolites, we have confirmed that the specimens are particularly susceptible to damage under the electron beam, and the lattice structure of the material typically degrades within a matter of seconds depending upon total electron dose. In our intial studies, we will not only characterize the general structure of all of the samples received, but will also refine the microscopy techniques in order to preserve as well as possible the atomic structure of the zeolite. We report here some of our initial results of the zeolite studies.

A typical area of a zeolite sample steamed for 4 hr at 400°C is shown in Fig. 1. The particle size is in the 10-30 nm range, and as seen in this image, no lattice fringes are visible due to the rapid damage accrued by the zeolite from the electron beam. At a

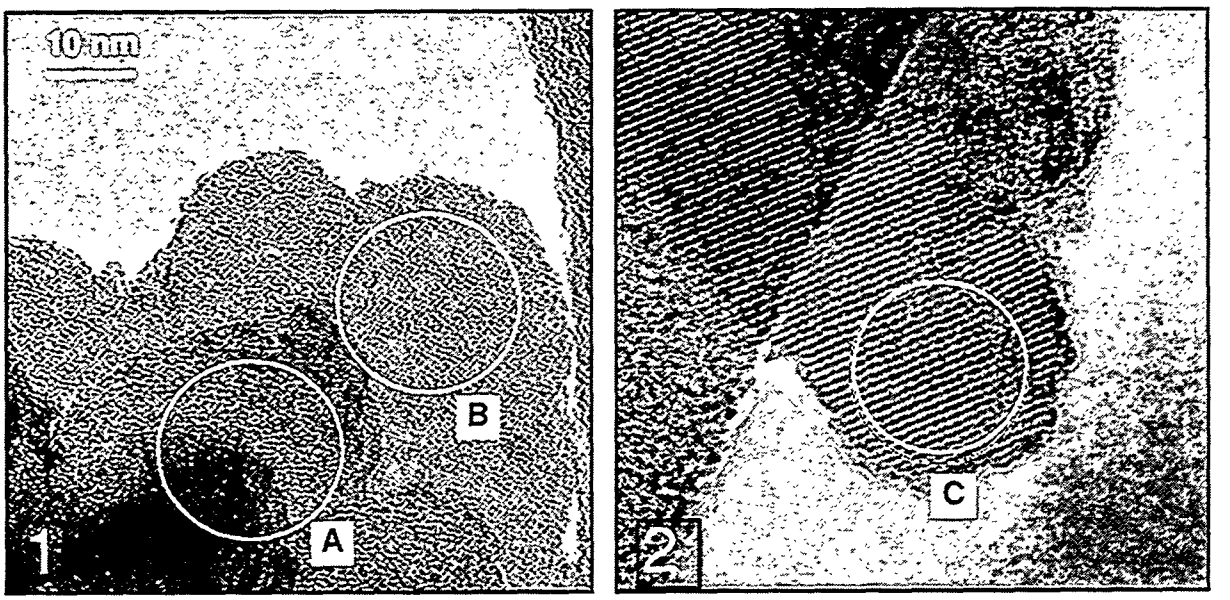

similar magnification in Fig. 2, however, lattice fringes are clearly seen, because the image was set up with the beam off of the area of interest, and the exposure made within a few seconds after bringing the area under the beam. This places a premium on the stability of both the sample and the stage, and does not permit an optimum focus to be carefully set, since this takes significant time and in general cannot be accomplished before the sample becomes irreversibly damaged (i.e. on the order of 10s). The results shown here offer the hope that, with further experience, useful structure images can be accurately recorded.

Energy dispersive x-ray spectra reveal that there is a non-homogeneous distribution of Cu and La in the specimen. A relatively large analysis area was chosen in order to minimize the effects of beam heating or other beam-induced effects on the distribution of elements. The amorphised area A in Fig. 1 showed significantly more La and Cu than either amorphous area B or crystalline area C in Fig. 2. It is recognized that this is a small sample, and that more systematic measurements of many such regions, especially taken over controlled time intervals, should allow a better determination of the effects of beam exposure on the elemental distribution in a given area. From these initial results, however, it does not appear that areas such as Fig. 2 at short beam exposures correlate to high concentrations of either Cu or La, suggesting that minimum beam exposures and short counting times can indeed give a reasonable picture of the elemental distributions in these zeolite specimens.

In order to provide a more realistic test environment for reactions on experimental catalysts for lean NOx applications, the ex-situ reactor system has recently had a number of design upgrades. Thesé are detailed in this report, and examples of the performance are also given. Initial tests on the ex-situ reactor utilized a standard 14%O2 in N2 gas mixture for catalyst reactions, as reported previously. The upgraded system now uses gas mixtures, metered through a programmable controller system, that simulate real diesel exhaust gas compositions. Specialty mixtures were provided by Scott Gases, in two cylinders, one a carrier gas (28%O2 in N2) and the other containing appropriate concentrations of CO, CO2, H, NO, propane, propylene and SO2. The gas flow is controlled by flow metering valves, which are precisely set by the MKS 247 flow controller. The gas compositions were chosen so that a 50-50 mixture would provide the base composition for reactions. Cylinder 1 contained the carrier gas; no oxygen was included in the mixture for Cylinder 2 to eliminate the possibility that the NO component would be oxidized prematurely to NO2. The carrier gas was passed through a water vapor injection system, where the appropriated percentage of water vapor was added to the gas mixture. The gases from both cylinders were combined at the outlet of the water vapor injection system, prior to the input to the reactor. This more realistic gas composition is now being used for catalyst exposures.

MATERIALS AND TESTING STANDARDS

IEA ANNEX II Management (April 1, 1998-September 30, 1998)

M. K. Ferber and K. Breder (Oak Ridge National Laboratory)

Objective/Scope

The purpose of this task is to organize, assist, and facilitate international research cooperation on the characterization of advanced structural ceramic materials. A major objective of this research is the evolution of measurement standards. This task, which is managed in the United States by ORNL, now includes a formal IEA Annex agreement identified as Annex II between the United States, Germany, Sweden, Japan, and Belgium. The original annex included four subtasks: (1) information exchange, (2) ceramic powder characterization, (3) ceramic chemical and physical characterization, and (4) ceramic mechanical property measurements. In the United States, a total of 13 industrial and government laboratories have participated and contributed their resources to this research. The research in Subtasks 2, 3, and 4 is now complete. In 1990, research in two new subtasks was initiated, including Subtask 5, Tensile and Flexural Properties of Ceramics, and Subtask 6, Advanced Ceramic Powder Characterization. The research in Subtasks 5 and 6 was completed in 1993 and the reports were distributed. Two new tasks (Subtask 7 on Ceramic Machining and Subtask 8 on Ceramic Powder Characterization) were proposed in late FY 1993 and the research is completed (1996). Subtask 7 in the United States included eight companies and three federal laboratories. The report on the results from research performed in the United States on Subtask 7 is complete (the final report of all the international research has been published and distributed). Subtask 8 included six companies. The final report for Subtask 8 is complete. In 1996, research in two new subtasks was initiated, including Subtask 9 - Thermal Shock and Subtask 10 - Ceramic Powder Characterization, and work in these subtasks is presently ongoing.

Recent Developments

A Subtask 9 Workshop was held at the Annual American Ceramic Society Meeting in Cincinnati on May 5, 1998. During the Subtask 9 working group meeting, representatives from Japan, Germany, and the United States discussed their thermal shock results obtained for a commercially available silicon nitride disk. In general the preliminary results obtained by the three countries were in fair agreement. The dimensional variations in the specimens were thought to be a primary factor for the relatively large scatter in the measured values of thermal fracture stress.

The IEA Annex II Executive Committee Meeting will be held at Siemens ZT München-Perlach, Germany, October 16, 1998.

Subtask 7, Machining Effects on Strength of Structural Ceramics

The summary report for Subtask 7 of all countries research has been distributed (July 1998). We have requested that the Executive Committee grant permission to distribute this report outside the Annex without waiting until March 1999. As of September 30, 1998, all have granted permission (except we have not heard from Sweden).

Current Subtask 9 Technical Efforts

The verification tests of the centrally-heated thermal shock test to be used in the United States were completed this reporting period. Heating of the specimen is accomplished with a gas torch which is positioned over the cylindrical test specimen using pneumatic actuators. During heating the temperature gradients are measured with an IR camera. Using this arrangement, several silicon nitride disks were fractured and the thermal fracture strength calculated. One limitation of the current setup involves the lack of sufficient temperature resolution. To address this issue a new image analysis system has been procured.

Work related to the automation of the thermal shock apparatus (TSA) developed for use by the United States was continued. Figure 1 provides a schematic representation of the TSA. The two dual-acting air cylinders are used to position the torch over the ceramic disk. The air flow and thus position of the cylinders are controlled with computer activated electric-to-pneumatic transducers. The disk surface temperatures are monitored continuously during heating using an infrared camera (IRC). In the initial TSA, the output of IRC was fed to a conventional VCR. This reduced the effective resolution of the 12 bit camera image to 8 bits, which are standard for commercial VCRs. As a result, the uncertainty in the temperature readings was on the order of ±5°C. In order to utilize the full resolution of the IRC, a computer equipped with a special graphics card was procured from the camera vendor. The software supplied with this computer provides for capturing up to 60 frames per second.

Technical problems with the IR camera has caused delays. The camera has been sent for service and will not be fixed for four months (September 1998).

Subtask 8, Characterizing Ceramic Powders

Major responsibility for this subtask in the United States is at NIST, and a detailed report of progress on this subtask is provided in the section of this report submitted by NIST. Dr. George Onoda has retired and his replacement is Dr. Lin-Sien Lum.

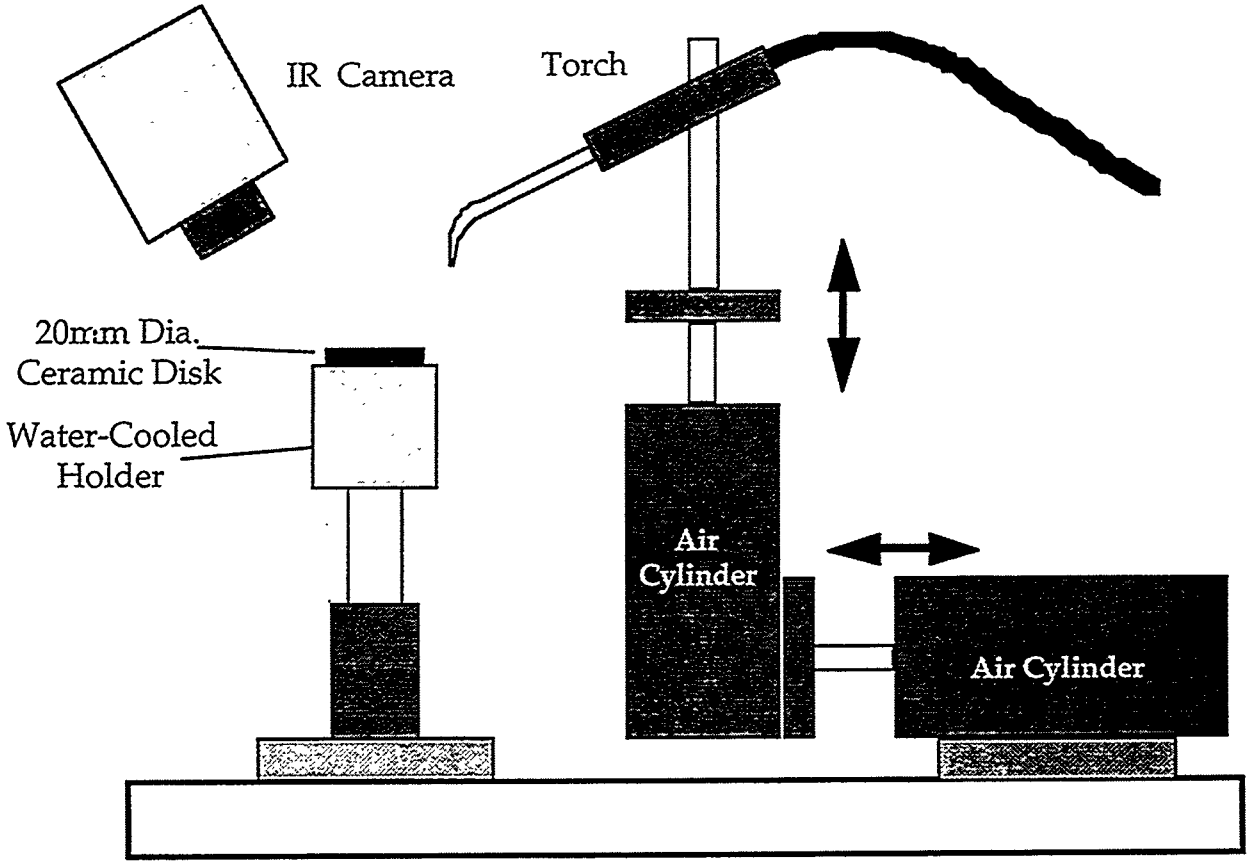

Figure 1 Schematic representation of thermal shock setup.

Status of Milestones - The dates of the remaining Milestones were changed due to delay of the signing of the extension of the Amendment. Milestone 411528 - Testing of Material from each country (Subtask 9) has been deleted due to change in the scope of work.

All Milestones were again changed the end of September (1998) due to technical problems with the IR camera.

411529	Organize data and prepare outline for final reports (Subtask 9 & Subtask 10)	Jun-1-1999 (from Sep-30-1998)
411530	Executive Committee Meeting, Subtasks 9 and 10, in Japan	Completed - 20 Oct. 1997
411531	Publish Thermal Shock (Subtask 9) Final Report	Sep-30-1999 (from Mar-31-1999)
411532	Publish Powder Characterization (Subtask 10) Final Report	Sep-30-1999 (from Mar-31-1999)
411533	Provide reports to ASTM	Sep-30-1999 (from Mar-31-1999)

Communications/Visits/Travel - Kristin Breder and Matt Ferber attended the Annual American Ceramic Society Meeting in Cincinnati, Ohio, on May 3-7, 1998.

Sid Diamond, Department of Energy, Program Review, July 21, 1998

Kristin Breder and Donna Conger visited Debbie Cutler, ETDE Operating Agent Representative, of the Energy Technology Data Exchange (ETDE) Publications Database Office in Oak Ridge, Tennessee, on September 3.

Publications and Presentations - Victor J. Tennery, Kristin Breder, Mattison K. Ferber, and Michael G. Jenkins, "Study of Flexure and Tensile Fracture strength, Fracture Locations, and Monte Carlo Predictions for a Silicon Nitride by Ten U.S. Laboratories," submitted to *J. Amer. Cer. Soc.*, March 1998.

Kristin Breder and Mattison K. Ferber, "Reproducibility of Grinding of Silicon Nitride - an International Comparison," High Temperature Materials Laboratory, Oak Ridge National Laboratory, Oak Ridge, TN, presented at the 100 Annual Meeting of the American Ceramic Society, Cincinnati, OH, May 6, 1998.

Breder, Kristin, Mattison Ferber, Mineo Mizuno, Yasuo Nagano, Thomas Hollstein, Kerstin A. Drusedau, Lennart Carlsson, and Jean-Pierre Erauw, "Effect of Machining Conditions on the Strength of Silicon Nitride Final Report Subtask 7 from Work Performed in Belgium, Germany, Japan, Sweden, and the United States," ORNL/M-6506, prepared by Oak Ridge National Laboratory for the United States Department of Energy, Office of Transportation Technologies, Heavy Vehicle Propulsion System Materials Program, March 1998.

NDE Standards for Advanced Ceramics

R. W. McClung

The development of standards is important for the establishment of reliability and acceptance of advanced structural materials. Committee C-28, on Advanced Ceramics, has been organized in the American Society for Testing and Materials (ASTM) to address this issue. One of the activities of the C-28 committee is nondestructive examination (NDE). The Section C-28.02.02 on NDE is reviewing existing standards on NDE (primarily developed for metals) to determine potential applicability for ceramics, as well as drafting original standards. Use of existing or modified standards, if available, is more efficient that generation of new documents and will assure the input of a large body of NDE expertise. Close liaison has been established with ASTM Committee E-7 on Nondestructive Testing, and documents are in various stages of review, recommendations for change, modification, and balloting. R. W. McClung is a subcommittee chairman in both committees and the official liaison.

Technical Highlights

Liaison and technical support have been continued between ASTM committees C-28 and E-7. To date, forty-four E-7 NDE standards identified as having potential relevance to ceramics have been reviewed in detail with recommendations made to E-7 for modifications to identified documents. Successful action is complete on 39 documents; three are being addressed by E-7; others require action by C-28. C-28 standard, C-1175, the guide to existing NDE standards, currently contains relevant information on 30 standards that were approved for incorporation; one additional standard is being balloted in C-28 for adding to C-1175. A recent revision to standard C-1212 (on fabricating reference specimens with seeded voids) to incorporate improvements from a newly approved standard C-1336 (on fabricating reference specimens with seeded inclusions) received society approval during the last reporting period. An additional set of comments with an affirmative ballot required technical changes. A revision was prepared and successfully balloted in a concurrent subcommittee/committee ballot and has received society approval.

A limited amount of data has been identified for establishing radiographic equivalence factors for advanced ceramics. Additional specimens will be sought for experimental radiography to develop additional data. A volunteer for the radiography has been recognized. The intent of this action is to provide data for a table in an E-7 standard E-94 on the radiographic method. Other work in progress includes an amplified outline for a draft standard for reference specimens containing laser-drilled holes and a possible standard on determination of porosity in ceramics using ultrasonic velocity. In addition, interest has been indicated in potential standards for reference specimens for surface flaws and high-resolution penetrant examination.

An advisory ballot was conducted on two E-7 standards for a potential revision to C-1175, the guide to existing NDE standards applicable to advanced ceramics. The two standards were E-1001, Practice for Evaluation of Discontinuities by the Immersed Pulse-Echo Ultrasonic Method Using Longitudinal Waves, and E-1817, Controlling Quality of

Radiological Examination Using Representative Quality Indicators (RQIs). E-1817 was determined to be applicable to advanced ceramics without revision; E-1001 was determined to be acceptable, in general, but several recommendations were made for modification. A revision to C-1175, incorporating relevant information about E-1817, was prepared and approved for a concurrent subcommittee/committee ballot to be conducted in late 1998. The recommendations for modification to E-1001 were compiled into a proposed revision of the standard in a form suitable for ballot. This was submitted with an explanatory cover letter to the chairman of the ultrasonic subcommittee of committee E-7. (This had been discussed previously with the subcommittee and the chairman during the meetings of E-7 in June 1998 in Atlanta, Georgia.)

A number of new or revised E-7 NDE standards with current or potential relevance to ceramics were reviewed and comments prepared on E-7 committee and subcommittee ballots. The topics included computed radiology (several proposed draft standards), controlling film processing, radioscopy, storage of radiographs and film, determining contrast sensitivity in radioscopy, determining relative image quality response of industrial radiographic film, resonance ultrasonic spectroscopy for flaw detecting, new terminology for radiology, and a revision to a standard on characterizing ultrasonic instrumentation (currently incorporated in C-1175). Another revision to a standard on computed tomography was prepared in response to prior comments from Committee C-28. The latter CT standard has been recently approved for incorporation into C-1175.

During meetings of Committee E-7 in Atlanta, Georgia, June 14-18,1998 (immediately prior to and overlapping meetings of C-28), participation by McClung as C-28 liaison included meetings of the subcommittees on radiology and ultrasonics. He reported to the respective subcommittees about the advisory ballot on E-1817 and E-1001 and the planned action noted above. Significant activity is ongoing in both subcommittees that will result in standards of interest and value for advanced ceramics. Several of the revisions and ballots are based, in part, on requests from C-28. Radiological standards in various stages of drafting, revisions or balloting include standards for image quality response of film at low (X-ray) energies, a guide for controlling film processing, total image unsharpness in radiology, computed radiology, a guide to radiographic examination, storage of radiographs and film, and determining image quality response of radiographic film. Several standards (from E-7) on computed tomography are being considered by the international committee ISO TC-135 on NDE.

Subcommittee E7.06 on Ultrasonic Methods has many standards in different stages of preparation or ballot including responses to requests from C-18. Among ultrasonic standards in process relevant to advanced ceramics are those for resonant ultrasonic spectroscopy (currently used for ceramic bearings and other materials), evaluation of flaws by immersed techniques, characterization of instruments and search units, detection and evaluation of flaws by contact techniques (three standards), and a practice for immersed examination. Several ultrasonic standards have been or are being presented to (and adopted by) the international Committee ISO TC-135 on Nondestructive Testing.

In a June 1998 meeting of the C-28 Long Range Planing Committee, a preliminary response to a survey on C-28 standards expressed interest in potential standards for NDE of coatings and green ceramics. After all results from the survey have been received and tabulated, they will be distributed to the relevant subcommittees of C-28 for action.

In July, administrative approval was obtained for an advisory ballot (opinion poll) of committee C-28 on the desirability (need) for adding relevant information on acoustic emission (AE) standards to C-1175 which currently contains information about materials, equipment and procedures for radiology, ultrasonics, and liquid penetrant examination. Suggested AE standards include those for primary and secondary calibration of sensors, monitoring during controlled stimulation, characterizing AE instrumentation, determining the reproducibility of AE sensor response, and mounting of AE sensors. A letter of explanation and ballot form were prepared and submitted to ASTM for distribution. The ballot is in progress, and responses received to date indicate a recommendation for incorporation of AE into C-1175. If the final results are affirmative, an advisory ballot will be initiated to provide review of selected AE standards to determine applicability to advanced ceramics (or recommended modifications to the standards to make them applicable).

Semiannual Report (March – September 1998)
IEA Subtask 10
George Onoda and Lin-Sien Lum
National Institute of Standards and Technology
Bldg 223, Room A256, Div. 852
Gaithersburg, MD 20899

Objective/Scope

The objective of Subtask 10 is to tighten and finalize procedures for the characterization of secondary properties of powders. There are four focus areas relating to the secondary properties: dispersion of powders for slurry preparation, slurry preparation, spray dried powders and green body evaluation.

Subtask 10 will involve participants from Belgium, Germany, Japan, Sweden, and the United States. Thirty-two participants from the five countries will participate in the round robin.

Technical Progress

A method to determine the state of dispersion of ceramic powders has been developed. The method involves following the changes in the particle size distribution as a function of the ultrasonication time used to disperse the powder in dilute suspension. If deagglomeration occurs by ultrasonication, then the particle size distribution should shift toward the finer size as the ultrasonication is increase. The final dispersed state is the size distribution that is attained after no further changes in particle size distribution occurs with longer ultrasonication time.

Measurement procedures have been developed to determine the rheology of ceramic suspensions using a rotational viscometer and a rotational rheometer. The suspensions in these procedures have a solids volume fraction of 30 percent of powder. The procedure specify the measurement of apparent viscosity, shear-thinning index and thixotropic response in water-based ceramic powders slurries over a shear rate range roughly 1 s^{-1} to 500 s^{-1}.

Procedures have been developed to determine the flow rate, size distribution, moisture content and binder content of spray dried powders. The procedure for flow rate measurement uses a modified Hall Flow method. A dry sieving technique is used to measure the size distribution of the granules. The moisture and binder content is determined by measuring the weight loss of the powders after drying.

Procedures to determine bulk density, porosity measurements and tensile strength on green body compacts have been developed. The bulk density is determined by measuring the external dimensions and the weight of the compacts. A mercury porosimetry technique is used to determine the porosity of the compacts. The tensile strength of the green body compacts is measured by the diametral compression test. The test consists in compressing a cylindrical specimen diametrically between two flat platens of a universal testing machine.

Each of the measurement procedures passed through rigorous robustness testing to tighten the experimental parameters. The technical leaders before compilation and distribution to the participants reviewed the finalized procedures. Corrections and editions have been incorporated into the final procedures. To improve the quality of the spray dried powders used for Subtask 10, commercial sources of the powders were utilized to eliminate problem associated with pilot size spray dryers. The spray dried samples for the round robin are being prepared for distribution to the participants. The green body characterization pellets are in the process of fabrication by VITO in Belgium from similar spray dried powders for density, porosity and tensile strength measurements.

Milestones
Prepare and distribute samples to participants by NIST for round robin testing—12/98
Complete round robin testing—2/98
Data analysis and final report—3/98

Communications/Visits/Travel- The technical leaders met in Cincinnati, Ohio in May 1998.

Publications/Presentations – none

Reference - none

Problems Encountered - none

Ceramic Mechanical Property Test Method Development

George D. Quinn
(National Institute of Standards and Technology)

Objective/Scope

This task is to develop mechanical test method standards in support of the Propulsion Systems Materials Program. The test methods should meet the needs of the DOE engine community but should also consider the general USA structural ceramics community as well as foreign laboratories and companies. Draft recommendations for practices or procedures shall be developed based upon the needs identified above and circulated within the DOE ceramics engine community for review and modification. Round-robins will be conducted as necessary, but shall be well-focussed, limited in scope, and complementary to IEA round-robins. Procedures developed in this program will be standardized by ASTM and/or ISO.

Technical Highlights and Results

1. Summary

Work continues on developing a full-consensus fracture toughness standard in ASTM to supersede the provisional standard PS 070-97. The surface crack in flexure SCF test method, one of the three in the standard, was further refined by using dye penetrants to make the cracks easier to detect and measure. Preparation of a reference material with certified fracture toughness continues at NIST as a separate project.

ASTM standard are being carried over to international standards in International Standards Organization (ISO), Technical Committee TC 206. Two draft ISO flexure strength standards have been written. We also are cooperating in the creation of a world ISO standard for Vickers and Knoop hardness and we are pleased to note that it conforms in most details to the ASTM methods. Two ISO standards on fracture toughness are under development. We have started to rely on results of several International Energy Agency (IEA) or Versailles Advanced Materials and Standards (VAMAS) round robins to support the USA position in ISO TC 206.

Research investigations on the diametral compression test method are on hold pending further analysis of the fracture patterns in specimens tested in the last semiannual period.

A task to develop methods for the flexural strength testing of cylindrical specimens has begun.

We currently are working on the following formal draft standards:

1.	ISO DIS 14704	Advanced (Fine) Ceramics - Determination of Flexural Strength at Room Temperature (NIST-USA convenes)
2.	ISO CD 14705	Fine Ceramics (Advanced Ceramics, Advanced Technical Ceramics) - Test Method for Hardness for Monolithic Ceramics at Room Temperature (Convened by Japan, NIST represents the USA)
3.	ISO Draft	Advanced (Fine) Ceramics - Determination of Flexural Strength at Elevated Temperature (NIST-USA convenes)
4.	ISO WD 15732	Fine Ceramics (Advanced Ceramics, Advanced Technical Ceramics) - Determination of Fracture Toughness at Ambient Temperature by Single Edge Precracked Beam (SEPB) Method (Convened by Japan, NIST cooperates with ASTM Task Group for USA response)
5.	ISO draft	Fine (Advanced) Ceramics - Determination of Fracture Toughness at Room Temperature by the Surface Crack in Flexure (SCF) Method (Proposed by USA-NIST)

Earlier work in this project has contributed to **eleven** completed standards:

1. ASTM C 1161-90 Standard Test Method for Flexural Strength of Advanced Ceramics at Ambient Temperature, G. Quinn, NIST.
2. ASTM C 1198-91 Dynamic Young's Modulus, Shear Modulus, and Poisson's Ratio for Advanced Ceramics by Sonic Resonance, by S. Gonczy, Allied-Signal; G. Quinn, NIST; and J. Helfinstine, Corning.
3. ASTM C 1211-92 Standard Test Method for Flexural Strength of Advanced Ceramic at Elevated Temperature, by G. Quinn with help from Mr. M. Foley, Norton; Mr. T. Richerson, Allied-Signal; and Dr. M. Ferber, ORNL.
4. MIL HDBK 790 Fractography and Characterization of Fracture Origins in Advanced Structural Ceramics, with J. Swab and M. Slavin, U.S. ARL.
5. ASTM C 1239-94 Standard Practice for Reporting Strength Data and Estimating Weibull Distribution Parameters, by S. Duffy, NASA-Lewis; G. Quinn, NIST; and C. Johnson, G.E.
6. ASTM C 1322-96 Standard Practice for Fractography and Characterization of Fracture Origins in Advanced Ceramics, in cooperation with Mr. J. Swab, U.S. ARL.
7. ASTM C 1326-96 Standard Test Method for Knoop Indentation Hardness of Advanced Ceramics.
8. ASTM C 1327-96 Standard Test Method for Vickers Indentation Hardness of Advanced Ceramics.
9. ASTM PS 070-97 Standard Test Methods for the Determination of Fracture Toughness of Advanced Ceramics, in cooperation with Prof. I. Bar-On, WPI; Prof. M. Jenkins, Univ. Washington, and J. Salem, NASA-Lewis.
10. ASTM E-1875-98 Standard Test Method for Dynamic Young's Modulus, Shear Modulus, and Poisson's Ratio by Sonic Resonance
11. ASTM E-1876-98 Standard Test Method for Dynamic Young's Modulus, Shear Modulus, and Poisson's Ratio by Impulse Excitation

The last two are recent additions and are standards created in ASTM Committee E-28, Mechanical Testing. That Committee, in consultation with Committee C-28 Advanced Ceramics and NIST, copied two C-28 standards (C 1198 and C 1259) almost verbatim. It was felt that the C-28 standards were so well written and generic that they need not be confined to advanced ceramics, but may now be applied to all elastic materials.

2. Fracture Toughness

2a. ASTM Standard - Refine PS 070

The ASTM standard continues to be revised and refined as it wends its way through the process of being adopted as a full consensus standard. In the meantime we have announced the new provisional standard in a series of lectures and presentations. It is important that the ceramic and engineering community become cognizant of the standard and start to use it. Interest is high. At the Cocoa Beach January, 1998 American Ceramic Society conference, an invited lecture was made before a packed audience. A dozen reprints were quickly snapped up and 15 more copies of the paper and the provisional standard had to be mailed from NIST upon our return. A presentation in Korea in September had over 100 in attendance.

Two negatives and several affirmatives with comments that were received on the Spring ASTM C-28 ballot were reviewed at the C-28 meeting in Atlanta in June. A revised draft is being prepared for a Fall 1998 ballot. Major changes to the chevron notch equations have been made by M. Jenkins and J. Salem. Their analytical work had showed that the traditional slice model for the stress intensity shape factors may have been less accurate than a straight through crack assumption model for 3 of the 4 chevron geometries in the standard. Subsequent testing with prototype NIST standard reference fracture toughness specimens confirmed that more accurate answers indeed were obtained with the latter model for one of the chevron geometries. This underscores the value of having a reference material for which there is a high confidence in fracture toughness values. A joint paper on this topic is in preparation with Jon Salem.

One of the balloters raised an issue about the single-edged precracked beam (SEPB) being too restrictive in some respects. We subsequently decided to broaden the allowable precrack depth (alpha) range from 0.40-0.60 to 0.35-0.60. This will allow more specimens and experiments to be declared valid. Cracks longer than 0.6 cause the calculated toughness to be too sensitive to the crack size measurement. We decided not to extend the range down to 0.30, as is specified in the Japanese standard JIS R 1607, since there is compelling evidence that indentation residual stresses may affect the final result.

We also relaxed the allowable crack tilt angle from 5° to 10° for 4-point flexure loading. It shall remain at 5° for 3-point loading. There is a growing body of evidence that 4-point loading may be preferable to 3-point loading in the SEPB tests, particularly at small fixture span sizes. The smallest span allowed in the standard is 16 mm, and it is very difficult to line up the precrack with the middle loading roller. The tolerance is 0.5 mm, but evidence suggests that a tilted crack may induce error. Prior work in a 1991 VAMAS round robin wherein we had to center a precracked specimen on a 16 mm span three point fixture also exposed this difficulty. Any misalignment of the precrack in three point loading causes the fast fracture portion of the crack to veer off, often at an unacceptable angle ($>5°$), thereby making the test invalid. The 4-point configuration is far less sensitive to crack tilt.

Serious consideration was also made to dropping the very small span 3-point SEPB configuration, so we did some testing to compare short span fixture results to full-sized fixture results. Once again, the reference material was very handy. We took broken halves of 3 mm x 4 mm x 45 mm SCF and SEPB test specimens and used them for mini SEPB (3 x 4 x 25 mm) tests in both 3-point loading (20 mm span) and 4-point loading (10 x 20 mm). The new results are shown in the last two rows of Table 1.

Table 1
Comparative fracture toughness results for specimens from billet C of the Standard Reference Material

Method	# of specimens	Average, K_{Ic}, MPa$\sqrt{m}$	Std. Dev. MPa$\sqrt{m}$
SCF, full sized specimens, four point	26	4.58	0.16
CNB, full sized "A" specimens, four point*	8	4.60	0.13
SEPB, full sized specimens, four point	11	4.59	0.12
SEPB, mini specimens, four point	5	4.56	0.13
SEPB, mini specimens, three point	3 of 5 successful only	4.55	0.09

* Tested by J. Salem, NASA, Lewis

The results are in superb agreement and confirm that the mini SEPB specimens produce the same accuracy and precision as the full-sized counterparts. Additional data from another billet corroborate this conclusion. Consequently, we have expanded the utility of a single specimen which may now be used to produce three fracture toughness tests which should be appreciated by the user community.

The small span 3-point experiments were problematic, however. The specimens were difficult to line up and 2 of the 5 trials were invalid since the crack angle was greater than 5°. The apparent toughnesses of the two faulty specimens were obviously erroneous as well: 4.96 and 5.28 MPa$\sqrt{m}$.

A recent VAMAS round robin on the fracture toughness of ceramic whisker-reinforced composites encountered exactly the same problem with short span 3-point SEPB testing.

Why keep the three point configuration? Some users prefer the illusory simplicity of the method. We decided to keep it in the standard for the time being because it is a traditional configuration (albeit scaled down in size) used in metals fracture toughness standards such as E 399, and it is the primary configuration in the Japanese fracture toughness standard JIS R 1607.

It was suggested that the ASTM standard be further modified to include explicit mention of the new standard reference material SRM 2100. After some discussion amongst the task group members we agreed to defer this for the moment. We want to get the current version adopted as a full standard as soon as possible and do not wish to include any new elements may elicit further delaying negative ballots.

2b. Standard Reference Material for Fracture Toughness

The NIST work to create a Standard Reference Material for fracture toughness is nearly finished. The data base for this SRM has expanded to 205 experiments on specimens taken from 6 billets of NC 132 hot pressed silicon nitride continues. This data base is supported by 85 preliminary tests on other NC 132 billets and over 200 specimens tested in the 1994 VAMAS round robin on the surface crack in flexure test method. All told, 290 specimens have been tested at NIST and about 200 by other labs as part of the preliminary or final SRM work. These ~500 experiments will support the nearly 800 specimens we hope to have available for sale as SRM 2100.

Unfortunately, some inhomogeneities were detected in specimens from 2 billets. The specimens had a faint mottling pattern on the surface similar to patterns shown in a 1989 paper by David Clarke in the identical material.[1] These specimens also had larger fracture toughness variability than normal. This was disconcerting and this project is on hold until October and November pending a resolution of this problem. An x-ray fluorescence chemical analysis revealed excess concentration of aluminum in the specimens. Aluminum is typically present at a level of a few tenths of weight percent, but the questionable billet had concentrations much greater than this.

A small additional set of specimens was prepared from billet H, a billet unlike the other 5 billets in that its specimens were sensitive to slow crack growth (SCG) at room temperature. The SCG effects were discernable in both SEPB and SCF experiments. We are preparing a few chevron notch (CN) specimens to give to Jon Salem at NASA-Lewis to test. Our objective is to ascertain whether the SCG can affect CNB tests in a manner similar to SCF and SEPB tests.

2c. Fluorescent dye penetrant - SCF Test method

Dye penetration techniques were applied to SCF precracks with the objective of making this test method (one of the three in the ASTM standard) easier to conduct. In this semiannual period, we applied the techniques to alumina, silicon nitride, and silicon carbide.

We compared the performance of two level IV, ultra-high sensitivity fluorescent penetrants: Magnaflux grade ZL-37 and Sherwin RC 88. Both are oil based. We wished to avoid possible SCG effects from water-based penetrants. Alumina, Coors AD 999 and silicon nitride, ESK Ekasin hipped specimens were tested with both penetrants. We also tried the ZL-37 on two Carborundum sintered

alpha silicon carbide specimens and four Norton hot-pressed silicon carbide specimens.

Good results were obtained with both penetrants. ZL-37 was less viscous than RC 88, seemed to be brighter to the eye when first viewing the precracks, and was less messy. Consequently, in the future we will use primarily the ZL-37. Magnaflux ZL-37 is a common ultra-high sensitivity penetrant that has been used effectively in other DOE ceramic programs. Vimal Pujari used it at Norton in 1993 to study surface cracks in silicon nitrides. Forster and Ellingson studied it as a complementary method to their more sophisticated NDE procedures and published a report on dye penetration procedures in 1996.[2]

Our new procedure is to apply the dye penetrant while the SCF precracked specimen is loaded to about half the expected fracture load for a soak period of about 10-15 minutes. When the specimen is unloaded the crack closes and tends to squeeze the dye both out of the crack and up further into the crack. The specimen is then hand ground as usual to remove the residual stresses. The specimen is fractured in four-point flexure and then immediately (within 1 hour) examined in a metallographic microscope. Common black lamp UV lamps are inadequate to illuminate small cracks, so we used a Leica DM-RM metallographic microscope that has an intense xenon lamp source with built-in UV filters. The fluorescent penetrant was easy to detect through the microscope eyepieces and correlated very well with crack sizes measured by optical or SEM fractographic techniques. It was a little difficult to photograph the precracks, however. We used Polaroid type 57 film which has an ASA speed of 3000 but exposure times as long as 15 minutes were necessary. The dye faded with exposure to the UV light source. A second photograph taken under the same conditions needed as much as double the exposure time. Our best measurement procedure was to mark the photographs (for the crack size measurement) while glancing at the specimen through the microscope to help aid in the interpretation.

Experiments with the alumina, silicon nitride and sintered alpha silicon carbide were successful, but we were unable to obtain dye penetration with the fine-grained, hot-pressed silicon carbide, Grade NC 203. We used our best procedure with ZL-37 and were disappointed when the dye failed to penetrate. We suspect that the dye penetrant is better able to infiltrate coarse-grained materials than fine-grained materials. Despite this setback, ordinary fractographic means were very successful in evaluating the crack size and we were able to obtain excellent fracture toughness results for the NC 203 as shown in Table 2. The 8 valid tests represented a 100% success rate, in contrast with our earlier work on this material in October 1994 when we obtained only 2 valid tests of 5 specimens tested for an average of 4.16 $\pm$ 0.08 MPa$\sqrt{m}$. The polishing work to remove the indentation and its residual stress damage zone were done more carefully this time.

Table 2
Fracture Toughness of Norton hot-pressed silicon carbide by the SCF method, 5 kgf (49 N) Knoop indentation load

number of specimens	crack size depth x width, μm	Average, K_{Ic} MPa$\sqrt{m}$	Standard deviation MPa$\sqrt{m}$
8	110 x 260	3.90	0.10

During a visit to Oak Ridge in May, we discussed some of the fluorescent dye penetration results with Dr. K. Breder who subsequently sent us some new GS-44 specimens to try. This material was used in the IEA project to assess machining damage. Detecting machining damage by fractography was difficult. By trying our fluorescent penetration method on SCF precracked specimens, we may pave the way for application of dye penetration methods to help characterize machining damage. The specimens Kristin sent us were too large for the SCF method and the specimens were sent to Bomas to be cut into 2 or 3 specimens per slab. (Too much hand polishing would have been required to remove the indentations.) This work is expected to commence at NIST in November.

3. ISO Flexure Strength Standards

Draft flexure strength standards for both room temperature and elevated temperature were reviewed and presented at the ISO Technical Committee TC 206 meeting in Kyongju, Korea on September 23-25. The room temperature draft has reached the level of "Draft International Standard." Both documents are harmonious with the ASTM C-28 standards (C 1161 and C 1211) but also include some elements from the Japanese preferred testing configurations. We insist, however that the ISO standard use rolling (friction relieving) loading pins and include both semi-articulating and fully-articulating fixtures. The ASTM standard also allows testing as-fired specimens. These provisions from the ASTM standards have met considerable resistance from the Japanese delegation which prefers simpler fixture styles. Indeed, at the meeting of TC 206 in Korea, the Japanese delegation insisted that we furnish evidence that elevated temperature flexure testing can be done with fully-articulating fixtures. Mr. Quinn responded by showing several fully-articulated fixture designs in use around the world. Furthermore, some results from *International Energy Agency project, subtask* 5, elevated temperature flexure strength were presented wherein some of the USA participants used fully-articulating fixtures. The German participants probably all used fully-articulating fixtures, but this needs to be verified. *The IEA round robin results were extremely helpful in advancing the USA position and supporting ASTM standards.*

The Korean delegation reported some interesting new experiments that reveal that humidity is a major factor for room temperature strength for some materials. The current ASTM standard C 1161, the other national standards, and the draft ISO standard all concur on this matter and merely require that humidity be measured and reported. This may not be sufficient.

4. Flexure Strength at Room Temperature - New Fixture Design

A new set of semiarticulating flexure fixtures for room temperature testing of rectangular specimens has been designed. Through the years we have used the traditional semi articulating fixture (with the ball) for well-machined specimens. For less well prepared or as-fired specimens, we used the patented U.S. government four-point fixture. The latter proved to be easier to use and it was felt that a new semiarticulating design could be made with the best elements of both fixture designs. We also wished to eliminate the ball from the semiarticulating design. A new set of fixtures was designed and experiments conducted to evaluate it's suitability. AD-999 alumina specimens left over from the TTCP round robin of the mid-1980's were tested. Fractures were uniformly distributed in the gage section and the strength values agreed with the earlier data. A single experiment with a strain gaged specimen was conducted and the observed strain was within 1/2% of the theoretical amount. The fixture design will be included in a future semiannual report.

Figure 1 Scheme for Flexure Testing of Cylindrical Specimens

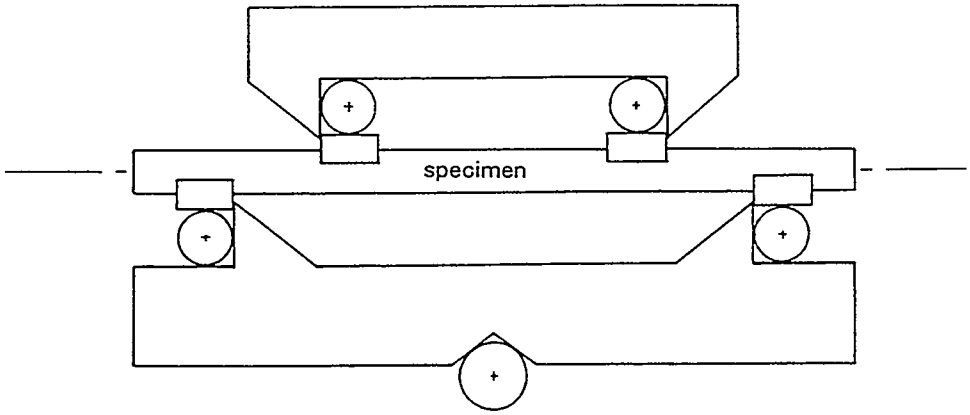

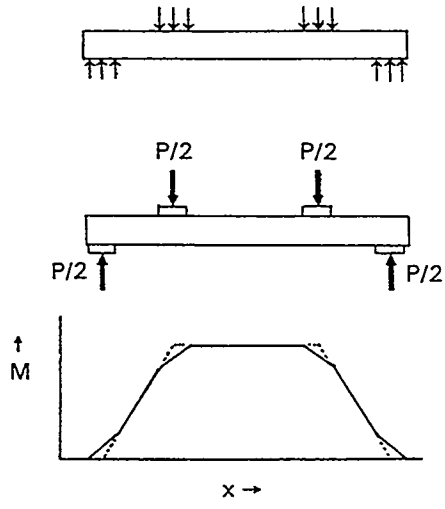

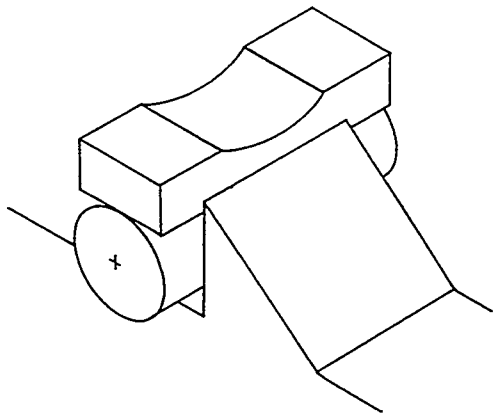

$$\sigma = \frac{M\,c}{I}$$

5. Diametral Compression

No activity this period. This work is on hold pending further intensive fractographic analysis to determine why our earlier test specimens did not fracture from volume flaws in the middle of the specimens. A german report from the Fraunhofer Institute in Freiburg must be translated and read as well since it has important new information about this test method. We remain optimistic that this method can be refined and made into a user friendly, standardized test.

6. Flexure Testing of Cylindrical Ceramic Specimens

During Mr. Quinn's visit to Oak Ridge National labs in May, it was learned there is common interest in adapting flexure strength test methods to cylindrical specimens. Some preliminary work had already been started at NIST on this topic. Tom Yonushonis at Cummins has also expressed an interest.

Articulation is less of a problem with cylindrical specimens, but avoidance of high contact stresses is a problem. Loading rollers should not apply load directly to the test specimen since the localized contact stresses between two crossed rollers is excessive. A scheme using loading shoes (or cradles) as illustrated in Figure 1 therefore has been selected.

The loading shoes transmit the forces from conventional rollers to a distributed area (if the shoe has a contour to match the specimen) or distributed line contacts (if the shoe has V-grooves). Although the load is no longer applied directly at one point, the specimen stress distribution is hardly affected. The distributed loads create the identical moment (load times distance) loading on the specimen gage section. The stress distribution is altered in the immediate vicinity of the loading shoes, but in a conservative manner as illustrated in the insert of Figure 1. There are no severe stress concentrations.

A fixture has been fabricated (Figure 2) and preliminary testing completed on sintered alumina, glass, and silicon nitride specimens. The fixture is intended to be used on 6 mm diameter x 80+ mm long specimens. One advantage of the design is that the fixture can also be used to test rectangular specimens merely by removing the shoes. The rectangular specimens may be placed directly on the loading rollers.

Figure 2 Flexure Fixture For Cylindrical Specimens with a Glass Specimen

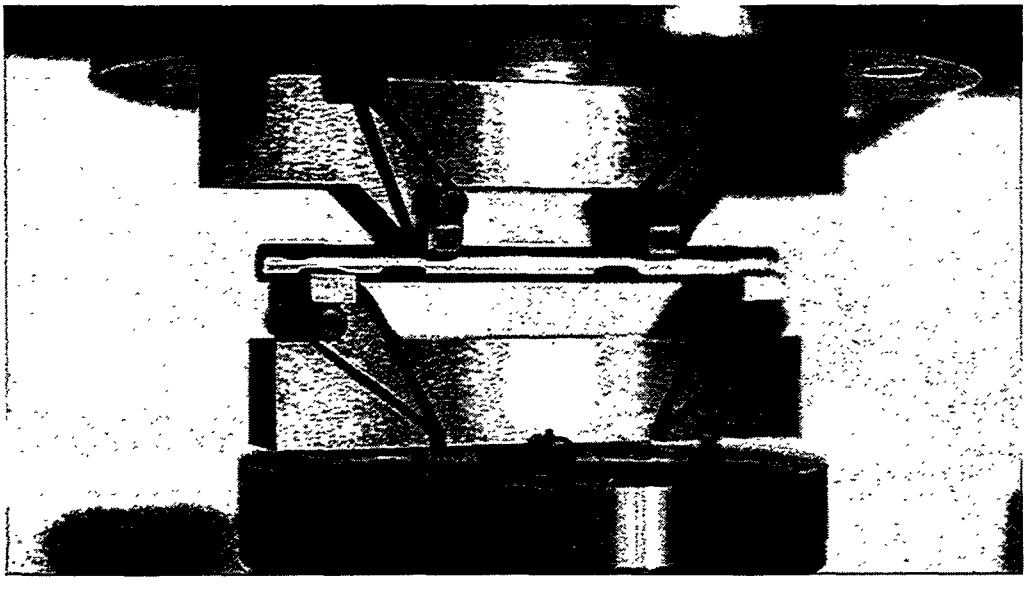

Figure 3 Flexure strength of a Cylinder-Segment after Weiler.[2]

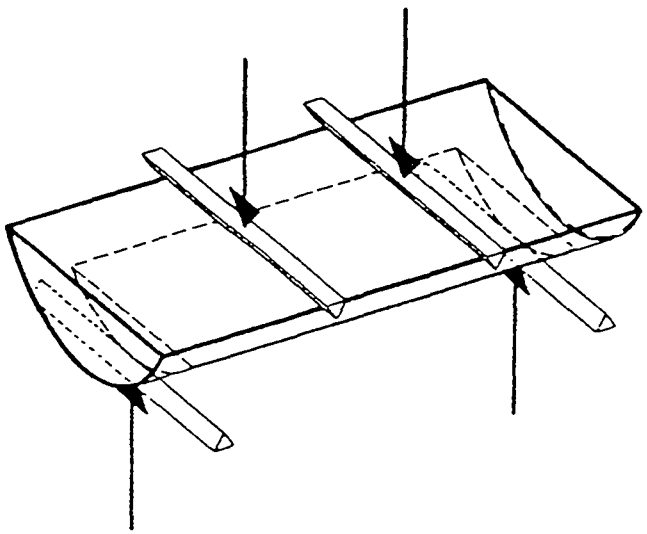

In an alternative approach, a few Coors zirconia timing plungers have been cut in half and will be tested in flexure in late 1998 using a method first suggested by L. Weiler of Asea/Brown/Boveri.[3]

7. Other Activities

7a. Possible Surface Roughness Round Robin

A new VAMAS round robin on surface roughness characterization by diamond stylus profilometry has been proposed by the National Physical Laboratory, England. The round robin will feature conventional roughness measurements of as-sintered, ground and polished components. Kristin Breder at ORNL was contacted and agreed to participate. NIST will also participate. Other interested DOE parties are welcome to join this project. Please contact George Quinn at NIST for further information (301 975-5765).

7b. Possible Ceramic Material Specification Standards

At Ray Johnson's suggestion, Cummins, Detroit Diesel Corporation and Caterpillar Companies were contacted to ascertain whether the companies were interested in ceramic material specifications standards. There are ASTM materials specifications standards for alumina substrates, alumina or zirconia biological prostheses. Is the time right for a "silicon nitride for engine applications" specification? As in 1994, when we made a similar investigation, we again received mixed answers and concluded that the market was not ready for such a specification.

7c. Fractographic Webb Site

NIST finished the installation of the new NIST webb site for fractographic analysis of advanced ceramics. The webb site, which is in essence a skeletal version of ASTM standard C 1322, is:

http://www.ceramics.nist.gov/webbook/fracture/fracture.htm

7d. ISO Test Method Standards

Mr. Quinn represented the United States at the ISO TC 206, Fine Ceramics, meeting in Kyongju, Korea on the following Working Groups:

- WG 2 Room Temperature Flexure Strength, Overall Convener
- WG 3 Hardness, USA representative
- WG 6 Tension Strength, Monolithics, represented the USA on behalf of Mike Jenkins
- WG 7 Fracture Toughness by SEPB, represented the USA on behalf of the ASTM Task Group
- WG 8 Elevated Temperature Flexure Strength, Overall Convener
- WG 9 Tensile Behavior, Composites, Led this WG on behalf of Mike Jenkins, the Overall Convener
- WG 10 Elastic Modulus, Represented the USA on behalf of Steven Gonczy, the USA representative
- WG 11 Weibull Analysis, Led this WG on behalf of Steven Duffy, the Overall Convener
- NWI Fracture Toughness by the SCF Method, Overall Convener

The last is a "New Work Item", which is the precursor stage to a Working Group. In each instance, Mr. Quinn had to review the USA standards, coordinate with the USA representatives in ASTM Committee C-28, and represent the USA position at the meeting.

Prior International Energy Agency round robin results were very helpful in supporting the USA position in WG 6, tension testing, and WG 8, elevated temperature flexure strength. (Furthermore, although not covered in this task, IEA activities on powder characterization have aided our international standards work in WG 5, Specific Surface Area of Powders by Gas Absorption methods.)

Status of Milestones

Revised Milestones Schedule, prepared 10/98

412125	Prepare draft ISO Flexure Strength Standard	completed Apr. 1996
412126	Prepare and distribute to ASTM Committee C-28 members a simple statistical analysis package for interlaboratory round robin test data.	completed June 1996 completed
412127	Participate in a ceramic whisker-reinforced composite round robin	completed May 1996
412128	Conduct dye-penetrant experiments on scf fracture toughness specimens	completed June 1998
412130	Finish ASTM fracture toughness standard (PS-070-97)	completed Mar. 1997
412131	Complete Phase I diametral compression testing	completed Dec. 1997
412135	Participate in VAMAS SEVNB fracture toughness round robin	completed Oct. 1997
412136	Finish of NC 132 fracture toughness measurements to assess 4 billets suitability as K_{Ic} reference material	completed July 1998
412137	Conduct survey of interest in a hypothetical silicon nitride engine material specification	completed Mar. 1998
412124	Prepare comprehensive paper on hardness testing of ceramics Delay until SRM 2831, Vickers hardness of Ceramics is complete.	**Reschedule to** June 1999
412129	Write comprehensive report on fracture evaluation by SCF method	**Reschedule to** Mar. 1999
412132	Commence diametral compression round robin This milestone should be canceled until test	**Cancel**

	methodology problems have been resolved.		
412133	Prepare draft diametral compression standard for ASTM This milestone should be canceled until test methodology problems have been resolved.	**Cancel**	
412134	Prepare review paper on diametral compression method	**New date**	Sept. 1998

Problems encountered

A guest scientist Dr. Ken Xu, who had been doing many of the fracture toughness experiments, left NIST to take a full time job at the end of July. This will slow our laboratory testing work.

A new phase of diametral compression testing and analysis is needed to follow on the unsatisfactory outcomes of our work in the fall of 1997 and winter of 1997/1998.

Publications/Presentations

1. C. Ullner and G. D. Quinn, "Round Robin on Recording Hardness," VAMAS Report #33, BAM, Berlin, February 1998.
2. G. D. Quinn, "Hardness Testing of Ceramics," Advanced Materials and Processes, August 1998, pp. 23 - 27.
3. G. D. Quinn, M. Jenkins, J. Salem, and I. Bar-On, "Standardization of Fracture Toughness Testing of Ceramics in the United States," proceedings of the 3rd PAC RIM conference, Kyongju, Korea, September 21, 1998.

Communications/Visits

1. G. Quinn attended the ASTM C-28 meeting in Atlanta in June.
2. G. Quinn visited ORNL on May 28.
3. Several inquiries from Cummins engine company about flexure fixture design and testing were answered. A set of drawings for a semiarticulated type II fixture were sent to Cummins and are being used to fabricate a fixture set.
   Note: Flexure fixture design drawings and simple users guides are available upon request from NIST Please contact George Quinn at NIST for further information (301 975-5765).
4. G. Quinn attended ISO meeting in Kyongju, Korea in September 1998.
5. DOE heavy-duty diesel engine manufacturers contractors (Cummins, Detroit Diesel Corporation and Caterpillar) were contacted and asked what topics for standards and material testing should be considered. There was strong interest in developing test methods for testing cylindrical parts. Therefore, we propose to continue developing the diametral compression method. We shall begin a task to develop the flexure test method for cylindrical parts in cooperation with work underway by M. Andrews at ORNL.

References

1. D. R. Clarke, "A Large Scale Processing Inhomogeneity in Silicon Nitride Ceramics and Its Effect on Oxidation," pp 110-118 in Preparation and Properties of Silicon Nitride Based Materials Science Forum, Vol. 47 (1989).
2. G. A. Forster and W. Ellingson, "An Investigation of Penetrant Techniques for Detection of Machining-Induced Surface-Breaking Cracks on Monolithic Ceramics," ORNL TR ORNL/Sub/93-SN893-1,Feb. 1996.
3. L. Weiler, "Cylinder-Segment Bend Test, A New Strength Measuring Technique for Ceramic Tubes and Cylinders," pp 621-625 in Science of Ceramics 14, Ed. D. Taylor, The Institute for Ceramics, Stoke on Trent, 1988.

ORNL/TM-13735

INTERNAL DISTRIBUTION

L. F. Allard, Jr.
P. F. Becher
T. M. Besmann
P. J. Blau
R. A. Bradley
K. Breder
C. R. Brinkman
T. D. Burchell
A. Choudhury
D. D. Conger
S. A. David
M. K. Ferber
R. L. Graves
H. W. Hayden, Jr.
C. R. Hubbard
M. A. Janney
D. R. Johnson (5)
R. R. Judkins
M. A. Karnitz
R. J. Lauf
K. C. Liu
W. D. Manly
S. B. McSpadden
T. A. Nolan
A. E. Pasto
M. H. Rawlins
A. C. Schaffhauser
D. P. Stinton
T. N. Tiegs
S. G. Winslow
R. E. Ziegler
Laboratory Records - RC

EXTERNAL DISTRIBUTION

Jeffrey Abboud
U.S. Advanced Ceramics Assoc.
1600 Wilson Blvd., Suite 1008
Arlington VA 22209

B. P. Bandyopadhyay
University of North Dakota
Box 8359 University Station
Grand Forks ND 58202-8359

Donald F. Baxter, Jr.
Advanced Materials & Processes
ASM International
9639 Kinsman Road
Materials Park OH 44073-0002

M. Brad Beardsley
Caterpillar Inc.
Technical Center Bldg. E
P.O. Box 1875
Peoria IL 61656-1875

Ramakrishna T. Bhatt
NASA Lewis Research Center
MS-106-1
21000 Brookpark Road
Cleveland, OH 44135

Bruce Boardman
Deere & Company, Technical Ctr.
3300 River Drive
Moline IL 61265-1792

Michael C. Brands
Cummins Engine Company, Inc.
P.O. Box 3005, Mail Code 50179
Columbus IN 47201

Donald J. Bray
Advanced Refractory Technologies
699 Hertel Avenue
Buffalo NY 14207

Walter Bryzik
U.S. Army Tank Automotive
Command
R&D Center, Propulsion Systems
Warren MI 48397-5000

David Carruthers
Kyocera Industrial Ceramics
5713 East Fourth Plain
Vancouver WA 98661

Ronald H. Chand
Chand Kare Technical Ceramics
2 Coppage Drive
Worcester MA 01603-1252

William J. Chmura
Torrington Company
59 Field Street, P.O. Box 1008
Torrington CT 06790-1008

William S. Coblenz
Defense Adv. Research Projects Agency
3701 N. Fairfax Drive
Arlington VA 22203-1714

Gloria M. Collins
ASTM
100 Barr Harbor Drive
West Conshohocken PA 19428-2959

Shawn Cooper
FEV Engine Technology
2285 Opdyke Road, Suite F
Auburn Hills MI 48326

Douglas Corey
AlliedSignal, Inc.
2525 West 190th Street, MS:T52
Torrance CA 90504-6099

Keith P. Costello
Chand/Kare Technical Ceramics
2 Coppage Drive
Worcester MA 01603-1252

Gary M. Crosbie
Ford Motor Company
P.O. Box 2053, 20000 Rotunda Drive
MD-3182, SRL Building
Dearborn MI 48121-2053

Pamela Cunningham
WETO Technical Library
MSE, Inc.
Industrial Park, P. O. Box 4078
Butte MT 59702

Sidney Diamond
U.S. Department of Energy
Office of Transportation Technologies
EE-33, Forrestal Building
Washington DC 28505

Ernest J. Duwell
3M Abrasive Systems Division
3M Center, Bldg. 251-01-34
St. Paul MN 55144

Michael Easley
AlliedSignal Engines
P. O. Box 52181
MS 551-11
Phoenix AZ 85072-2181

J. J. Eberhardt
U.S. Department of Energy
Office of Transportation Technologies
EE-33, Forrestal Building
Washington DC 20585

Jim Edler
Eaton Corporation
26201 Northwestern Highway
P.O. Box 766
Southfield MI 48037

William A. Ellingson
Argonne National Laboratory
Energy Technology Division, Bldg. 212
9700 S. Cass Avenue
Argonne IL 60439-3848

John W. Fairbanks
U.S. Department of Energy
Office of Transportation Technologies
EE-33, Forrestal Building
Washington DC 20585

Ho Fang
Applied Materials
2695 Augustine Drive, MS-0962
Santa Clara CA 95054

Dan Foley
AlliedSignal Ceramic Components
MS:1/5-1, 26000
2525 West 190th Street
Torrance CA 90504

Douglas Freitag
DuPont Lanxide Composites
21150 New Hampshire Avenue
Brookeville MD 20833

Richard Gates
NIST
Bldg. 223, Rm. A-256
Rt. 270 & Quince Orchard Road
Gaithersburg MD 20899

Ludwig J. Gauckler
ETH Zurich
Nonmetallic Materials
Sonneggstr. 5
CH-8092 Zurich, SWITZERLAND

Allan E. Goldman
U.S. Graphite, Inc.
907 W. Outer Drive
Oak Ridge TN 37830

Robert J. Gottschall
U.S. Department of Energy
Metal & Ceramic Sciences, ER-131
19901 Germantown Road
Germantown MD 20874-1290

Thomas J. Gross
U.S. Department of Energy
Office of Transportation Technologies
EE-30, Forrestal Building
Washington DC 20585

Changsheng Guo
Chand Kare Technical Ceramics
2 Coppage Drive
Worcester MA 01603

Nabil S. Hakim
Detroit Diesel Corporation
13400 Outer Drive West, A08
Detroit MI 48239-4001

Alan M. Hart
Dow Chemical Company
1776 Building
Midland MI 48674

Michael H. Haselkorn
Caterpillar Inc.
Technical Center, Building E
P.O. Box 1875
Peoria IL 61656-1875

Deborah A. Haught
U.S. Department of Energy
Ofc. of Industrial Crosscut Technologies
EE-23, Forrestal Bldg.
Washington DC 20585

Daniel Hauser
Edison Welding Institute
Microjoinint & Plastics Tech. Team
1250 Arthur E. Adams Drive
Columbus OH 43221-3585

John Haygarth
Wah Chang
P.O. Box 460
Albany OR 97321-0460

Gene Huber
Precision Ferrites & Ceramics
5432 Production Drive
Huntington Beach CA 92649-1525

Thomas A. Johnson
Lanxide Corporation
1300 Marrows Road
P.O. Box 6077
Newark DE 19714-6077

Adam Jostsons
ANSTO
PMB1
Menai, NSW, Australia 2234

Yury Kalish
Detroit Diesel Corporation
Mechanical Systems
13400 Outer Drive West
Detroit MI 48239-4001

Roy Kamo
Adiabatics, Inc.
3385 Commerce Park Drive
Columbus IN 47201

W. C. King
Mack Truck, Z-41
1999 Pennsylvania Avenue
Hagerstown MD 21740

Tony Kirn
Caterpillar Inc.
Defense Products Dept., JB7
Peoria IL 61629

Joseph A. Kovach
Parker Hannifin Corporation
6035 Parkland Boulevard
Cleveland OH 44124-4141

Edwin H. Kraft
Kyocera Industrial Ceramics
5713 E. Fourth Plain Boulevard
Vancouver WA 98661

Arthur Kranish
Trends Publishing Inc.
1079 National Press Building
Washington DC 20045

Oh-Hun Kwon
Norton Company
Saint Gobain Industrial Ceramics
1 Goddard Road
Northboro MA 01532-1545

S. K. Lau
B. F. Goodrich Aerospace R&D
9921 Brecksville Road
Brecksville OH 44141

Elaine Lentini
Saint-Gobain Industrial Ceramics
Goddard Road
Northboro MA 01532

Stan Levine
NASA Lewis Research Center
21000 Brookpark Road, MS:106/5
Cleveland OH 44135

Robert H. Licht
Norton Company
Saint Gobain Industrial Ceramics
1 Goddard Road
Northboro MA 01532-1545

E. Lilley
Norton Company
Saint Gobain Industrial Ceramics
1 Goddard Road
Northboro MA 01532-1545

B. J. McEntire
Applied Materials Corporation
3050 Bowers Avenue
Santa Clara, CA 95054

James McLaughlin
Sundstrand Power Systems
4400 Ruffin Road
P.O. Box 85757
San Diego CA 92186-5757

Biljana Mikijelj
Ceradyne, Inc.
3169 Red Hill Avenue
Costa Mesa CA 92626

Carl E. Miller
Delphi Energy & Engine Mgmt. Systems
4800 S. Saginaw Street, MC 485-301-150
P. O. Box 1360
Flint MI 48501-1360

Curtis V. Nakaishi
U.S. Department of Energy
Federal Energy Tech. Center
3610 Collins Ferry Rd.
P.O. Box 880
Morgantown WV 26507-0880

Malcolm Naylor
Cummins Engine Company, Inc.
P.O. Box 3005, Mail Code 50183
Columbus IN 47202-3005

Dale E. Niesz
Ceramic & Materials Engineering
607 Taylor Road, Rm. 204
Piscataway, NJ 08854-8065

Thomas J. Paglia
Coors/ACI
3315 Boone Road
Benton AR 72015

Richard Palicka
CERCOM, Inc.
1960 Watson Way
Vista CA 92083

Vijay M. Parthasarathy
Solar Turbines
2200 Pacific Highway, M.Z. R-1
San Diego CA 92186

Magan Patel
Cummins Engine Company, Inc.
Mail Code 50183
Box 3005
Columbus IN 47202-3005

James W. Patten
Cummins Engine Company, Inc.
P.O. Box 3005, Mail Code 50183
Columbus IN 47202-3005

Stephen C. Pred
Pred Materials International, Inc.
60 East 42nd Street, Suite 1456
New York NY 10165

Vimal K. Pujari
Norton Company
Saint Gobain Industrial Ceramics
1 Goddard Road
Northboro MA 01532-1545

Fred Quan
Corning Inc.
Sullivan Park, FR-2-8
Corning NY 14831

George Quinn
NIST
I-270 & Clopper Road
Ceramics Division, Bldg. 223
Gaithersburg MD 20899

Harold Rechter
Chicago Fire Brick Company
7531 S. Ashland Avenue
Chicago IL 60620-4246

Jack A. Rubin
CERCOM, Inc.
1960 Watson Way
Vista CA 92083

Robert J. Russell
Riverdale Consulting, Inc.
24 Micah Hamlin Road
Centerville MA 02632-2107

J. Sankar
North Carolina A&T State Univ.
Dept. of Mechanical Engineering
Greensboro NC 27406

Maxine L. Savitz
AlliedSignal, Inc.
Ceramic Components
2525 West 190th Street
P.O. Box 2960, MS:1/5-1, 26000
Torrance CA 90509-2960

Jim Schienle
AlliedSignal Aerospace
1130 West Warner Road
M/S 1231-K
Tempe AZ 85284

Gary Schnittgrund
Transfer Technology
16401 Knollwood Drive
Granada Hills CA 91344

Robert S. Shane
Shane Associates
1904 NW 22nd Street
Stuart FL 34994-9270

Subu Shanmugham
MicroCoating Technologies
3901 Green Industrial Way
Chamblee GA 30341-1913

Charles Spuckler
NASA Lewis Research Center
21000 Brookpark Road, MS: 5-11
Cleveland OH 44135-3127

Gordon L. Starr
Cummins Engine Company, Inc.
P.O. Box 3005, Mail Code:50182
Columbus IN 47202-3005

Marian Swirsky
Cambridge Scientific Abstract
Commerce Park, Bldg. 4, Suite 804
23200 Chagrin Blvd.
Beachwood OH 44122

Victor J. Tennery
113 Newell Lane
Oak Ridge TN 37830

Malcolm Thomas
Allison Engine Company
P. O. Box 420 (W06)
Indianapolis IN 46206

Marc Tricard
Norton Company
Superabrasives Division
1 New Bond Street, MS-412-301
P. O. Box 15008
Worcester MA 01615-0008

Marcel H. Van De Voorde
Commission of the European Community
P.O. Box 2
1755 ZG Petten
THE NETHERLANDS

V. Venkateswaran
Materials Solutions International, Inc.
P.O. Box 663
Grand Island, NY 14072-0663

Michael S. Walsh
Vapor Technologies Inc.
6330 Gunpark Drive
Boulder CO 80301

Robert M. Washburn
ASMT
11203 Colima Road
Whittier CA 90604

R. W. Weeks
Argonne National Laboratory
Bldg. 362, E313
9700 S. Cass Avenue
Argonne IL 60439

Sheldon M. Wiederhorn
NIST
Building 223, Room B309
Gaithersburg MD 20899

Matthew F. Winkler
Seaworthy Systems, Inc.
P.O. Box 965
Essex CT 06426

Thomas J. Wissing
Eaton Corporation
26201 Northwestern Highway
P.O. Box 766
Southfield MI 48037

James C. Withers
MER Corporation
7960 S. Kolb Road
Tucson AZ 85706

Dale E. Wittmer
Southern Illinois University
Mechanical Engineering Dept.
Carbondale IL 62901

Egon E. Wolff
Caterpillar Inc.
Technical Center
P.O. Box 1875
Peoria IL 61656-1875

Roy Yamamoto
Ethyl Petroleum Additives, Inc.
500 Spring Street
P. O. Box 2158
Richmond VA 23218-2158

Thomas M. Yonushonis
Cummins Engine Company, Inc.
1900 McKinley Avenue
P.O. Box 3005, Mail Code 50183
Columbus IN 47202-3005

Jong Yung
Sundstrand Aerospace
Dept. 789-6
4747 Harrison Avenue
Rockford IL 61125

A. L. Zadoks
Caterpillar Inc.
Technical Center, Building L
P.O. Box 1875
Peoria IL 61656-1875

Zhenqi Zhu
Stevens Institute of Technology
Department of Mechanical Engineering
Castle Point on Hudson
Hoboken NJ 07030

Department of Energy
Oak Ridge Operations Office
Assistant Manager for Energy
Research and Development
P. O. Box 2001
Oak Ridge TN 37831-8600

For distribution by microfiche
as shown in DOE/OSTI-4500,
Distribution Category UC-332
(Ceramics/Advanced Materials).